Droplet Impact onto a Spherical Particle in Mid-Air

Sayed Abdolhossein Banitabaei

A DISSERTATION SUBMITTED TO THE FACULTY OF GRADUATE STUDIES IN PARTIAL FULFILMENT OF THE REQUIREMENT FOR THE DEGREE OF DOCTOR OF PHILOSOPHY

GRADUATE PROGRAM IN MECHANICAL ENGINEERING

YORK UNIVERSITY

TORONTO, ONTARIO

July 2019

ABSTRACT

Collision between a droplet and a particle has a wide range of applications in chemical and petrochemical industries, polyethylene synthesis, and particle coating. Various studies in the literature indicate that the collision products are very different depending on the size and velocity of the particle and droplet, particle wettability and roughness, and physical properties of the liquid and the surrounding gas. The collision outcome is a liquid film (i.e. lamella) and the objective of this thesis is to identify various impact products in different conditions and to study how each category of the above mentioned parameters or a combination of them affect the lamella formation. Investigation of the droplet impact was divided into two parts: drop impact onto a still particle, and droplet impact onto a moving particle in mid-air. Contribution of this thesis to the field can be summarized as following. First, studying the impact phenomenon in a wider range of both Weber number ($0.1<We<1146$) and droplet-to-particle diameter ratio ($1.4<D_r<5.0$) compared to what already exists in the literature. Both experimental and numerical tools were developed and used to study the head-on impact between a droplet and a particle. Second, studying the effect of impact velocity, particle wettability, and the amount that each of these parameter contributes on collision outcomes. The required conditions for a lamella to be formed was also studied, and how the lamella geometry changes in case the impact velocity is changed, or hydrophilic/hydrophobic types of particles are used. Third, investigation of the effect of liquid viscosity on lamella formation; what the dynamics of the liquid is inside the film, and how the fluid field inside the lamella is affected by the viscosity changes. Fourth, identifying the role of ambient gas in lamella formation and how each of the drag and lift forces contribute in creating the liquid film. Fifth, developing

a pneumatic droplet generator capable of producing single drops with various droplet sizes. The breakup phenomenon in the nozzle and droplet velocity upon pinch-off were also investigated in detail.

TABLE OF CONTENTS

LIST OF TABLES

LIST OF FIGURES

NOMENCLATURE

CA	Contact angle, deg
D_d	Droplet diameter, mm
D_p	Particle diameter, mm
d_N	Nozzle diameter, mm
S	Space between droplets, mm
T	Ambient temperature, °C
U	Impact velocity, m/s
V_d	Droplet velocity, m/s
V_p	Particle velocity, m/s
σ	Surface tension, mN/m
ρ_l	Liquid density, kg/m^3
θ_{eq}	Equilibrium contact angle, deg
θ_{adv}	Advancing contact angle, deg
θ_{rec}	Receding contact angle, deg
θ_{dyn}	contact angle, deg
VOF	Volume of Fluid
DoD	Droplet on demand
μ	Liquid viscosity, cP
$We = \rho_l U^2 D_d/\sigma$	Weber number
$Re = \rho_l U D_d/\mu$	Reynolds number
$Oh = \mu/\sqrt{\rho_l \sigma D_d}$	Ohnesorge number

GLOSSARY OF TERMS

Equilibrium Contact Angle – The angle by which a liquid–vapor interface of a stationary droplet meets a solid surface which quantifies the surface wettability. Ideally, there is a unique contact angle for a given system of solid, liquid, and vapor at a given temperature and pressure. For equilibrium or static contact angle, the contact area between liquid and solid is not changed from the outside during the measurement.

Advancing Contact Angle – The advancing angle is the angle between a liquid and a solid surface during the wetting process. The advancing angle is considered as the dynamic contact angle.

Receding Contact Angle – The receding angle is the contact angle between a liquid and a wet solid surface during dewetting process. Like the advancing angle, the receding angle is considered as the dynamic contact angle.

Hydrophilic – In a hydrophilic molecule, interaction of molecules with water (and polar substances) are generally more favorable than other materials. Contact angle of water droplet on a hydrophilic surface is less than 90°.

Hydrophobic – Hydrophobic molecules are non-polar and without a charge. Therefore, they do not have tendency to interact with water. Contact angle of water droplet on a hydrophobic surface is more than 90°.

Wettability – Wettability is tendency of a liquid to spread on a solid surface in the presence of other immiscible fluids. Contact angle is one of the measures for wettability. Complete wetting is referred to as spreading. The more wettable the surface is, the smaller contact angle the liquid would demonstrate on it.

Volume of Fluid – VOF method is a numerical technique used in CFD for locating the interface. Since VOF method is not a standalone flow solving algorithm, it needs to be solved together with the Navier–Stokes equations.

Silanization – Silanization or siliconization is covering a glass surface with alkoxysilane molecules to change the wettability of the surface to increases its hydrophobicity.

Dynamic Contact Angle – The dynamic contact angle is the contact angle of a non-stationary liquid on a surface. It is defined when the liquid is wetting (advancing angle) or de-wetting (receding angle) a solid surface.

Contact Angle Hysteresis – In practice and in non-ideal surfaces, a droplet does not rest with a single value for equilibrium contact angle and hysteresis is observed that ranges from advancing contact angle to the receding contact angle. The equilibrium contact angle lies between these two values.

Contact Angle – Contact angle is the angle between the liquid surface and the outline of the contact surface when an interface exists between the liquid and the solid surface. The contact angle (wetting angle) is a measure of the wettability of a solid surface by a liquid.

Chapter 1

1.1 INTRODUCTION

Impact of droplets and particles has vast applications in various industries including, but not limited to spray drying (Hung and Yao 1999), spouted bed coating (Rocha, Taranto, & Ayub, 1995), polyethylene synthesis (Ge & Fan, 2007), and Fluidized Catalytic Cracking (Teunou & Poncelet, 2002).

As a primary topic, droplet impact on planar surfaces, mainly focuses on the effects of the impact velocity, wettability of the substrate, surface roughness, and physical properties of the liquid on variations of the collision products. Various scenarios for the impact outcomes have been reported and discussed including bouncing, spreading, splashing, and formation of fingers. A thorough review on the topic has been presented by (Josserand & Thoroddsen, 2016).

Regarding the droplet impact onto curved substrates, cylindrical objects have been among primarily used surfaces. (Rozhkov, Prunet-Foch, & Vignes-Adler, 2002) studied impact of a water droplet onto the cross section of a cylinder. They observed formation of a flat thin liquid film (i.e. lamella) for impact of smaller droplets while for larger drops, a growing conical liquid film was generated around the cylinder. There are also other impact cases in the literature that resulted in similar outcomes; see the following studies for instance: droplets of a polymeric solution impacting onto a cylinder (Rozhkov, Prunet-Foch, & Vignes-Adler, 2003), impact of ethanol droplets onto an iron cylinder (Villermaux & Bossa, 2011), impact of a droplet for a mixture of water and glycerol onto a cylinder

with the same size as the droplet (Juarez, Gastopoulos, Zhang, Siegel, & Arratia, 2012). An illustrative map of the existing literature on droplet impact onto the curved surfaces has been shown at the end of Chapter 2.

Along with the cylindrical targets, collision of a droplet onto a still spherical substrate has also been studied. (Dubrovsky, Podvysotsky, & Shraiber, 1992) worked on impact of a small droplet onto particles with different sizes. They reported that for hydrophilic surfaces, effect of particle wettability on impact outcomes was insignificant. However, in hydrophobic region, a higher contact angle decreased the amount of liquid deposited on the particle surface (contact angle was increased up to 107°).

(Mitra, Doroodchi, Pareek, Joshi, & Evans, 2013) studied the effect of impact velocity on outcomes of droplet collision onto a brass sphere. They observed that by increasing Weber number, the spreading diameter was increased, while the contact time was decreased. However, they worked within a limited range of Weber numbers and did not go beyond 83 ($\boldsymbol{We = \rho_l U^2 D_d/\sigma}$). Earlier than that (Hardalupas, Taylor, & Wilkins, 1999) impacted mono-disperse droplets of water, ethanol, and glycerol ($\boldsymbol{160 \leq D_d \leq 230\ \mu m}$) onto a 1 mm spherical target with an impact velocity in the range of 6 to 13 m/s. They observed a crown-like and radially outward liquid film characteristics of which were influenced by the liquid properties, droplet kinematic parameters, and surface roughness. Formation of a similar liquid film during impingement of a water droplet onto a copper hemisphere had been already reported by (Levin & Hobbs, 1971).

A numerical model for collision of a droplet and a spherical target was developed by (Yan-Peng & Huan-Ran, 2011). They studied impact behavior and outcomes for a

range of sphere sizes from 1.26 to 50 cm, and impact velocity between 0.2 to 0.85 m/s. They found no significant difference in the duration of impact between droplet impact onto a particle and onto a plane surface. This can also be inferred by comparison of the experimental results presented by (S. Chandra & Avedisian, 1991), for droplet impact onto a plane surface, and by (Mitra, Sathe, et al., 2013), for impact on a spherical target. (Yan-Peng & Huan-Ran, 2011) also reported that the outcome of the impact process for the particle diameter (D_p) of 1.26 *mm* was geometrically similar to that for D_p=50 mm (which represents a plane surface). In all works explained above, the target was larger than the impacting droplet, and cases in which the droplet-to-particle diameter ratio (D_r) was larger than 1 were not investigated.

As discussed above, in an overwhelming majority of impact studies in the literature, D_r was always smaller than 1. A numerical study was performed by (Li, Chai, Shi, & Liang, 2014) for a droplet impact onto a cylinder with $Dr > 1$. For a head-on collision, they observed formation of a lamella around the substrate and found that wettability has a significant effect on the contact time and dynamic behavior of the liquid. Various collision scenarios with $D_r>1$ were studied by (Gac & Gradoń, 2014) for Weber numbers from 0.6 to 70. They reported Weber number as the main parameter for impact characterization and observed that when a droplet is larger than the particle ($D_r>1$), three collision scenarios were possible as they increased the Weber number: coalescence without disintegration, ripping and coating with some small satellite droplets, and for We~70, formation of a long conical film in form of a lamella was observed. Nevertheless, the range of Weber number they worked was relatively narrow (0.6<We<70). They also showed that the lamella length and the time of breakup depend on the droplet to particle diameter

ratio, capillary number, and wettability of the particle, which requires studying impact cases in a wider range of D_r. However, we could find no experimental work studying this claim.

Considering the results presented by (Gac & Gradoń, 2014) together with the impact outcomes reported by (Rozhkov et al., 2002, 2003) for cylindrical objects, there might be some unique impact products in higher Weber numbers for drop impact on spherical substrates in the D_r range not tested in the above mentioned works. Collision of a hydrophobic particle onto a water droplet within the above mentioned gap (D_r = 1.45) was performed by (Sechenyh & Amirfazli, 2016). They reported three different regimes including formation of a conical lamella, and studied variations of some lamella geometrical parameters based on the impact Weber number. However, some questions were left unanswered including why and how a lamella forms, the effect of particle wettability on impact duration, the effect of contact angle changes in hydrophobic range on lamella geometry and the effect of liquid viscosity and size ratio (specifically when D_r >1) on impact products.

Another important aspect of droplet impact onto a particle is the spatial and temporal variations of liquid film thickness formed on the substrate. (Dubrovsky, Podvysotsky, and Shraiber 1992) reported that the droplet-to-particle size ratio affects thickness of the liquid film formed during the impact. Three phases for such an impact were introduced by (Bakshi, Roisman, & Tropea, 2007) including initial drop deformation, inertia dominated phase, and viscosity dominated phase. They found that in the first two phases, non-dimensional variation of the film thickness for various Reynolds numbers fits

onto a single curve. It should be noted that variations of the film thickness for $D_r > 1$ has not been studied in the literature.

Effect of ambient gas on lamella formation has been also discussed in the literature for droplet impact onto a flat surface. (L. Xu, Zhang, & Nagel, 2005) identified two effective forces; a destabilizing force applied to the drop from the surrounding gas (F_d), and surface force (F_σ) which prevents further lamella stretching. (Bird, Tsai, & Stone, 2009) argued that the trade-off between these two sources varies with density and pressure of the ambient gas. (Riboux & Gordillo, 2014) determined onset of splashing through the lift force applied by the surrounding gas to the edge of the lamella. They found that if this lift force is large enough to prevent the rim from reattaching to the object, the lamella detaches from the surface and splashing happens. According to their findings, density and viscosity of the gas phase affect the splashing onset. However, effect of the ambient gas on lamella spreading in droplet-particle impact has not been addressed yet.

In terms of the droplet impact onto particles and curved surfaces, a detailed literature review has been presented in the introduction of Chapters 2 and 3. A brief review of the important areas in the field includes:

1) Droplet and particle impact velocity
2) Effect of particle wettability changes in hydrophobic range
3) Effect of droplet-to-particle size ratio for D_r>1
4) Physical properties of liquid (e.g. viscosity and surface tension)
5) Particle surface characteristics (e.g. temperature and roughness)

Despite the large number of works available in the literature, combination of the above mentioned parameters can possibly result in specific impact conditions and products which have not been investigated yet. Moreover, behavior of the fluid field inside the liquid film during the lamella formation is worth studying. Therefore, the gaps in the literature were identified and prioritized as the objectives of this thesis and are briefly explained below.

In the present studies, the particle is a solid sphere with a typical diameter of 2 mm made of polystyrene, glass, etc. to have various surface wettabilities. Droplet impact was first investigated on a still particle in which the impact velocity was the same as velocity of the droplet. In the second chapter, the effect of particle wettability and impact velocity on impact products and duration of the collision were systematically studied in experiments (No. 1 and 2 in the list above). Compared to the literature, the range of Weber numbers investigated was significantly extended ($0.1 < We < 1146$) here. While focus of the previous works was mostly on impacts in which the droplet was smaller than the particle, D_r was chosen to be larger than one so that a thin liquid film in the form of a truncated cone was formed. A dimensional analysis was also performed which relates geometrical parameters of the lamella to the time and the impact velocity. Moreover, a numerical simulation was used to study that whether and how variations of particle hydrophobicity affects the impact outcome.

After studying impact on a still particle, collision of a falling droplet and a moving hydrophobic particle in mid-air was investigated. First, an experimental study was conducted for a head-on impact between a droplet falling by gravity and a particle shot

upwards (D_r~1.4 and *We*~1800). Due to difficulties in performing experiments for every and all conditions, a numerical simulation tool was also developed and verified with the experimental results to be used for parametric studies. The effect of droplet-to-particle diameter ratio and the liquid viscosity on lamella formation were investigated (No. 3 and 4 in the list above). The numerical model was also used to determine the flow pattern and the velocity field inside the lamella. Furthermore, effect of ambient gas density and the drag force on formation of the liquid film was investigated. Therefore, our understanding from the following topics was improved: a) the required conditions for lamella formation in droplet impact onto a particle, b) effect of each parameter on the final product, c) dynamics of the fluid and how flow inside the lamella is evolved during the impact, d) how characteristics of the particle, droplet, and the ambient can affect the flow pattern.

For the droplet-particle impact investigation, having single droplets with various sizes and velocities is crucial. Therefore, a pneumatic droplet generator was designed and manufactured. Using interchangeable nozzle heads, although it was capable of generating droplets with different sizes, we realized that achieving various initial velocities upon droplet generation was not physically possible by the device. This occurs due to the timely contribution of surface tension force during the droplet pinch-off process elaborated in Chapter 4.

It should be noted that the present document is a paper-based thesis in which each chapter has a distinct objective and has been already published or submitted for publication in a journal. Therefore, as mentioned above, each chapter includes a

dedicated and detailed introduction which is a complementary of what was just presented above.

1.2 CONTRIBUTIONS

1.2.1 JOURNAL PAPERS

1. S. A. Banitabaei, A. Amirfazli,"Droplet impact onto a solid sphere in mid-air: Effect of viscosity, gas density, and diameter ratio on impact outcomes", Phys. Fluids (to be submitted)
2. A. Razzaghi, S. A. Banitabaei, A. Amirfazli, "Shedding of Multiple Sessile Droplets by an Airflow", Phys. Fluids 30, 087104, 2018.
3. S. A. Banitabaei, A. Amirfazli,"Droplet impact onto a solid sphere: effect of wettability and impact velocity", Phys. Fluids, **29**, 06211, 2017.
4. S. A. Banitabaei, A. Amirfazli, "Pneumatic drop generator: Liquid pinch-off and velocity of single droplets", Colloids Surfaces A, *505*, *204-213, 2016.*

Three of the papers (i.e. chapters 2, 3 and 4) have just two authors and all what you read in those chapters are originally conducted and written by me and my supervisor. The fourth paper (i.e. Appendix A) however, is contribution of the simulation capabilities that I developed during my PhD in a master thesis related to droplet shedding. The experimental work of this study was already published by the authors in a separate paper. However, that paper is focused on the results of numerical simulations performed for various conditions of the droplets configuration and I have implemented all those numerical simulations in the paper. This has been clarified in Appendix A as well.

1.2.2 CONFERENCE CONTRIBUTIONS

1. S.A. Banitabaei, A. Amirfazli, “Numerical simulation of droplet impact onto a solid sphere in mid-air”, DFD 2017, Denver, USA, Nov. 19-22, 2017.
2. A. Razzaghi, S. A. Banitabaei, A. Amirfazli, “The role of drag force in shedding of multiple sessile drops”, DFD 2017, Denver, USA, Nov. 19-22, 2017.
3. S.A. Banitabaei, A. Amirfazli**,** “Droplet impact onto a solid sphere: effect of wettability and impact velocity”, APS 69th Ann. Meeting DFD, Portland, USA, Nov. 20-22, 2016.
4. S.A. Banitabaei, A. Amirfazli, “A New Pneumatic Micro-drop Generator”, 6th Bubbles & Drops Workshop, Potsdam-Golm, Germany, July 6-10, 2015.
5. S.A. Banitabaei, A. Amirfazli, “Droplet impact with a solid particle: An energy model for lamella formation”, 89th ACS Colloid Surface Sci. Symp., Pittsburgh, USA, June 15-17, 2015.
6. V. Sechenyh, S.H. Banitabaei, M. Karimi, A. Amirfazli, “Drop Impact onto a Solid Particle”, APS 67th Ann. Meeting DFD, San Francisco, USA, Nov. 23-25, 2014. (Gallery of Fluid Motion)

1.3 REFERENCES

Amirzadeh, A., Raessi, M., & Chandra, S. (2013). Producing molten metal droplets smaller than the nozzle diameter using a pneumatic drop-on-demand generator, *47*, 26–33. Retrieved from http://apps.isiknowledge.com/full_record.do?product=UA&search_mode=GeneralSearch&qid=25&SID=2AaJQm1KcsyxSaIMKRU&page=1&doc=1

Apparatus and method for generating droplets. (2002, September 10). Retrieved from

http://www.google.com/patents/US6446878

Bakshi, S., Roisman, I. V., & Tropea, C. (2007). Investigations on the impact of a drop onto a small spherical target. *Physics of Fluids*, *19*(3). https://doi.org/10.1063/1.2716065

Bird, J. C., Tsai, S. S. H., & Stone, H. A. (2009). Inclined to splash: triggering and inhibiting a splash with tangential velocity. https://doi.org/10.1088/1367-2630/11/6/063017

Chang, S., Attinger, D., Chiang, F., Zhao, Y., & Patel, R. C. (2004). SIEM measurements of ultimate tensile strength and tensile modulus of jetted, UV-cured epoxy resin microsamples. *Rapid Prototyping Journal*, *10*(3), 193–199. https://doi.org/10.1108/13552540410539012

Cheng, S., & Chandra, S. (2003). A pneumatic droplet-on-demand generator, *34*(6), 755–762. Retrieved from http://apps.isiknowledge.com/full_record.do?product=UA&search_mode=GeneralSearch&qid=26&SID=2AaJQm1KcsyxSaIMKRU&page=1&doc=3

Cheng, S. X., Li, T., & Chandra, S. (2005). Producing molten metal droplets with a pneumatic droplet-on-demand generator. *Journal of Materials Processing Technology*, *159*(3), 295–302. https://doi.org/10.1016/j.jmatprotec.2004.05.016

de Gans, B., Duineveld, P., & Schubert, U. (2004). Inkjet printing of polymers: State of the art and future developments, *16*(3), 203–213. Retrieved from http://apps.isiknowledge.com/full_record.do?product=UA&search_mode=GeneralSearch&qid=20&SID=2AaJQm1KcsyxSaIMKRU&page=1&doc=2

Development of a molten metal droplet generator for rapid prototyping. (n.d.). Retrieved October 14, 2015, from

https://openlibrary.org/books/OL21790290M/Development_of_a_molten_metal_droplet_generator_for_rapid_prototyping

Dubrovsky, V. V., Podvysotsky, A. M., & Shraiber, A. A. (1992). Particle interaction in three-phase polydisperse flows. *International Journal of Multiphase Flow*, *18*(3), 337–352. https://doi.org/10.1016/0301-9322(92)90021-8

Edd, J. F., Di Carlo, D., & Humphry, K. J. (2008). Controlled encapsulation of single-cells into monodisperse picolitre drops, *8*(8), 1262–1264. Retrieved from http://apps.isiknowledge.com/full_record.do?product=UA&search_mode=GeneralSearch&qid=18&SID=2AaJQm1KcsyxSaIMKRU&page=1&doc=1

Fang, M., Chandra, S., & Park, C. B. (2008). Building three-dimensional objects by deposition of molten metal droplets, *14*(1), 44–52. Retrieved from http://apps.isiknowledge.com/full_record.do?product=UA&search_mode=GeneralSearch&qid=4&SID=2AaJQm1KcsyxSaIMKRU&page=1&doc=1

Foutsis, & Vassilis. (2004). *Producing Small Molten Metal Drops with a Pneumatic Generator [microform]*. Thesis (M.A.Sc.)--University of Toronto. Retrieved from https://books.google.ca/books/about/Producing_Small_Molten_Metal_Drops_with.html?id=ffbNygAACAAJ&pgis=1

Gac, J. M., & Gradoń, L. (2014). Lattice-Boltzmann modeling of collisions between droplets and particles. *Colloids and Surfaces A: Physicochemical and Engineering Aspects*, *441*, 831–836. https://doi.org/10.1016/J.COLSURFA.2012.11.078

Gao, F., & Sonin, A. A. (1994). Precise Deposition of Molten Microdrops: The Physics of Digital Microfabrication. *Proceedings of the Royal Society A: Mathematical, Physical and*

Engineering Sciences, *444*(1922), 533–554. https://doi.org/10.1098/rspa.1994.0037

Ge, Y., & Fan, L.-S. (2007). Droplet-particle collision mechanics with film-boiling evaporation. *Journal of Fluid Mechanics*, *573*, 311. https://doi.org/10.1017/S0022112006003922

Hardalupas, Y., Taylor, A. M. K. P., & Wilkins, J. H. (1999). Experimental investigation of sub-millimetre droplet impingement onto spherical surfaces. *International Journal of Heat and Fluid Flow*, *20*(5), 477–485. https://doi.org/10.1016/S0142-727X(99)00045-4

Hayes, D., Cox, W., & Grove, M. (1998). Micro-jet printing of polymers and solder for electronics manufacturing, *8*(3–4), 209–216. Retrieved from http://apps.isiknowledge.com/full_record.do?product=UA&search_mode=GeneralSearch&qid=21&SID=2AaJQm1KcsyxSaIMKRU&page=1&doc=1

Hung, L. S., & Yao, S. C. (1999). Experimental investigation of the impaction of water droplets on cylindrical objects. *International Journal of Multiphase Flow*, *25*(8), 1545–1559. https://doi.org/10.1016/S0301-9322(98)00085-8

Josserand, C., & Thoroddsen, S. T. (2016). Drop Impact on a Solid Surface. *Annual Review of Fluid Mechanics*, *48*(1), annurev-fluid-122414-034401. https://doi.org/10.1146/annurev-fluid-122414-034401

Juarez, G., Gastopoulos, T., Zhang, Y., Siegel, M. L., & Arratia, P. E. (2012). Splash control of drop impacts with geometric targets. *Physical Review E - Statistical, Nonlinear, and Soft Matter Physics*, *85*(2), 1–6. https://doi.org/10.1103/PhysRevE.85.026319

Levin, Z., & Hobbs, P. V. (1971). Splashing of Water Drops on Solid and Wetted Surfaces: Hydrodynamics and Charge Separation. *Philosophical Transactions of the Royal*

Society A: Mathematical, Physical and Engineering Sciences, *269*(1200), 555–585. https://doi.org/10.1098/rsta.1971.0052

Li, Q., Chai, Z., Shi, B., & Liang, H. (2014). Deformation and breakup of a liquid droplet past a solid circular cylinder: A lattice Boltzmann study. *Physical Review E - Statistical, Nonlinear, and Soft Matter Physics*, *90*(4), 1–10. https://doi.org/10.1103/PhysRevE.90.043015

Masters, K. (1985). *Spray Drying Handbook*. *Halstead Press*. Halstead Press. https://doi.org/10.1002/aic.690330131

Mitra, S., Doroodchi, E., Pareek, V., Joshi, J. B., & Evans, G. M. (2013). Collision Behaviour of a Small Spherical Particle on a Large Stationary Droplet.

Mitra, S., Sathe, M. J., Doroodchi, E., Utikar, R., Shah, M. K., Pareek, V., … Evans, G. M. (2013). Droplet impact dynamics on a spherical particle. *Chemical Engineering Science*, *100*, 105–119. https://doi.org/10.1016/j.ces.2013.01.037

Orme, M., & Smith, R. (2000). Enhanced aluminum properties by means of precise droplet deposition, *122*(3), 484–493. Retrieved from http://apps.isiknowledge.com/full_record.do?product=UA&search_mode=GeneralSearch&qid=19&SID=2AaJQm1KcsyxSaIMKRU&page=1&doc=1

Producing droplets smaller than the nozzle diameter by using a pneumatic drop-on-demand droplet generator. (2008). *Experiments in Fluids*, *44*(1), 105–114. https://doi.org/10.1007/s00348-007-0378-z

Rezai, P., Salam, S., Selvaganapathy, P. R., & Gupta, B. P. (2012). Electrical sorting of Caenorhabditis elegans. *Lab on a Chip*, *12*(10), 1831.

https://doi.org/10.1039/c2lc20967e

Rezai, P., Salam, S., Selvaganapathy, P. R., & Gupta, B. P. P. (2011). Effect of pulse direct current signals on electrotactic movement of nematodes Caenorhabditis elegans and Caenorhabditis briggsae. *Biomicrofluidics*, *5*(4), 044116. https://doi.org/10.1063/1.3665224

Rezai, P., Siddiqui, A., Selvaganapathy, P. R., & Gupta, B. P. (2010a). Behavior of Caenorhabditis elegans in alternating electric field and its application to their localization and control. *Applied Physics Letters*, *96*(15), 153702. https://doi.org/10.1063/1.3383223

Rezai, P., Siddiqui, A., Selvaganapathy, R., & Gupta, B. P. (2010b). Electrotaxis of Caenorhabditis elegans in a microfluidic environment. *Lab on a Chip*, *10*, 220–226. https://doi.org/10.1039/b917486a

Riboux, G., & Gordillo, J. M. (2014). Experiments of Drops Impacting a Smooth Solid Surface : A Model of the Critical Impact Speed for Drop Splashing, *024507*(JULY), 1–5. https://doi.org/10.1103/PhysRevLett.113.024507

Ricci, J. E. (1959). The Physico-chemical Constants of Binary Systems in Concentrated Solutions. Volume 1. Two Organic Compounds (without Hydroxyl Derivatives). *Journal of the American Chemical Society*, *81*(23), 6343–6344. https://doi.org/10.1021/ja01532a074

Rocha, S. C. S., Taranto, O. P., & Ayub, G. E. (1995). Aerodynamics and heat transfer during coating of tablets in two-dimensional spouted bed. *The Canadian Journal of Chemical Engineering*, *73*(3), 308–312. https://doi.org/10.1002/cjce.5450730306

Rozhkov, A., Prunet-Foch, B., & Vignes-Adler, M. (2002). Impact of water drops on small

targets. *Physics of Fluids*, *14*(10), 3485–3501. https://doi.org/10.1063/1.1502663

Rozhkov, A., Prunet-Foch, B., & Vignes-Adler, M. (2003). Impact of drops of polymer solutions on small targets. *Physics of Fluids*, *15*(7), 2006–2019. https://doi.org/10.1063/1.1580480

S. Chandra, & Avedisian, C. T. (1991). On the collision of a droplet with a solid surface, The Royal Society London Vol. 432. *Proceedings of the Royal Society of London A: Mathematical, Physical and Engineering Sciences*, *432*(1884), 13–41.

Salam, S., Ansari, A., Amon, S., Rezai, P., Selvaganapathy, P. R., Mishra, R. K., & Gupta, B. P. (2013). A microfluidic phenotype analysis system reveals function of sensory and dopaminergic neuron signaling in C. elegans electrotactic swimming behavior. *Worm*, *2*(September), e24558. https://doi.org/10.4161/worm.24558

Schena, M., Heller, R. A., Theriault, T. P., Konrad, K., Lachenmeier, E., & Davis, R. W. (1998). Microarrays: biotechnology's discovery platform for functional genomics. *Trends in Biotechnology*, *16*(7), 301–306. Retrieved from http://www.ncbi.nlm.nih.gov/pubmed/9675914

Sechenyh, V., & Amirfazli, A. (2016). An experimental study for impact of a drop onto a particle in mid-air: The influence of particle wettability. *Journal of Fluids and Structures*, *66*, 282–292. https://doi.org/10.1016/j.jfluidstructs.2016.07.020

Small droplet formation in a pneumatic drop-on-demand generator: Experiments and analysis. (2010). *Experimental Thermal and Fluid Science*, *34*(8), 1488–1497. https://doi.org/10.1016/j.expthermflusci.2010.07.013

Sui, G., & Leu, M. (2003). Investigation of layer thickness and surface roughness in rapid

freeze prototyping, *125*(3), 556–563. Retrieved from http://apps.isiknowledge.com/full_record.do?product=UA&search_mode=GeneralSearch&qid=1&SID=2AaJQm1KcsyxSaIMKRU&page=1&doc=1

Teunou, E., & Poncelet, D. (2002). Batch and continuous fluid bed coating – review and state of the art. *Journal of Food Engineering*, *53*(4), 325–340. https://doi.org/10.1016/S0260-8774(01)00173-X

Tong, J., Rezai, P., Salam, S., Selvaganapathy, P. R., & Gupta, B. P. (2013). Microfluidic-based electrotaxis for on-demand quantitative analysis of Caenorhabditis elegans' locomotion. *Journal of Visualized Experiments : JoVE*, (75), e50226. https://doi.org/10.3791/50226

Villermaux, E., & Bossa, B. (2011). Drop fragmentation on impact. *Journal of Fluid Mechanics*, *668*, 412–435. https://doi.org/10.1017/S002211201000474X

Xie Dan, Zhang HongHai, & Shu XiaYun. (2010). Multi-materials drop-on-demand inkjet technology based on pneumatic diaphragm actuator, *53*(6), 1605–1611. Retrieved from http://apps.isiknowledge.com/full_record.do?product=UA&search_mode=GeneralSearch&qid=27&SID=2AaJQm1KcsyxSaIMKRU&page=1&doc=1

Xu, J., & Attinger, D. (2008). Drop on demand in a microfluidic chip. *Journal of Micromechanics and Microengineering*, *18*(6), 065020. https://doi.org/10.1088/0960-1317/18/6/065020

Xu, L., Zhang, W. W., & Nagel, S. R. (2005). Drop Splashing on a Dry Smooth Surface, *184505*(May), 1–4. https://doi.org/10.1103/PhysRevLett.94.184505

Yan-Peng, L., & Huan-Ran, W. (2011). Three-dimensional direct simulation of a droplet

impacting onto a solid sphere with low-impact energy. *Canadian Journal of Chemical Engineering*, *89*(1), 83–91. https://doi.org/10.1002/cjce.20399

Chapter 2

Effect of Wettability and Velocity on Impact Products*

2.1 INTRODUCTION

Collision of a droplet and a spherical solid object has a wide range of applications in chemical and petrochemical industries (e.g. fluid catalytic cracking; FCC), polyethylene synthesis, particle coating (e.g. in pharmaceutical processes), as well as modification of surface roughness.

In terms of geometry and kinematics of the impact, studies regarding droplet collision onto a solid object can be classified into the following categories: drop impact onto planar surfaces [1-5], droplet collision with cross section of a cylindrical object [6-9], droplet impact with lateral surface of a cylinder [10-14], droplet impact onto a stationary solid sphere [15-21], and droplet-particle collision in mid-air [22-24]. However, with respect to the characteristics of substrate or liquid, one may consider the following categories as well: droplet impact onto a mesh or a membrane [25], drop impact onto rough or porous objects [26-27], impact of a droplet onto a flexible/deformable surface 28], drop impact onto open structure surfaces [29], impact on moving surfaces [30], droplet impact with patterned surfaces [31], and impact of non-Newtonian droplets onto

* This chapter has been published as a journal paper: S. A. Banitabaei, A. Amirfazli, ”Droplet impact onto a solid sphere: Effect of wettability and impact velocity”, *Physics of Fluids* **29**, 062111 (2017).

surfaces [32]. There are also studies in the literature for collision of a particle falling down on a stationary droplet [33-34].

This introduction is intended to form a basis for studying formation of liquid films due to droplet impact onto different surfaces, specifically spherical targets. But, by way of background, first, formation of a crown-shaped liquid film is presented due to a droplet impact onto a smooth surface and parameters that affect crown formation and its geometry are introduced. Then, different works on droplet impact onto cylindrical targets will be presented, some of which also report formation of a conical liquid film around the target. Finally, droplet impact onto stationary and moving spherical objects will be discussed, impact morphology will be explored, and the conditions (e.g. impact velocity and particle wettability) for which a liquid film (i.e. lamella) is generated after the impact will be presented.

Josserand and Thoroddsen [35] reviewed recent theoretical and experimental studies of drop impact onto solid surfaces. They mainly focused on explanation of the underlying physical concepts and the complicated interplay between liquid inertia, viscosity, surface tension, and the surrounding gas related to formation of impact outcomes. They specifically emphasized bouncing, spreading, splashing, fingering and air entrapment. For impact onto a planar surface, they explained that an air cushion is generated at the initial contact area and lifts the emerged liquid film (i.e. lamella) away from the solid surface to start gliding on a thin sheet of air. The effect of surface roughness and hydrophobicity on the impact phenomena was addressed as well.

Stevens *et al.* [36] studied evolution of splash for a drop impact onto a smooth surface and observed that the drop spreads and forms a liquid sheet, where for a low viscosity liquid (i.e. μ ~1 *mPa.s*), a crown-shaped corona emerges. However, they explained that considering the first moment of impact as t=0, there is always a delay for the corona emergence which is smaller for liquids with a lower viscosity. Ambient pressure (P_{amb}) was also recognized as another important parameter in corona formation and they realized that as P_{amb} is decreased, the emerged crown decreases in size until it vanishes.

Rozhkov *et al.* [6] studied impact of 2.8 *mm* and 3.95 *mm* water droplets onto the cross section of a stainless steel cylinder with a diameter of 3.9 *mm*. For a droplet impact velocity of 3.5 *m/s*, they observed that the primary stage of the impact is similar to drop collision with a planar surface, but the later stages were different. The liquid spread beyond the target and in case of the smaller droplets, collision transforms the drop into an almost flat thin liquid film. However, large droplets created a conical liquid film around the cylinder terminated by a thicker rim. They observed that lamella was growing both in length and base diameter and liquid flowed towards the rim up to a certain time that most of the liquid accumulated in the rim and lamella became very thin, leading to its rupture. Similar impact outcomes were also reported by: 1) Rozhkov *et al.* [7] for collision of droplets of a polymeric solution onto a cylindrical target, 2) Villermaux and Bossa [8] for impact of 6 *mm* droplets of water and ethanol with an iron cylinder of the same diameter, and later 3) Juarez *et al.* [9] for impact of 2.85 *mm* droplets of water and glycerol mixture (viscosity $\nu = 10\ \mathrm{cP}$, surface tension $\gamma = 0.035\ \mathrm{N/m}$) onto a cylinder with a diameter of 2.85 *mm*. An analytical model was also developed by Rozhkov *et al*. [37] to explain

dynamics of the resulting outcomes of the droplet impact onto a disc target and predict the structure of the liquid flow inside the lamella.

In case of collision between a droplet and a stationary solid sphere, the important issues include physical properties of liquid, geometry and surface roughness, temperature of the target, diameter ratio of droplet and particle (D_r), and impact velocity (V_0). These parameters can significantly affect the type and geometry of the impact outcomes, and some of these parameters will be the focus of this chapter as will be discussed below.

Dubrovsky *et al.* [22] performed an experimental investigation on the interaction of liquid droplets with solid particles of different sizes and velocities. They studied impact of a small droplet (D_d from 0.65 to 1.05 *mm*) with a large still solid particle (D_p from 3.2 to 8.0 *mm*) i.e. D_r between 0.08 to 0.22. They found that collision of a fast-moving small drop with a large solid particle will result in droplet breakup followed by formation of a certain number of liquid fragments. They introduced a coalescence parameter (X) for impact as the ratio of change in target mass to the mass of the colliding droplet when the impact is completed. They found an increase in the coalescence parameter as the particle to droplet diameter ratio is increased. They also performed experiments with targets made from different materials as well as targets covered by a hydrophobic film. Their experiments revealed that for wetting surfaces ($\theta < 90°$), the effect of particle wettability on impact outcomes is not significant. However, for non-wetting target surfaces ($\theta > 90°$), a significant decrease in X was observed by increasing the contact angle (θ). Although

the maximum contact angle in their tests was $107°$, they extrapolated the results and inferred that if $\theta \rightarrow 180°$ then $X \rightarrow 0$.

Mitra *et al.* [23] performed a theoretical and experimental study on droplet impact onto a thermally conductive brass sphere with a diameter of 10 mm. They investigated the effect of Weber number and surface temperature on droplet spreading and evolution of the impact outcomes. They used water droplets of 3.1 mm diameter; and isopropyl alcohol and acetone droplets of 2.1 mm diameter. The impact outcomes were either a spreading liquid sheet or a rebounding droplet. They studied the impact phenomena in a range of Weber numbers from 8 to 84 and observed that as *We* is increased, maximum spreading diameter is increased and droplet contact time with the solid particle is decreased. Ge and Fan [17] also developed a 3D model for collision between an evaporating droplet (acetone with 1.8 to 2.1 mm diameter) and a high-temperature brass target of 3.2 or 5.5 mm diameter. They found that in film boiling condition, the droplet undergoes a spreading, recoiling and rebounding process. For a 3.2 mm target, spreading was larger on the particle surface compared to the 5.5 mm target on which the droplets jumped higher in the rebounding phase. Their results showed that the droplet contact time with the particle is almost independent of the impact velocity.

Hardalupas *et al.* [15] performed experiments with water, ethanol and glycerol with various concentrations to create liquids with different surface tensions and viscosities. They generated mono-disperse droplets between 160 and 230 μm, and velocity range of 6 to 13 m/s to impact a 1 mm spherical target. Their results indicate that a crown-like liquid film was formed at the first 10 μs of droplet impingement which its characteristics

are influenced by the liquid properties, droplet kinematic parameters, and surface roughness. Such radially outward flow in form of a crown on top of the solid surface was also reported earlier by Levin and Hobbes [38] for impingement of a 2.94 *mm* water droplet onto a dry copper hemisphere with impact velocities in the range of 1.68 to 4.8 *m/s*.

Bakshi *et al.* [16] performed an experimental and theoretical study for droplet impact with a spherical target to determine spatial and temporal variations of liquid film thickness on the target surface. They used droplets in the diameter range of 2.2 to 2.6 *mm* and stainless steel spheres with 3.2, 6 and 15 *mm* diameters as target (D_r range of 0.15 to 0.81). Their experimental results indicated that the impact phenomenon and generation of the lamella film on the target surface includes three distinct phases: initial drop deformation phase, inertia dominated phase, and viscosity dominated phase. They also investigated the effect of droplet Reynolds number and target-to-drop size ratio on the dynamics of the film flow. It was found that in the drop deformation and inertia dominated phases, non-dimensional temporal variations of film thickness for different values of Reynolds numbers collapse onto a single curve. However, for the viscous dominated stage, either an increase in *Re* or a decrease in size ratio will decrease the non-dimensional film thickness on the particle. A theoretical model was developed to account for inertial and viscous effects to calculate the evolution of the film thickness near the particle apex (i.e. height of the remaining portion of droplet on particle during impact) in the viscous dominated phase. In accordance with the results of Hardalupas *et al.* [15], they observed retraction of the liquid crown at low droplet impact velocities, and disintegration of the cusps located on the lamella rim at a high impact velocity.

Collectively, the literature for droplet impact onto a spherical target includes investigations of various liquids with a range of viscosities and surface tensions, effect of surface roughness, different target temperatures, and various impact velocities using both experimental and numerical approaches. However, in all the above studies, an impact took place between a droplet and a spherical particle in which the droplet-to-particle diameter ratio (D_r) was always smaller than 1. Li *et al.* [13] performed a lattice Boltzmann numerical study on deformation and breakup of a liquid droplet impingement on a cylindrical particle through a gravity-driven impact with $D_r > 1$. In their model, a droplet was placed on top of the cylinder. Density for both droplet and the surrounding fluid was 1 *kg/m*^{3}. The droplet motion reported in their results is suspected to be generated by a pressure difference in the boundaries of the computational domain. They investigated the effect of target wettability, viscosity ratio of both fluids, and Bond number on the dynamic behaviour of the liquid droplet. They found that wettability has an important effect on dynamic behavior of the droplet, the detachment location of liquid film from the cylindrical particle, and the contact time, i.e. the period from the first moment of impact until film detachment. By increasing wettability (i.e. $\theta \to 0$), the film detachment point moved from upper face of the cylinder to the lower face demonstrating that wettability has a significant effect on impact outcomes. Their results can motivate an experimental study to investigate effect of droplet-particle contact angle and diameter ratio on impact onto cylindrical and spherical objects.

There are also a few works in the literature regarding droplet-particle collision in mid-air (see for instance Podvysotsky and Shraiber [39] or Mitra *et al*. [23]). Dubrovsky *et al.* [22] performed an experimental investigation on collision of a small steel particle of

1 *mm* diameter with a large drop in mid-air with D_d ranging from 2.9 to 5.6 *mm*. Therefore, the range of droplet to particle diameter ratio was $2.9 \leq D_r \leq 5.6$ and either of the following scenarios was observed after impact: 1) particle was completely captured by the droplet known as bonding regime, 2) particle passed through the drop and came out of the other side with formation of an air bubble, a number of satellite droplets, or several large liquid fragments after complete disintegration of the target drop. Generally, four collision scenarios were recognized by them and a map of various impact regimes based on different *We* and *Re* numbers was proposed.

Considering the experiments performed in Ref. [22] in terms of the diameter ratio, D_r was either much smaller, or larger than 2 throughout this work. In fact, there is a significant gap in the D_r values investigated by them (i.e. $0.22 < D_r < 2.9$) that together with the new impact outcomes reported by Rozhkov *et al.* [6-7] for drop impact onto cylindrical objects of the same size, one can conclude that there might be some unique impact outcomes that have not been captured yet for droplet impact onto spherical objects in which D_r ~2. Sechenyh and Amirfazli [24] performed an experimental investigation within the above mentioned gap ($D_r = 1.45$) for impact of a high speed particle onto a falling droplet in mid-air. They conducted experiments with both hydrophilic and hydrophobic particles; and illustrated the effect of particle wettability on formation of a conical liquid film for droplet-particle impact in mid-air (see Fig. 9 in Ref. [24]). Three different regimes were reported in Ref. [24] based on the impact velocity for collision of a hydrophobic particle (polystyrene) onto a water droplet including bonding (We_{rel}<120), ripping and coating (We_{rel}~385), and shattering (610<We_{rel}<2640). For impact of a hydrophilic particle (a glass bead) onto a water droplet, ligament formation was observed

in a wide range of Weber number ($38<We_{rel}<1200$). It should be noted that aside from wettability differences, particle densities were not the same, which causes the collision energy to be different for the same impact velocities. They also reported variations of some geometrical parameters of the lamella based on the impact velocity. However, a detailed discussion of the mechanism for the observed phenomena, i.e. why and how a lamella forms, effect of particle wettability on duration of impact, and effect of contact angle variations on lamella geometry were not investigated in the literature.

A map containing the previous experimental and numerical works performed for droplet impact onto a still spherical particle is presented later in section III. The image frames are ordered based on the Weber number for each case, and droplet and particle size, liquid name, and droplet-particle contact angle (or particle roughness) are indicated on top of the images. Considering this map, one realizes that the maximum Weber number for the available studies on drop impact onto a still particle is limited to 356. Moreover, the map illustrates that in drop impact onto still objects, most of the studies investigated the impact of a small droplet onto a large particle and there is no information in the literature regarding impact outcomes for collision of a large droplet onto a small spherical target ($D_r>1$).

In the current study, after a classification and review of the available literature in drop-particle impact and possible collision outcomes in the form of a liquid film, three main issues were identified that have not been addressed to date. First, collision of a droplet onto a still spherical particle while the drop-to-particle diameter ratio is larger than 1. Therefore, $D_r\sim1.75$ was chosen to be investigated in this work for which, under some

circumstances, new impact outcomes were observed. Secondly, based on the numerical results of Li *et al.* [13] for drop impact on a solid cylinder, as well as the experimental results presented by Sechenyh and Amirfazli [24] for particle impact onto a droplet in mid-air, it is deduced that the surface wettability may have an important effect on outcomes of a droplet colliding onto a stationary spherical target. However, they did not discuss the physical nature for formation of different outcomes seen at various particle wettabilities and impact velocities. Although in Ref. [24] lamella formation was attributed to particle hydrophobicity, there is no study in the literature to investigate lamella behavior in case wettability is changed in the hydrophobic region. In the present work, a systematic study was performed to determine the effect of drop-particle contact angle on collision outcomes, and to determine its sensitivity of geometrical parameters to wettability. Thirdly, the effect of impact velocity on collision outcomes was examined through a non-dimensional analysis. In the current work, the droplet velocity was changed in a wider range of Weber number, i.e. from 0.1 to 1150, compared to We_{min} ~2 and We_{max}=356 in the literature, to capture a wider range of possible outcomes.

2.2 MATERIALS, EXPERIMENTAL SETUP, AND METHODS

2.2.1 GLASS PARTICLES

Glass beads with a diameter of 2 ± 0.01 *mm* were used as target particles. To study the effect of contact angle variations on impact outcomes, different levels of wettability is required. Silanization method was used to create the desired hydrophobicity on the surface of the glass beads. Before surface treatment, the glass beads must be completely cleaned. This was performed through sonicating the beads in acetone for 40

minutes. Then the glass beads were washed by distilled water and dried using an air stream. It should be noted that in each silanization process, a microscope slide was also put besides the glass beads to be treated exactly by the same procedure. This glass plate was later used as a control sample to measure the advancing and receding contact angles that a silan solution creates on glass beads.

The cleaned beads and glass plate were then immersed into the silan solution for 20 minutes. Three different solutions were used to achieve different levels of wettability. ChloroTrimethylSilan (CTMS) for creating a hydrophilic surface, OctaDecylTrichloroSilan (ODTS) for making a hydrophobic glass surface, and a 50% *wt* combination of CTMS and ODTS for having an intermediate contact angle value.

The glass was then taken out and washed with a strong stream of cold water (to prevent further polymerization) and then by acetone to be completely cleaned from the products of the silanization process. The glass beads were transferred to a clean container and the control sample used for contact angle measurements. A goniometer, equipped with a computer-controlled liquid dispenser and a digital camera (60 *fps*), was used to measure the advancing and receding contact angles. Measurements were repeated 3 times for each material (see Table 1).

Table 2-1. *Water contact angles measured on flat glass surfaces coated with different silan solutions.*

Silan solution used for glass treatment	Contact angle (θ)		
	Advancing	**Equilibrium**	**Receding**
ChloroTrimethylSilan (CTMS)	70˚ ± 2˚	57˚ ± 2˚	40˚ ± 1˚
ODTS+CTMS (50% *wt*)	90˚ ± 3˚	80˚ ± 2˚	69˚ ± 2˚
OctaDecylTrichloroSilan (ODTS)	118˚ ± 2˚	100˚ ± 2˚	76˚ ± 3˚

2.2.2 EXPERIMENTAL APPARATUS AND ANALYSIS METHOD

Figure 2-1 illustrates a schematic of the setup used for performing the experiments. A 50 *μl* syringe was used to generate the water droplets. The syringe was activated by a computer controlled stepper motor to avoid vibrations induced by manual discharge of the syringe. The height of the syringe was adjustable from almost above the particle up to a 1.5 *m* height to achieve droplet velocities between 0.05 to 5 *m/s*. A cylindrical shroud was also used to isolate the falling droplet from disturbing flows in the surrounding environment.

To minimize the interference of particle holder with the impact process, a small glass tube with a diameter of 0.8 *mm* was used. Inner diameter of the glass tube was 0.2 *mm* and was connected to a vacuum pump (absolute pressure of 200 *mbar*). Therefore, the particle was firmly kept on top of the thin glass tube during the impact. Two perpendicular positioning stages were also used to let the operator adjust the particle location precisely beneath the needle. However, due to the drag force, the droplet did not always remain a perfect sphere while falling down which led to a horizontal displacement

in each test that prevented an accurate head-on collision. In such cases, the test was repeated with a new dry particle, to ensure a head-on impact.

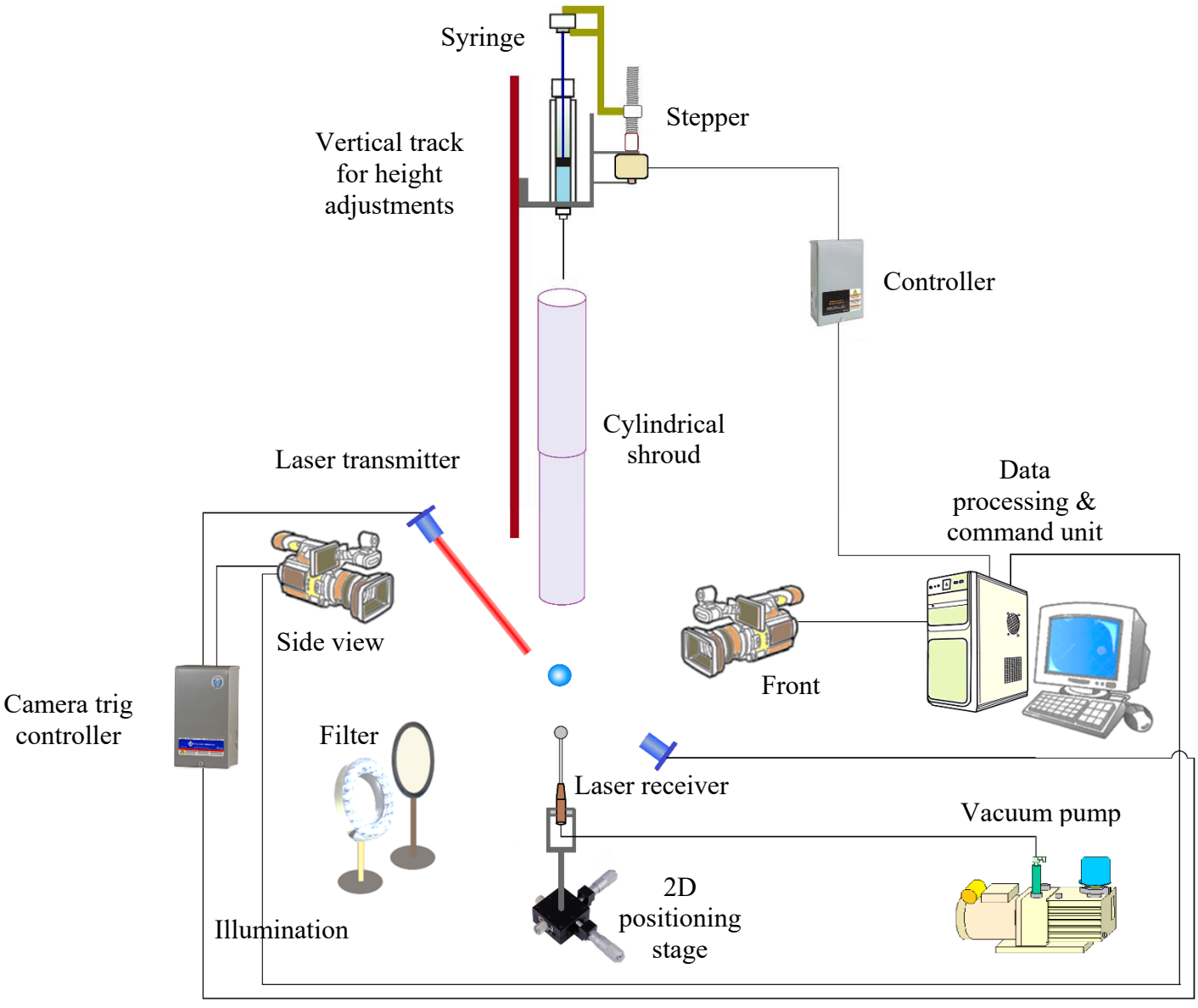

Figure 2-1 *Schematic of the experimental setup for studying droplet-particle impact.*

Two high speed cameras were used to capture images from two perpendicular views to ensure the head-on impact taking place. The front view was captured by a

Phantom Miro-310 as the master camera connected to a Phantom V4.3 for capturing the side view images. The front view camera was externally trigged through a control box connected to a laser receiver constantly exposed to a laser beam. When droplet passes through the beam, a pulse was generated to trigger the master camera. Both cameras were equipped with high resolution optics; Tamron AF 180*mm* f/3.5 SP for the front view camera and Edmund Optics 50 *mm* was mounted on the side view camera. An AmScope LED-96S with a diffuser were also used as illumination system.

Both cameras were synchronized to capture 7000 *fps* and Phantom Miro-310, which provided the front view images, was set on a resolution of 640×480 pixels and an exposure time of 97 *μs*. Droplet size, velocity, and other geometrical parameters of the lamella were all determined by manual image processing through ImageJ software for both experiments and simulations. A single frame from a calibration grid (with 0.25 *mm* mesh size) was captured after each experiment to determine the pixel size; precision for the length measurement was determined to be 0.03 *mm.*

To conduct the numerical analysis, commercial software ANSYS-Fluent 18 was used. CLSVOF model was implemented with a 2D axisymmetric approach. Although a cylindrical coordinate system is used by Fluent, for clarity and consistency with the literature, the continuity and momentum equations are given in Cartesian system as:

$$\frac{\partial \rho}{\partial t} + \nabla \times (\rho \vec{v}) = 0 \tag{1}$$

$$\frac{\partial (\rho \vec{v})}{\partial t} + \nabla \times (\rho \vec{v} \vec{v}) = -\nabla \mathrm{P} + \nabla \times [\mu \nabla \vec{v} + (\nabla \vec{v})^T] + \rho \vec{g} + \vec{F_s} \tag{2}$$

in which $\rho, v, P, \text{and } F_s$ are density, velocity, pressure, and surface tension force, respectively. The advection equation for calculating volume fraction of each phase (α) is:

$$\frac{\partial \rho_l \alpha_l}{\partial t} + \vec{v} \times \nabla \rho_l \alpha_l = 0 \tag{3}$$

and volume fraction of the continuous phase is calculated by:

$$\sum_{i=1}^{n} \alpha_i = 1 \tag{4}$$

Density and viscosity of mixture are calculated using the volume fraction of each phase which can be written as:

$$\rho_{mix} = \alpha_l \rho_l + (1 - \alpha_l)\rho_g \tag{5}$$

$$\mu_{mix} = \alpha_l \mu_l + (1 - \alpha_l)\mu_g \tag{6}$$

Since α is almost discontinuous across the interface, the level set method was used to enhance the quality of the local curvatures in constructing the interface through a smooth function.

In the numerical simulation, a 2 *mm* particle was placed at the centre of a 28×8 *mm* domain meshed with initial cells of 0.02 *mm* size in the impact area (see Fig. 2-2). Dynamic refinement was also implemented based on gradients of phase, velocity, and pressure in the domain. The appropriate coordinate system (i.e. cylindrical) is selected according to the parameters set by the user. A 2D axisymmetric simulation reduces the computational cost of the solution; however, the splashed droplets coming off the rim area are not physical as they suggest formation of toroids instead of spherical droplets. It should also be noted that since the Bond number is not too small, the effect of

gravitational acceleration, specifically for the low Weber numbers, might not be negligible. Therefore, the gravity option in Fluent was turned on for all the simulation cases.

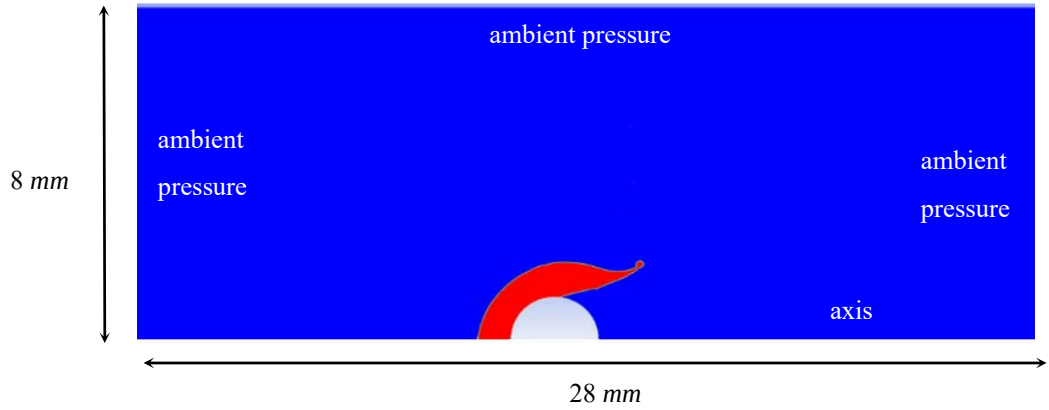

Figure 2-2 *Computational domain and boundary conditions for the droplet-particle impact problem (D_p=2* mm*, D_d=3.3* mm*,* CA=*118°,* We=*1146).*

2.3 RESULTS AND DISCUSSIONS

2.3.1 HYDROPHILIC PARTICLES

Figures 2-3 illustrates droplet impact onto a hydrophilic glass sphere (θ =70°) with different impact velocities. In Fig. 2-3(a), a 3.42 *mm* water droplet collides with a 2 *mm* glass particle (D_r=1.71) with an initial velocity of 0.05 *m/s* (*We*=0.13). For verification of having an on-axis impact, panel A-1 shows the side view of the same impact at the same initial time. Impact of the droplet with the particle is shown in panel A-3 where the droplet gently lands on the hydrophilic glass target (see frames A-4 and A-5) and covers the particle surface completely in panel B-1. Due to the small impact momentum, the liquid bulk does not disintegrate and remains as one. Similar tests were performed for two more cases in which V_0=0.43 *m/s* (*We*=8.8) and V_0=0.95 *m/s* (*We*=38.2), and the results were similar to when *We*=0.13.

Figure 2-3(b) illustrates on-axis collision of a droplet with an impact velocity of 4.91 *m/s* (i.e. *We*=1005). As shown in panels A-3 to B-3, although momentum of the droplet upon impact is much higher compared to the previous case in Fig. 2-3(a), the droplet does not break up during the impact and the collision outcome is similar to *We*=0.13. This is mainly due to high wettability of the target surface; as the droplet keeps moving down, a layer of liquid sticks to the target surface all around the particle keeping the droplet from breaking up or to form a lamella. Since formation of lamella due to its high surface area is not energetically favorable [6], the liquid only slightly deforms around the spherical particle to follow its shape. Suppression of splashing for hydrophilic surfaces in this case is similar to what has been observed for planar surfaces. When a droplet impacts onto a hydrophobic surface, air entrainment lifts the edge of the spreading liquid up the surface and facilitates the splashing, while increasing the surface wettability (i.e. lower contact angles), restrains the onset of splashing. For detailed information on this phenomenon, see section 6 of Ref. [40].

In the hydrophilic region, a similar behavior for the collision outcome was also reported in the literature for impact of a relatively low velocity droplet (*We*~26) onto a spherical target (θ=72°) with a larger diameter compared to the droplet (D_r<1) (see Fig. 10 in Zhang *et al*. [20]). Considering Figs. 2-3(a) and 2-3(b) one can conclude that in on-axis impact of a droplet with a hydrophilic particle, increasing the impact velocity in this range has no significant effect on impact outcomes as surface wettability and liquid cohesion force prevent the liquid disintegration and keep the droplet attached to the particle.

	1	2	3	4	5
A	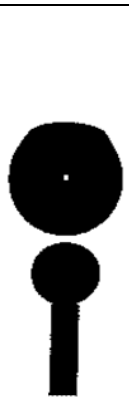	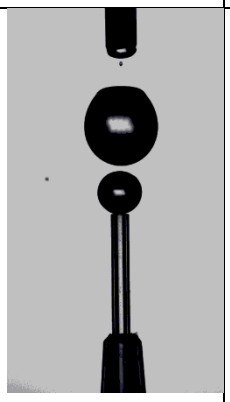	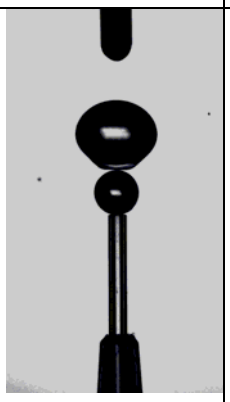	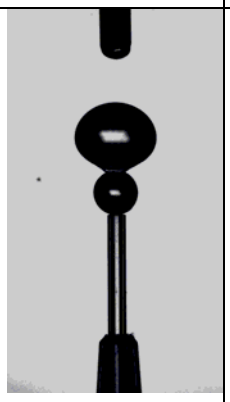	
	t = 0 μs (side view)	t = 0 μs	t = 4571 μs	t = 5286 μs	t = 11428 μs
B	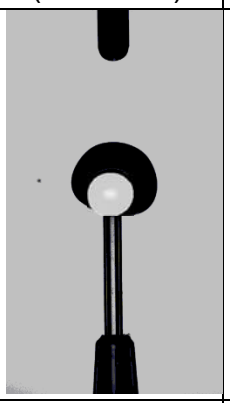	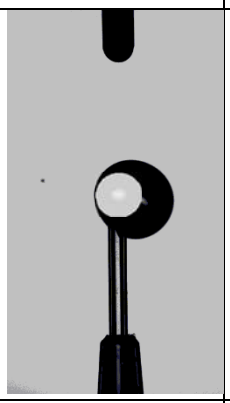	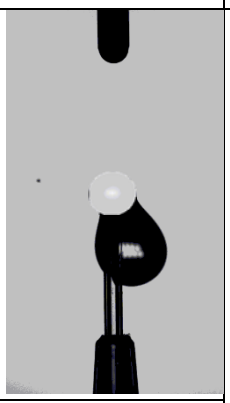		
	t = 12857 μs	t = 18285 μs	t = 44000 μs		

a) D_d = 3.42 *mm*, V_0 = 0.05 *m/s*, *We* = 0.13

(see the next page for caption)

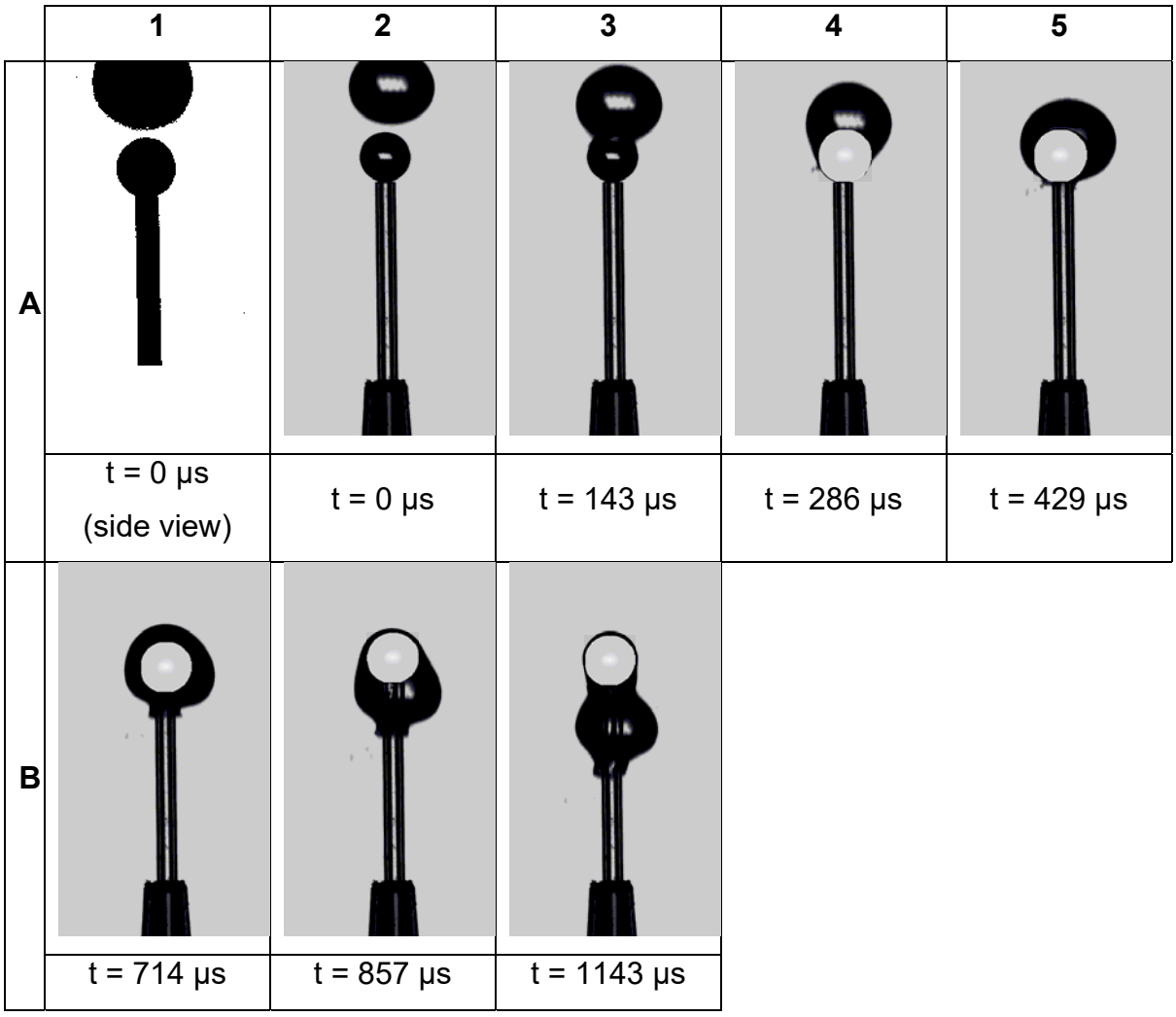

b) D_d = 3.00 *mm*, V_0 = 4.91 *m/s*, *We* = 1005

Figure 2-3 *Impact of a water droplet onto a hydrophilic glass particle (D_p = 2* mm*) with a contact angle of 70˚; a)* V_0 *= 0.053* m/s *(*We*=0.13), b)* V_0 *= 4.91* m/s *(*We*=1005). A grey circle is placed on some of the frames to identify the particle location.*

2.3.2 PARTICLE WITH CONTACT ANGLE OF 90˚

Figure 2-4 shows the droplet collision onto a glass particle having a contact angle of 90˚for different impact velocities. In Fig. 2-4(a), velocity of head-on collision is 0.05 *m/s* (*We*=0.1). The droplet lands gently on the particle as shown in panels A-4 and A-5 and gradually envelopes the target surface. Then, the droplet falls down the particle without

coating the target surface as shown in panels B-2 and B-3. This experiment was repeated for impact velocity of 0.42 *m/s* (*We*=8.6) and collision outcome was similar to Fig. 2-4(a).

When the impact velocity was increased to 2.64 *m/s*, a rim was formed and developed as shown with arrows in panels A-4 and A-5 of Fig. 2-4(b). As the droplet moves down to detach from the particle, a conical shaped structure is formed (see B-1 to B-4 in Fig. 2-4(b)). Assuming axisymmetric liquid bulk in panels A-2 and B-4, image processing for volume measurement showed 32% increase in the apparent volume of the liquid bulk from A-2 to B-4. Considering conservation of volume during the impact, it is deduced that the droplet changes to a liquid film (i.e. lamella) due to the impact.

A similar impact behavior was also observed for a water droplet when the impact velocity was increased to 5.01 *m/s* (see Fig. 2-4(c)). However, due to a higher impact momentum, both lamella height and base diameter were increased and lamella started to open up compared to the results in Fig. 2-4(b). Formation of fingers was initiated at the base of the lamella as shown in panels B-1 to B-3 (see arrows). Finger formation in this impact is similar to what was already observed by Thoroddsen and Sakakibara [41] (for water drop impact onto a glass plate, *We*~1000), or Aziz and Chandra [42] (for impact of molten tin droplets on a stainless steel planar surface, We~600).

For $\theta \simeq 90^{\circ}$, there are a few works in the literature, all in low Weber numbers, in which a small droplet impacts onto a larger spherical target (D_r<1). Therefore, unlike the case shown in Fig. 2-4(a), the droplet does not fall down the particle after impact (see Fig. 2 in Ref. [43] and Fig. 4 in Ref. [19]). For instance, after low velocity impact of a 3.1 *mm* droplet onto a 10 *mm* brass particle (*We*=8), the water droplet was stretched by

impact kinetic energy to its maximum spreading diameter. Then, the liquid starts a recoiling phase, retracts and after some oscillations sits gently on top of the particle.

	1	2	3	4	5
A		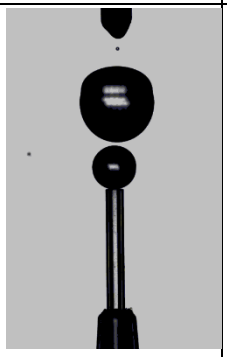	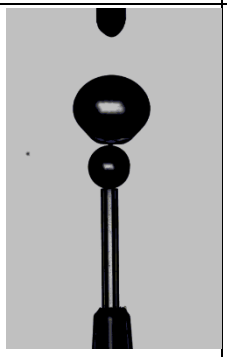	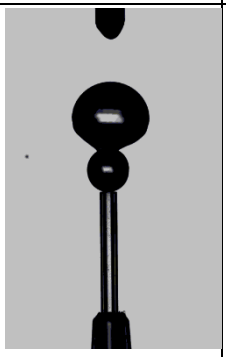	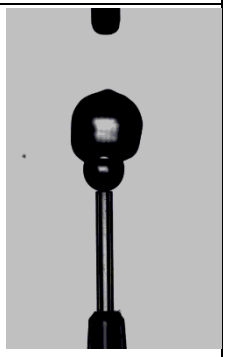
	t = 0 (side view)	t = 0 μs	t = 5143 μs	t = 7000 μs	t = 10428 μs
B		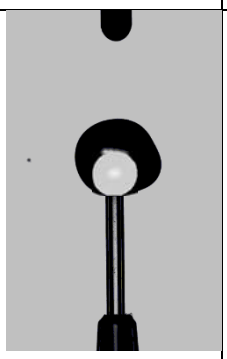	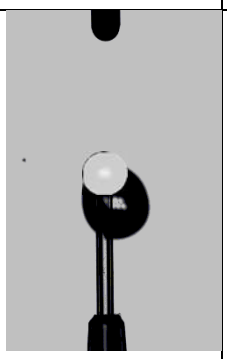		
	t = 17571 μs	t = 28714 μs	t = 60571 μs		

a) D_d **= 3.36** ***mm*****,** V_0 **= 0.05** ***m/s*****,** ***We*** **= 0.1** (see the next pages for caption)

	1	2	3	4	5
A	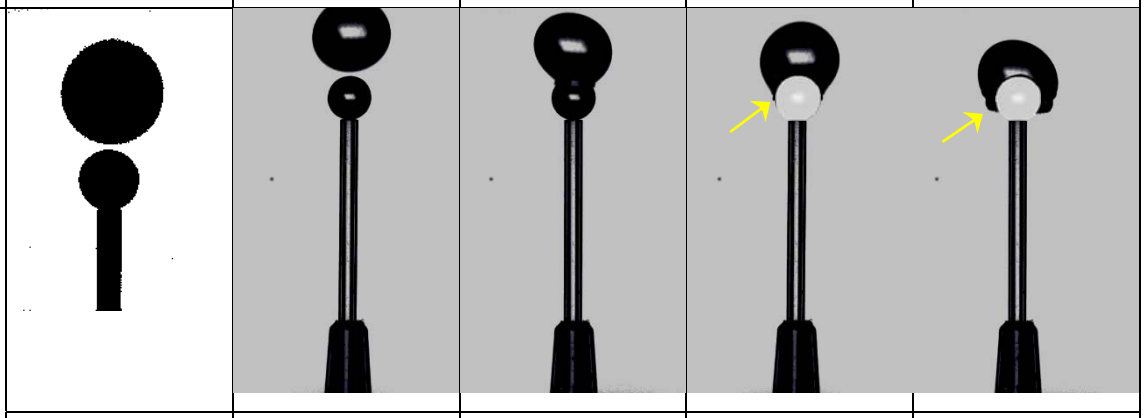				
	t = 0 (side view)	t = 0 μs	t = 143 μs	t = 428 μs	t = 714 μs
B	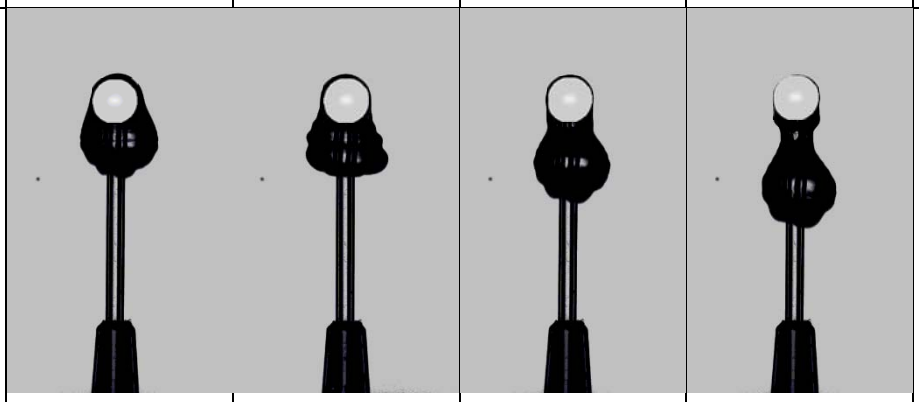				
	t = 1857 μs	t = 2000 μs	t = 2285 μs	t = 2714 μs	

b) D_d = 3.39 *mm*, V_0 = 2.64 *m/s*, *We* = 328

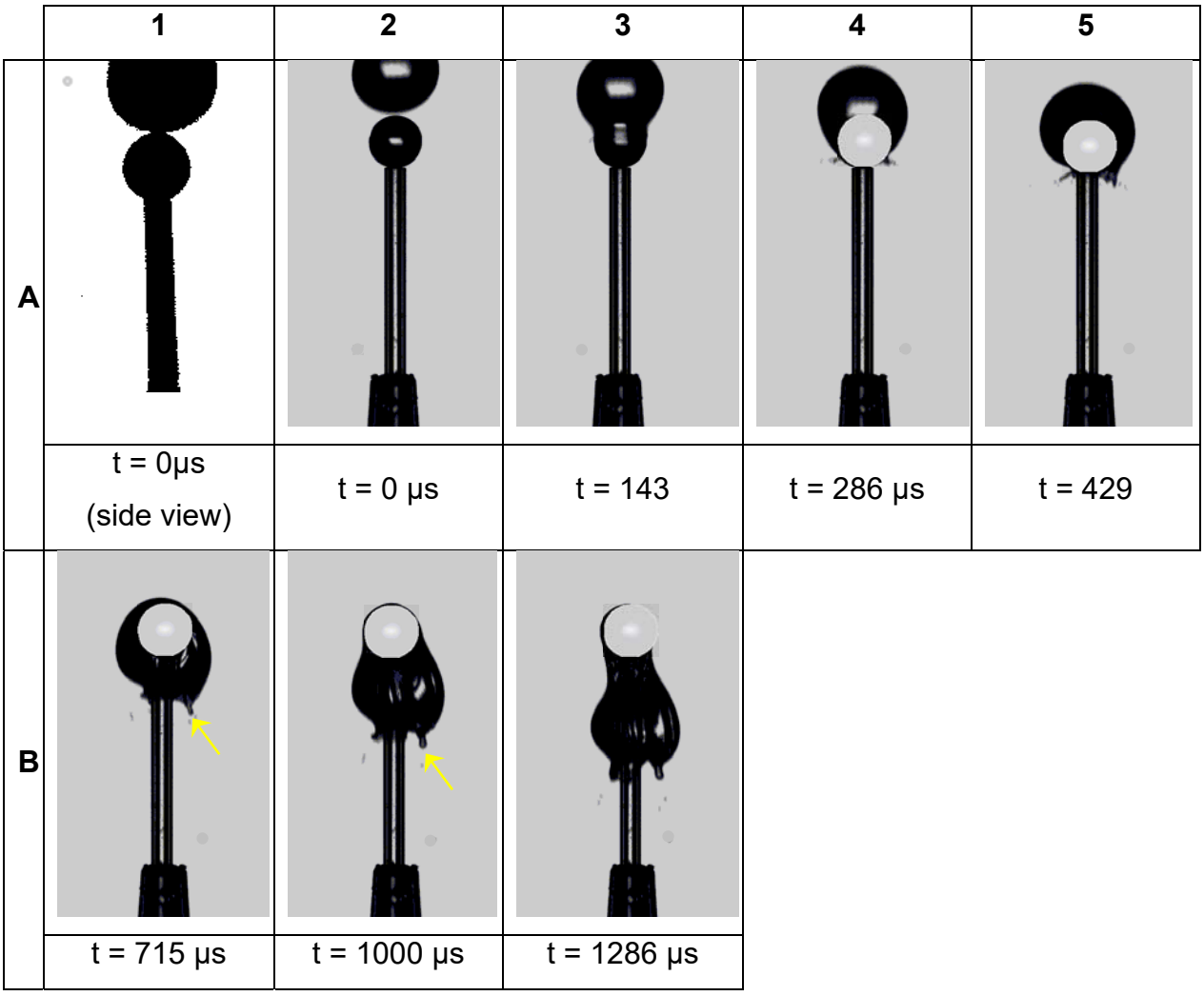

c) D_d = 3.24 *mm*, V_0 = 5.01 *m/s*, *We* = 1133

Figure 2-4 *Impact of a water droplet onto a stationary glass particle (*D_p *= 2* mm*) with a contact angle of 90˚; a)* V_0 *= 0.05* m/s*, b)* V_0 *= 2.64* m/s*, c)* V_0 *= 5.01* m/s*.*

2.3.3 HYDROPHOBIC PARTICLE

2.3.3.1 IMPACT PRODUCTS

Figure 2-5 demonstrates droplet collision onto a glass sphere with a hydrophobic surface (*CA*=118˚) and for different impact velocities. In Fig. 2-5(a), droplet collides onto the particle surface with a relatively low velocity (V_0=0.05 *m/s*, *We*=0.1). As shown in

frames A-3 to A-5, the droplet gently lands on the target and goes through some undulations and deformations on top of the particle for a few milliseconds (frames B-1 to B-3). Finally, the droplet detaches from the glass surface and falls down from the target without disintegration or a substantial deformation. Numerical simulations (2D) by Li *et al.* [13] for a water droplet impact onto a hydrophobic cylinder with a similar Weber number, but with a theoretical contact angle of 170˚ (see Fig. 7 in Ref. [13]) predicts formation of two liquid films in each side of the particle. The liquid films elongated to long and thin fingers as time elapsed and finally the drop was split from the middle. This collision outcome is more similar to what was observed here for higher impact velocities on a spherical target (e.g. see Fig. 2-5(c)). They also predicted no deposition of liquid film on the cylinder after the impact.

When the impact velocity was 0.4 *m/s* (see Fig. 2-5(b)), a collision outcome was observed similar to what was observed in Figs. 2-3(b) and 2-4(b). However, as the droplet-particle contact angle is increased, evolution of the impact product became slower (compare panels *I* to *III* in Fig. 2-6(a)). In general, in the advancing stage, dynamic contact angle increases with the velocity of the contact line. Therefore, for a high contact line velocity, the apparent contact angle can be larger than Young's contact angle (for both hydrophilic and hydrophobic particles). However, when the impact velocity (and therefore contact line velocity) is not high, e.g. as in Fig. 2-6(a), it is quite possible that the equilibrium contact angle plays a role in the droplet deformation. Therefore, for impact onto a hydrophobic particle, the droplet does not tend to spread downwards on the surface of the particle to maintain a contact angle more than 90˚. On the other hand, when particle wettability is high, the interface of droplet and particle should form a hydrophilic

contact angle around the contact line ($\theta < 90^{\circ}$). Therefore, although the droplet touches the particle surface with a contact angle higher than 90° as shown in Fig. 2-6(b), the droplet spreads and moves downward on the particle surface to maintain a hydrophilic contact angle. Since the speed of this contact angle adjustment is higher than the impact velocity, it can facilitate downward motion of the droplet and affect the droplet overall velocity. As the frames timing on Fig. 2-6(a) indicates, more than 75% of discrepancy in time of impact between hydrophilic and hydrophobic cases happens in the initial stage of the impact (i.e. between the impact moment, t=0, and when the droplet passes around the middle of the spherical target, 2nd row images in Fig. 2-6(a)). Therefore, particle wettability affects the impact outcome and this effect is more significant at the earlier stages of the impact.

One can also say that as a water droplet moves around the curve on the bottom half of a hydrophobic sphere, it behaves like a re-entrant structure on which due to high surface tension of water, it is energetically less favourable for the liquid to negotiate the curvature. The reason is that moving down the curve while maintaining a high contact angle requires considerably more stretching of the surface compared to a hydrophilic particle on which the droplet can easily fold downwards to follow the bend. Therefore, evolution time for the impact outcome is relatively shorter for drop collision on a hydrophilic particle compared to that of a more hydrophobic surface as shown on Fig. 2-6(a) (more information about thermodynamic principles of re-entrant structures can be found in Ref. [44]).

As shown in Fig. 2-5(c), when the droplet velocity is increased to 1.8 *m/s*, the lamella starts to appear similar to the case in Fig. 2-4(c). However, for a hydrophobic particle, the lamella was generated at a lower impact velocity (V_0=2.64 *m/s* for *CA*=90° compared to V_0=1.8 *m/s* when *CA*=118°). Formation of a similar lamella due to impact on a spherical target was first reported by Bakshi *et al.* [16], for a 2.6 *mm* droplet of water-glycerine mixture impacted onto a 3.2 *mm* stainless steel particle with a velocity of 2 *m/s* (see Fig. 2-1). Although D_r<1 in their case, a conical liquid film was created since a rim was formed and became larger as the liquid spread over the particle surface. It finally formed a conical lamella by stretching the liquid film downward as the film shrank on the lower half of the target. However, formation of a conical lamella in Fig. 2-5(c) is mainly due to hydrophobicity of the particle which repels the liquid film as it moves on the target, similar to what happens on a flat surface.

The lamellar stretching behavior results from the continuous competition of inertial, viscous frictional, and surface tension forces. Figures 2-5(d) and 2-5(e) illustrate formation of lamella in higher Weber numbers. As droplet impact velocity is increased, both lamella length and base diameter are increased; i.e. the lamella film thickness will be decreased accordingly which will be discussed in detail in the following section. The conical liquid film shown in Fig. 2-5(d) forms a similar lamella compared to the second transitional regime reported in Fig. 3 of Ref. [24].

The lamella shown in Figs. 2-5(d) and 2-5(e) is also similar to what was generated by impact of a water droplet [6] or a droplet of a polymeric solution [7] with the cross section of a cylinder. However, in both above mentioned papers, contact angle did not

play an important role in lamella formation and its cone angle. The reason is that according to Rozhkov *et al*. [6], when a continuous jet impinges the cross section of a cylindrical target with a diameter larger than that of the jet (i.e. $D_r \leq 1$), the liquid film first spreads on the target and then continues spreading into mid-air with an angle of $90°$. Then the lamella film bends downward, and so the cone angle of lamella would be independent of the liquid-target contact angle (see Fig. 4 in Ref. [6]), while in the current case, wettability of the spherical target has a significant effect on impact outcome (compare Figs. 2-3(b), 2-4(c) and 2-5(e)).

As discussed earlier and based on the results presented in Figs. 2-3 to 2-5, three parameters are crucial in lamella formation: 1) hydrophobicity of the particle, which causes the moving liquid on the particle to be repelled from the surface and creates a conical structure; 2) velocity of the droplet, as the droplet should have enough momentum upon impact to be detached from the particle when it is repelled by the particle surface; 3) drop-to-particle diameter ratio; if D_r is too large, particle can be completely captured by the droplet (see Fig. 6 in [22]), while a very small D_r may result in droplet breakup followed by formation of a certain number of liquid fragments (see Fig. 2 in Ref. [22]). In other words, a lamella can only be formed when a droplet impacts onto a hydrophobic particle with an appropriate diameter ratio and impact velocity. Effect of various geometrical parameters on impact outcome and lamella evolution in time will be discussed in the next section.

	1	2	3	4	5
A		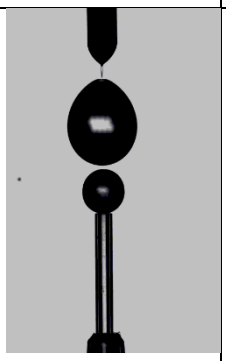	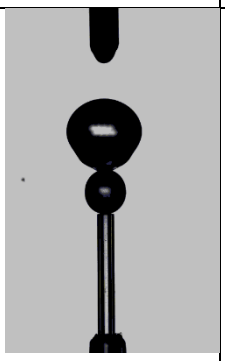	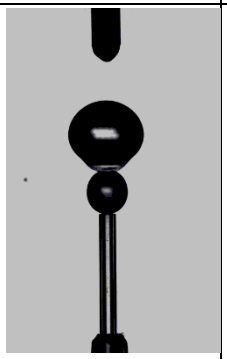	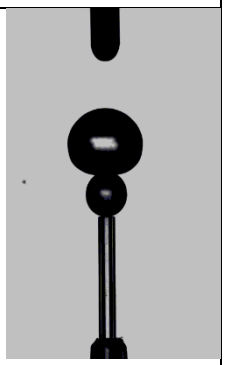
	t = 0 µs (side view)	t = 0 µs	t = 4571 µs	t = 5285 µs	t = 7714 µs
B		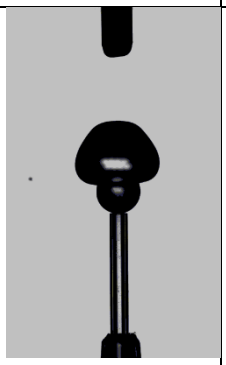	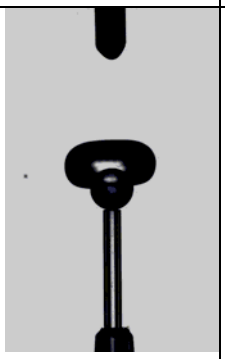	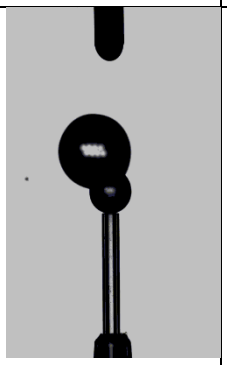	
	t = 27000 µs	t = 43857 µs	t = 56143 µs	t = 70286 µs	

a) D_d = 3.30 mm, V0 = 0.05 m/s, We = 0.1 (see below panel (e) for caption)

	1	2	3	4	5
A	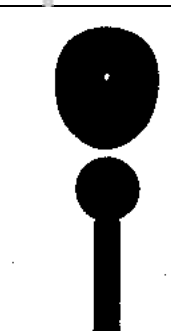			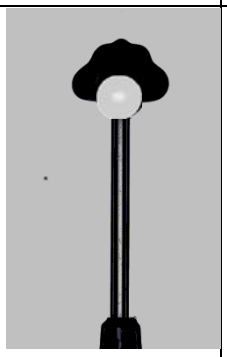	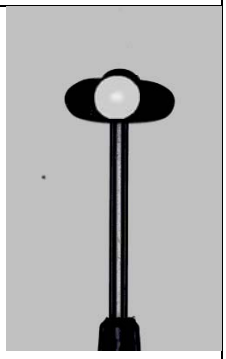
	t = 0 μs	t = 0 μs	t = 2143 μs	t = 6000 μs	t = 10000 μs
B	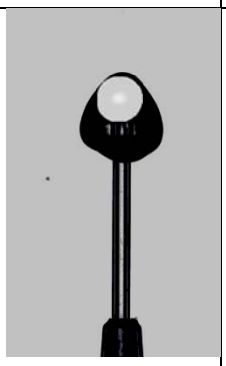				
	t = 14571 μs	t = 19000 μs	t = 30429 μs		

b) D_d = 3.30 *mm*, V_0 = 0.40 *m/s*, *We* = 7.3

	1	2	3	4	5
A		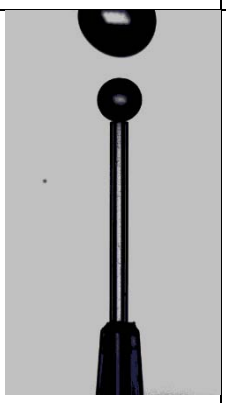	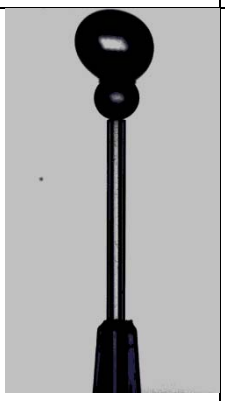		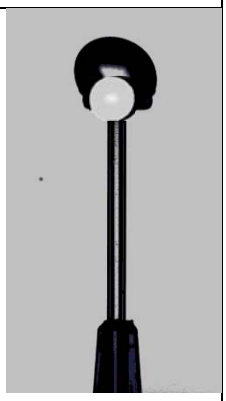
	t = 0 μs	t = 0 μs	t = 714 μs	t = 1000 μs	t = 1428 μs
B					
	t = 1571 μs	t = 2428 μs	t = 3142 μs	t = 4142 μs	t = 4857 μs

c) $D_d = 3.60\ mm$, $V_0 = 1.8\ m/s$, $We = 162$

	1	2	3	4	5
A		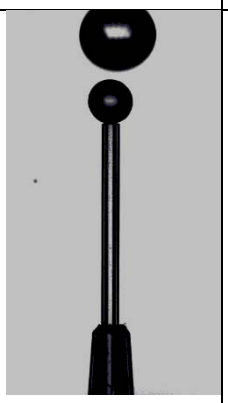	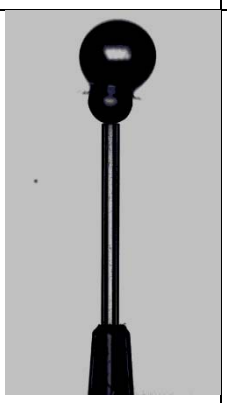	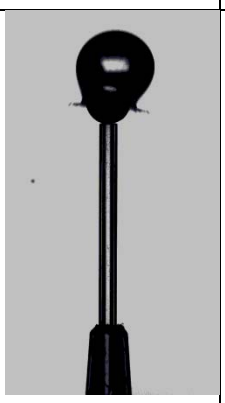	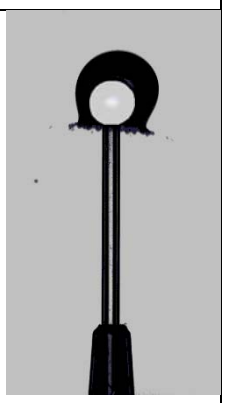
	t = 0 µs (side view)	t = 0 µs	t = 285 µs	t = 428 µs	t = 714 µs
B	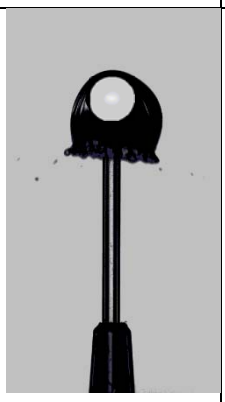			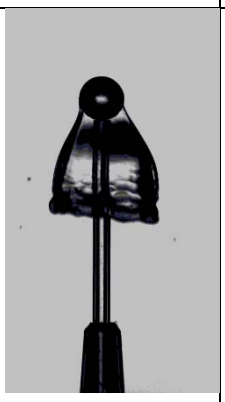	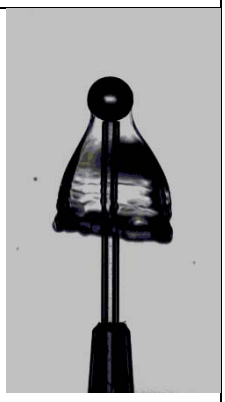
	t = 1142 µs	t = 1428 µs	t = 1714 µs	t = 2000 µs	t = 2285 µs

d) $D_d = 3.30\ mm$, $V_0 = 3.27\ m/s$, $We = 531$

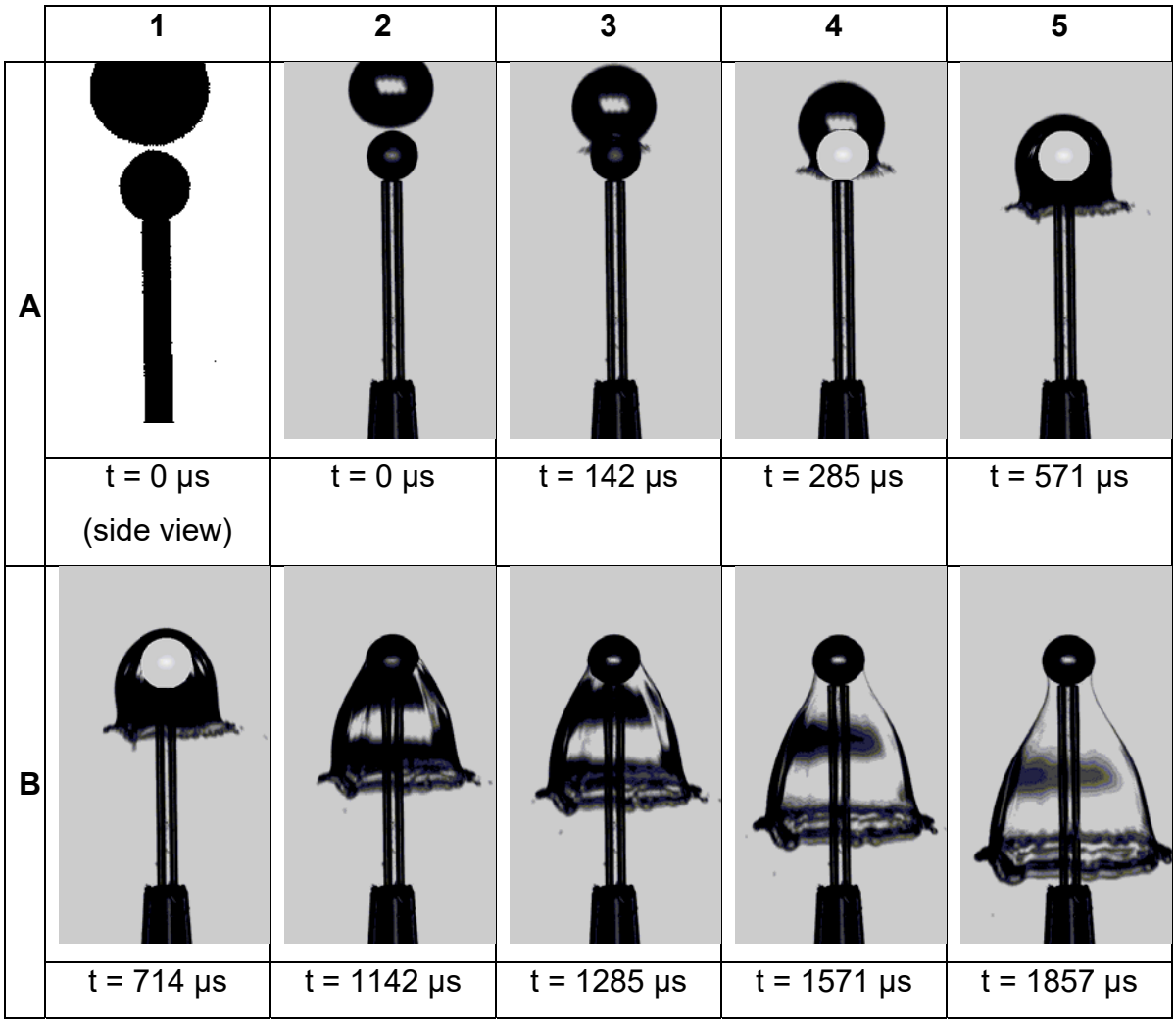

e) D_d = 3.30 *mm*, V_0 = 5.00 *m/s*, *We* = 1146

Figure 2-5 *Impact of a water droplet onto a hydrophobic glass particle (D_p = 2* mm*) with a contact angle of 118 ˚; a)* V_0 *=0.05* m/s*, b)* V_0 *= 0.4* m/s*, c)* V_0 *= 1.8* m/s*, d)* V_0 *=3.26* m/s*, e)* V_0 *= 5.00* m/s*.*

(I) $\theta = 70°$	***(II)*** $\theta = 90°$	***(III)*** $\theta = 118°$
D_d = 3.42 *mm* V_0 = 0.43 *m/s* (*We* = 8.8)	D_d = 3.51 *mm* V_0 = 0.42 *m/s* (*We* = 8.6)	D_d = 3.30 *mm* V_0 = 0.40 *m/s* (*We* = 7.3)
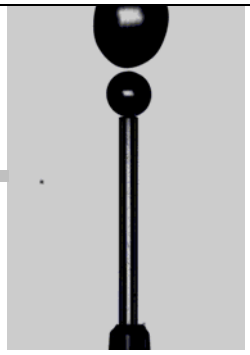	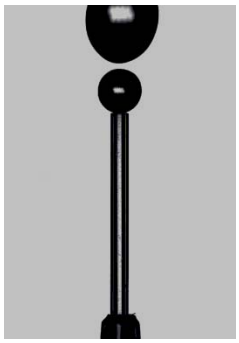	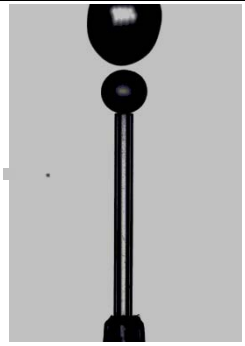
t = 0 µs	t = 0 µs	t = 0 µs
 t = 2857 µs	 t = 4714 µs	
		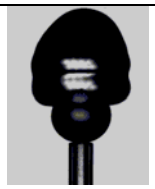 t = 3285 µs
		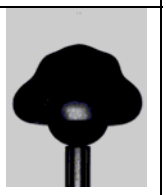 t = 6428 µs
		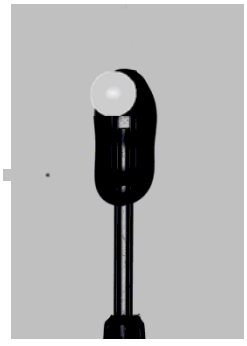
t = 16715 µs	t = 17714 µs	t = 19000 µs

(a)

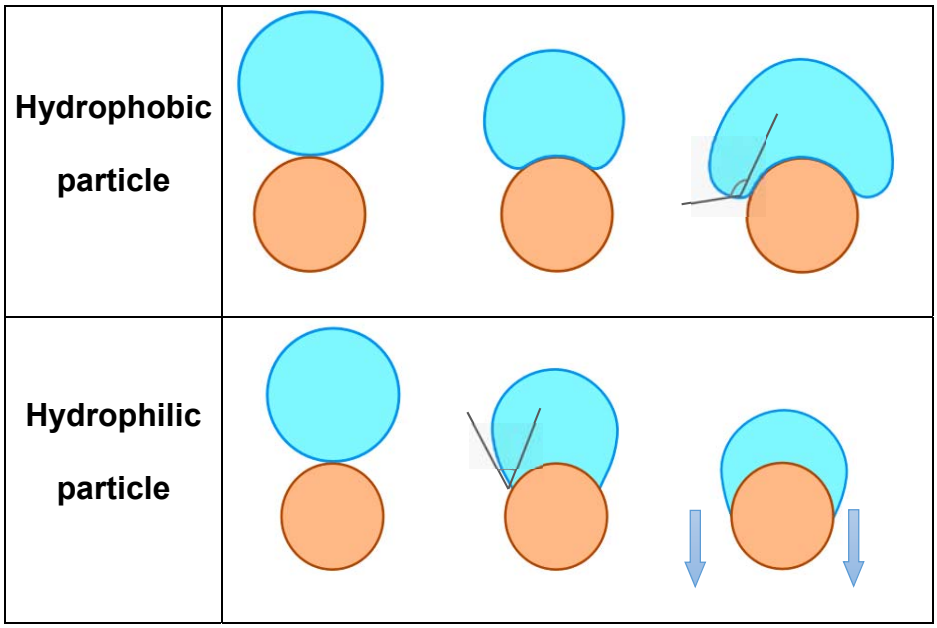

(b)

Figure 2-6 *a) Comparison of the elapsed time for evolution of impact outcome for various particle wettabilities, b) effect of particle wettability on downward motion of the droplet.*

Droplet impact onto a stationary particle quantified with a timescale is shown in Fig. 2-7. This diagram includes impact on both hydrophilic and hydrophobic particles. This illustration can be used for comparison of temporal evolution of the collision outcomes. For instance, one may compare the frames in two columns at $We \approx 10$ and achieve the same conclusion made from Fig. 2-6(a) (i.e. for low impact velocities, impact outcome on a hydrophobic particle needs more time to evolve compared to impact on a hydrophilic target).

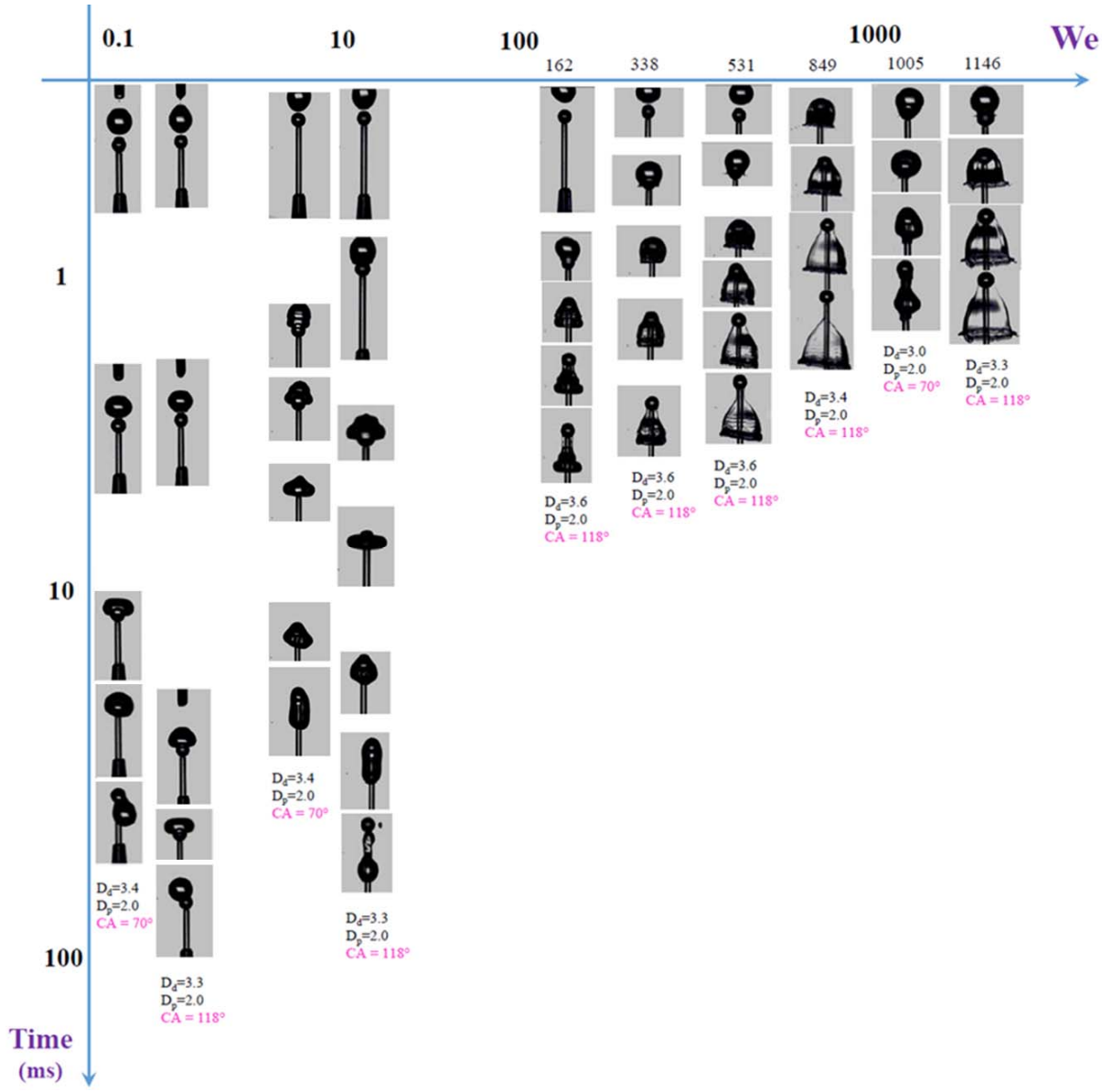

Figure 2-7 *Time evolution of the impact versus Weber number showing the morphology of droplet impact onto hydrophilic and hydrophobic particles*

2.3.3.2 LAMELLA ANALYSIS

Figure 2-8(a) illustrates the geometrical parameters of the liquid bulk and lamella in an intermediate stage of the impact, i.e. lamella base diameter (D_b), lamella height (H), and height of the remaining liquid on the particle (h). It should be noted that for lamella

height measurement, the reference point for *H* when the droplet was feeding into the liquid film was the apex of the lamella as shown in Fig. 2-8(a). However, when there was no more liquid on top of the particle (i.e. $h \approx 0$), the line that connects the lamella to the particle became the reference point for *H* which started moving downward on the particle surface until lamella detachment.

Figure 2-8(b) shows variations of the lamella base diameter over time in dimensionless form for various Weber numbers. Diameter and velocity of the droplet just before the impact were used for defining non-dimensional numbers (D^*= $\frac{D_b}{D_d}$, $t^* = \frac{tV_0}{D_d}$). For a given Weber number within the range of impact velocity in which a lamella forms, the base diameter of the lamella increases with time; and as Weber number is increased at a constant dimensionless time, D^* increases accordingly. The same behaviour was shown for droplet-particle impact in mid-air (see Fig. 6-a in Ref. [24] in which lamella base diameter increased with a constant rate as Weber number was increased). Moreover, by increasing the Weber number, Fig. 2-8(b) shows that non-dimensional time at which the lamella is detached from the particle is increased. Detachment points are marked with red diamonds in Fig. 2-8(b). Figure 2-6(b) in Ref. [24] indicates an increase in duration of the lamella growth phase as Weber number is increased (for impact in mid-air) which agrees with the present results for a still particle considering the position of diamonds shown with a dashed-line on Fig. 2-8(b).

Within the lamella formation process, a function with general form of

$$D^* = a - \frac{a}{1 + \left(\frac{t^*}{b}\right)^n} \tag{7}$$

can replicate D^* versus time. Coefficients *a* and *b* are adjusting parameters and so are different for various Weber numbers. However, the power *n* remains the same for all cases in which a fully open lamella is formed. Based on the experiments and simulation results performed in various impact velocities for the droplet and particle size presented in Fig. 2-5, a fully open lamella forms while the droplet impact velocity is in the range of 4 to 9 *m/s*. In this range, the power *n* is determined to be 0.42 ±0.02.

Equation 7 is an empirical relationship which shows a maximum error of 6% with the experimental data and is consistent with physics of the phenomenon. The lamella base diameter starts from zero (i.e. $t^* = 0$ for the impact moment) and approaches to an asymptotic value when $t^* \gg 1$ which is in agreement with what was reported for drop-particle impact in mid-air as an independent set of data (see Fig. 5 in Ref. [24]).

Figure 2-8(c) shows the growth in the base diameter of two lamella cases resulted from drop impact onto cylindrical objects (from literature), compared to impact onto a spherical target (current work) at the same Weber numbers but different diameter ratios. Some of the images of the corresponding impact phenomenon are shown on each curve. As illustrated in Fig. 2-8(c), the general formulation presented for drop impact on a sphere in Eq. (7) can accurately predict the results of impact on a cylindrical target as well (compare two solid-line curves on Fig. 2-8(c) with the corresponding dashed-lines).

In Rozhkov *et al*. [6] and Juarez *et al*. [9], droplet and cylindrical target had the same diameter (D_r~1), while in the current experiments, the drop-to-particle diameter ratio is significantly larger (D_r=1.75). By comparing the lamella cone angles (2ψ) on Fig. 2-8(c), one can conclude that as D_r decreases, at a constant Weber number, the lamella

forms with a larger cone angle. The reason is that when D_r is small, the particle diameter would be relatively larger and on a larger particle, the point from which lamella detaches from the particle surface moves upward. Therefore, for a smaller D_r, a larger cone angle would be created while lamella is formed (either on a spherical particle or on cross section of a cylindrical target). As a result, lamella base diameter is generally larger in the results presented by Ref. [6] and Ref. [9] (D_r~1) compared to the current work (D_r=1.75). The temporal rate of increase in base diameter is also relatively larger for cylindrical objects compared to the spherical targets.

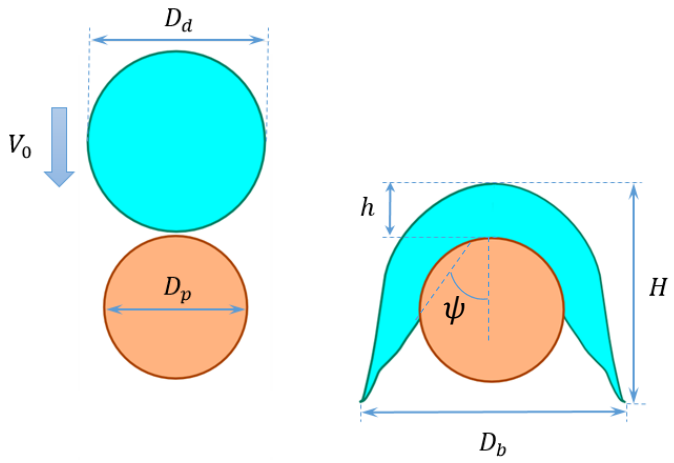

(a)

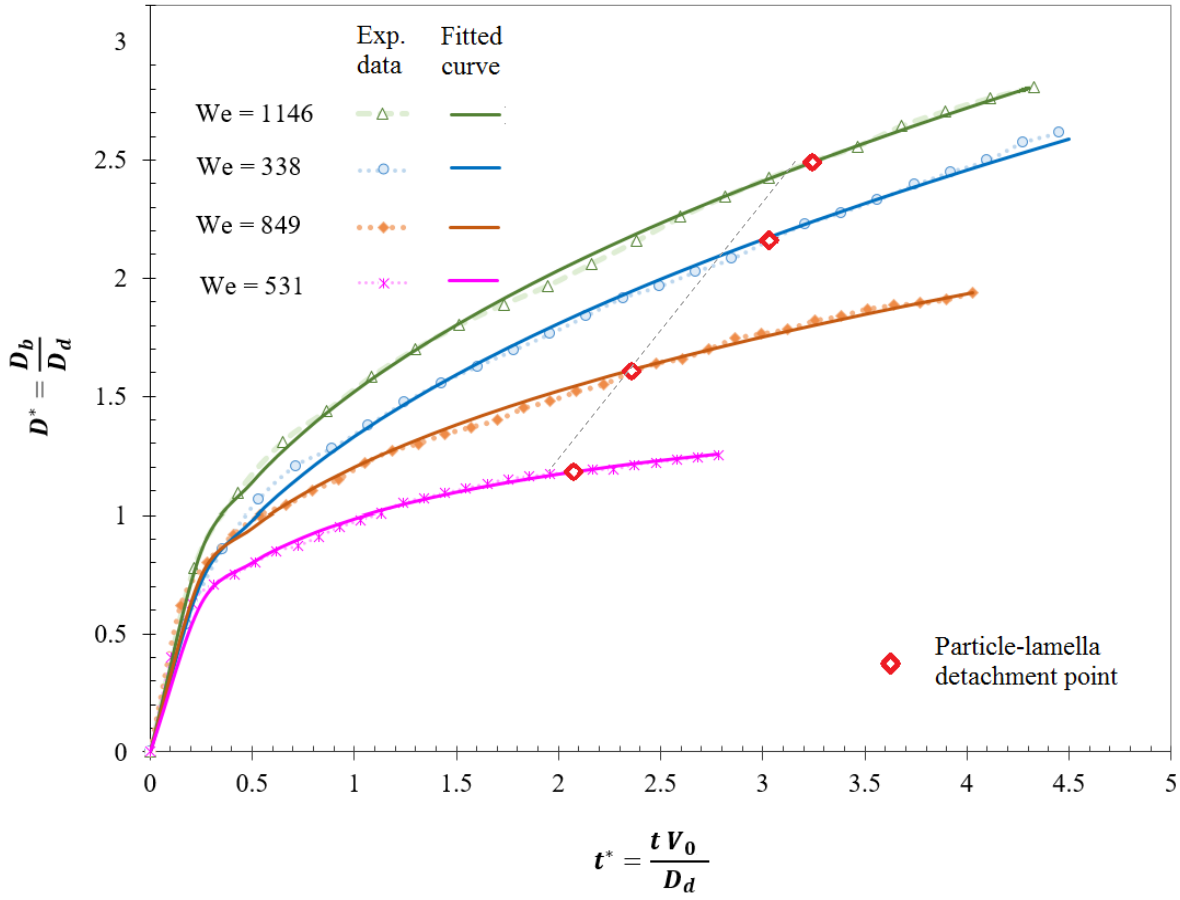
Exp. data
Fitted curve
We = 1146
We = 338
We = 849
We = 531
Particle-lamella detachment point
$D^* = \frac{D_b}{D_d}$
$t^* = \frac{t\,V_0}{D_d}$
0
0.5
1
1.5
2
2.5
3
3.5
4
4.5
5

(b)

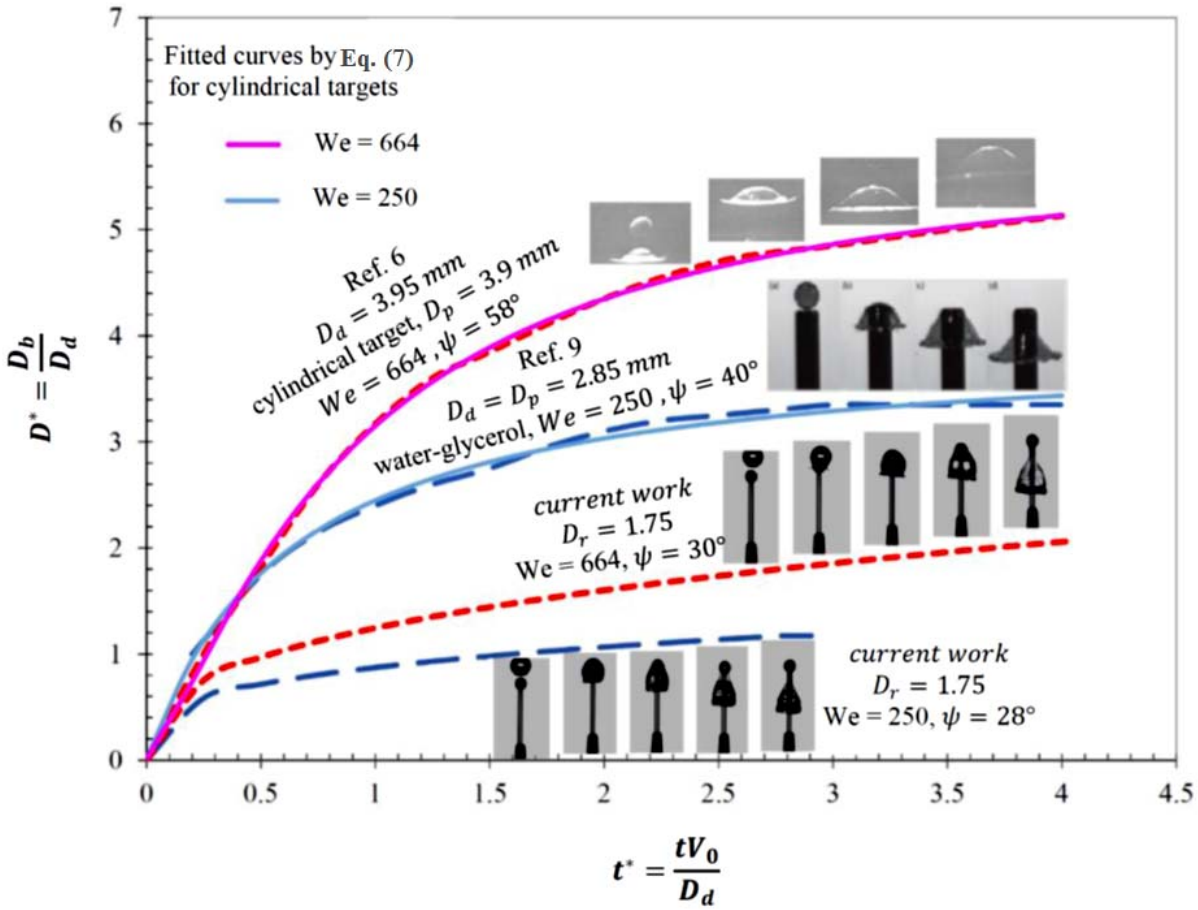

(c)

Figure 2-8 *a) Geometrical parameters of the lamella and liquid bulk in drop impact onto a spherical particle, b) variations of dimensionless lamella base diameter versus time, c) dimensionless lamella base diameter: drop impact onto a cylindrical object compared to the impact with a spherical target. Reproduced from Phys. Fluids 14, 3485-3501 (2002), with the permission of AIP Publishing. Reproduced with permission from Phys. Rev. E 85, 026319 (2012). Copyright 2012 American Physical Society.*

In collision of a water droplet with a hydrophobic spherical target, height of the remaining liquid on the target is assumed to be a function having the following governing parameters:

$$h = f\left(D_d, t, D_p, V_0, \theta\right) \tag{8}$$

However, dependency of *h* on the droplet-particle contact angle (θ) should be investigated while its dependency on the rest of parameters is clear. Creating glass particles in the entire range of contact angles (especially in hydrophobic region) for doing experiments is difficult, if not impossible. Therefore, experiments were only implemented for some contact angles and numerical analysis was used to augment the existing gaps in studying the effect of θ on the collision outcomes. Figure 2-9(a) shows phase volume fraction contour plot of simulation results for a water drop impact onto particles with three different wettabilities. Red color in simulation results shows the liquid, and the blue area denotes the gas phase. The corresponding experimental results have also been provided for comparison which illustrates capability of the numerical model to capture the effect of droplet-particle contact angle on the impact outcomes.

To investigate the effect of particle wettability on the lamella formation (i.e. when θ > 90°), a series of simulations were done with different particle wettabilities in which a 3.3 *mm* water droplet with an initial velocity of 5 *m/s* impacted onto a 2 *mm* solid particle. Figure 2-9(b) shows the phase diagram of the simulation results for each case in which impact outcome was captured at the moment of lamella detachment from the particle. Three geometrical parameters of the lamella were measured including lamella length, base diameter, and the cone angle of the lamella (2ψ). The results are summarized in Fig. 2-9(c) and it illustrates that there is, in fact, a threshold for wettability (i.e. θ =110°) after which variations of the contact angle does not have a significant effect on the lamella geometry. Therefore, for a strongly hydrophobic particle one may rewrite Eq. (8) as $h = f(D_d, t, D_p, V_0)$in which only two of the parameters have independent basic units (we take D_d and t). Using Π-theorem, one can define the following non-dimensional groups: $\Pi =$

$\frac{h}{D_d} = h^*$, $\Pi_1 = \frac{V_0 t}{D_d} = t^*$, $\Pi_2 = \frac{D_p}{D_d}$. So, the height of the remaining liquid on target can be expressed as $\frac{h}{D_d} = \mathcal{F}\left(\frac{V_0 t}{D_d}, \frac{D_p}{D_d}\right)$ which in the case of using single-diameter particles and droplets (D_p=2.0 mm and D_d=3.3 mm for hydrophobic particles at We>250) will be simplified as:

$$h^* = \mathcal{F}(t^*) \qquad (9)$$

$\theta_{eq} = 70°$ $\theta_{eq} = 70°$ V_0 = 4.91 *m/s*	$\theta_{eq} = 90°$ V_0 = 5.01 *m/s*	$\theta_{eq} = 118°$ V_0 = 5.00 *m/s*
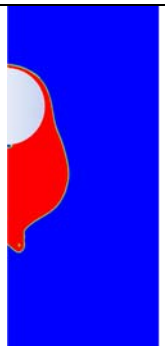	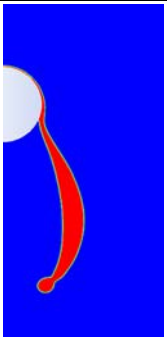	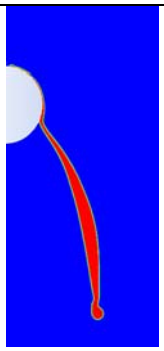
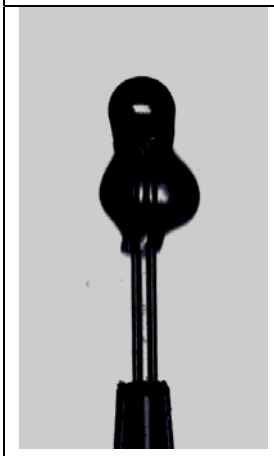	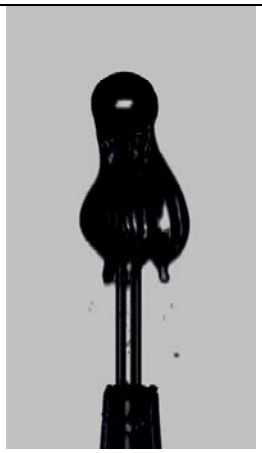	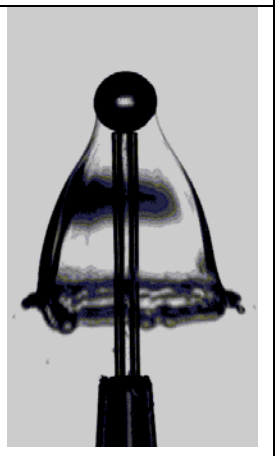

(a)

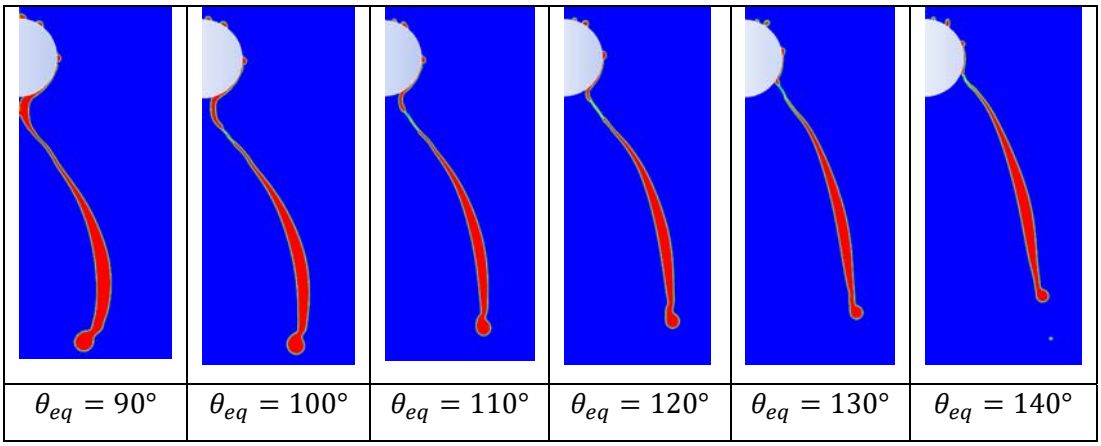

(b)

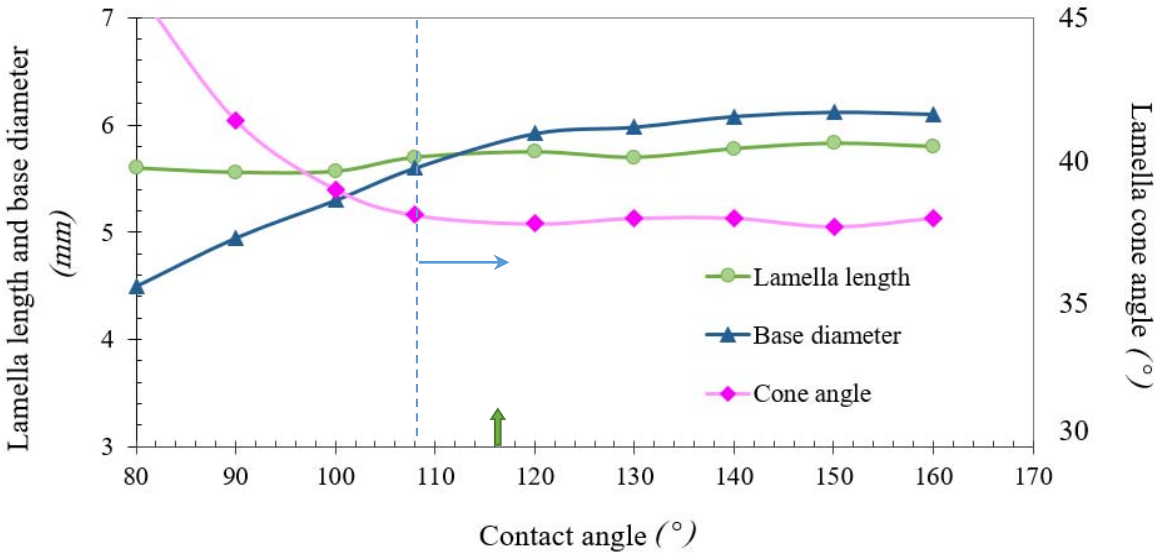

(c)

Figure 2-9 *Lamella geometry for droplet impact onto a stationary spherical target*; *a) comparison of simulation and experimental results for hydrophilic and hydrophobic particles, b) fully formed lamella just before detachment from particles with different wettabilities (D_d=3.30* mm, *D_p=2.0* mm, *V_0=5.0* m/s*), c) effect of contact angle on three main geometrical parameters of a fully formed lamella (θ_{eq} >125° are hypothetical values used for simulations as was done by* Li *et al.* [13]*).*

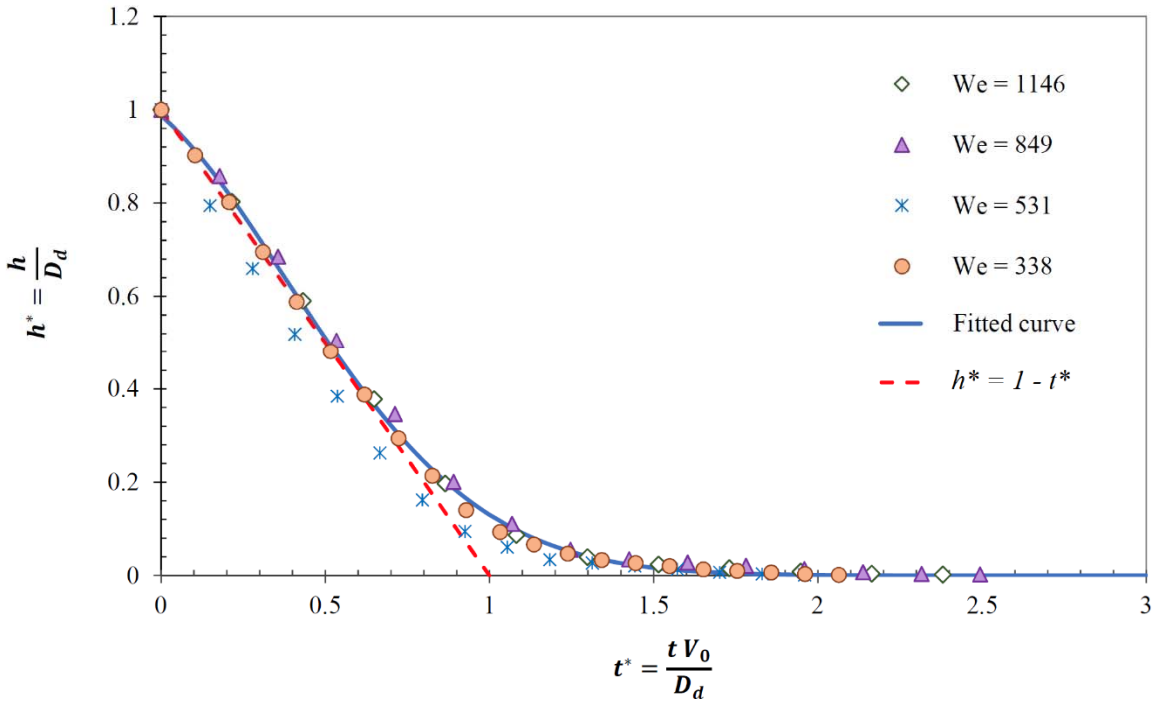

Figure 2-10 *Dimensionless height of remaining liquid bulk on top of the solid surface versus time.*

Looking back at Fig. 2-8(a), the droplet touches the particle surface with the velocity V_0. One may assume that the droplet velocity remains unchanged during the impact. In other words, the portion of the liquid on top of the particle keeps moving down with the initial impact velocity (V_0). This assumption is used commonly in other works (e.g. see Eq. (13) in Ref. [45]). Therefore, the temporal equation for height of the remaining liquid on the particle during the impact would be:

$$h = D_d - V_0 t \tag{10}$$

which in non-dimensional form can be written as:

$$\frac{h}{D_d} = 1 - \frac{V_0 t}{D_d} \tag{11}$$

$$h^* = 1 - t^* \tag{12}$$

Variation of non-dimensional height of the remaining liquid versus dimensionless time is shown in Fig. 2-10. For all Weber numbers, the height of the liquid bulk on the particle surface decreases as droplet moves down over time. All the experimental data in various Weber numbers overlap on a single curve. The reason is that magnitude of h^* is inversely proportional to both the elapsed time and the impact velocity, i.e. by increasing V_0, the time t at which h^* reaches a certain value will be accordingly decreased. Therefore, tV_0 remains unchanged regardless of the variations of droplet velocity during the impact. In other words, h^* for each specific $t^* = tV_0/D_d$ remains on the same curve for all impact velocities (Weber numbers). The dashed line on Fig. 2-10 represent an approximation of Eq. (12) which shows a good agreement with the experimental data. However, the best fit achieved with the experimental results is the master curve shown with the solid line. The reason for deviation from Eq. (12) is that near the end of the process where h is tending to zero, the constant velocity assumption does not hold any longer. The master curve on Fig. 2-10 is represented by the following equation:

$$h^* = ae^{\frac{-(t^*-b)^2}{c}} \tag{13}$$

in which the coefficients were determined to be $a = 1.06, b = -0.22$ and $c = 0.71$. It is worth mentioning that the maximum time scale for droplet impact onto a spherical target is determined as t_{max}=2.5 in which the droplet is transformed into a lamella (i.e. h→0 based on the experimental data shown on Fig. 2-10). It is possible that a liquid film with

a small thickness remains on the particle, but it is not detectable with our imaging system, so a zero asymptote was considered for the *h** as an approximation.

Since t^*_{max} is independent of the impact velocity, one may compare this to the time scale for maximum spreading of a droplet on a flat surface presented by Pasandideh-Fard *et al*. [45] in which $t^*_c = \frac{8}{3} = 2.67$.

Mitra *et al.* [47] also studied residual film thickness when a droplet impacts a highly conductive particle with size ratio near unity in the presence of heat transfer between particle and droplet. They found that temporal evolution of film thickness was almost unaffected by heat transfer. When plotting variations of the liquid film thickness over time, they identified three distinct regimes. A linear reduction in film thickness was observed, at the first stage of impact, similar to what is shown by Eq. (12). However, caution should be taken in comparing their results to what is presented in Fig. 2-10 due to the significant difference in droplet-to-particle diameter ratio (~0.85 in Ref. [47] compared to 1.75 in the present work), and the range of Weber numbers.

Figure 2-11 illustrates variations of dimensionless lamella height (i.e. $H^* = \frac{H}{D_d}$, see Fig. 2-8(a)) versus time for four different impact velocities. Each curve is related to a Weber number and consists of two parts. In the ascending section of the curve, the lamella is stretched since the droplet kinetic energy still overcomes all resistance sources including shear stress between particle and droplet, viscous dissipation inside the lamella, and the increase in surface energy due to increase of film surface area. However, in the descending part of the curve, the lamella shrinks to reduce the surface energy (i.e. to

reach an energetically favourable state). Note that the jump seen on each curve is an artifact of changing the reference point for measuring *H* as already explained.

A similar dimensional analysis presented for h^* in the previous section, can be used to explain the behaviour of lamella height (*H*). Lamella height is proportional to both the initial velocity (V_0) and the duration of impact (*t*). Therefore, in the non-dimensional form, H^* would be only a function of t^*. In other words, for various Weber numbers, there should be a single curve to represent stretching of the lamella. As experimental data on Fig. 2-11 indicates, in the ascending section, H^* is the same for all impact velocities, and so the curves overlap and can be represend by a single curve fitted to all the data from various Weber numbers with the following equation:

$$H^* = a - \frac{b}{1 + \left(\frac{t^*}{c}\right)^d} \tag{14}$$

in which $0 < t^* < 3$ and $a = 3.5$, $b = 2.5$, $c = 2.38$ and $d = 2.93$. Equation (14) is only for the ascending section of the plot. The maximum point on this curve that can be reached while lamella is stretched (i.e. H^*_{max}), depends on the impact velocity of the droplet. Therefore, the point from which lamella stops stretching and starts retracting tracks higher on the general curve as the Weber number is increased. This explains why in spite of having the same temporal rate of decrease for H^* (i.e. all descending curves are parallel), there is a separate retraction curve for each Weber number. The red diamonds in Fig. 2-11 indicate the detachment point of the lamella from the solid particle in each Weber number. As droplet impact velocity is increased, the lamella detachment takes place in a larger non-dimensional time *(t^*)*.

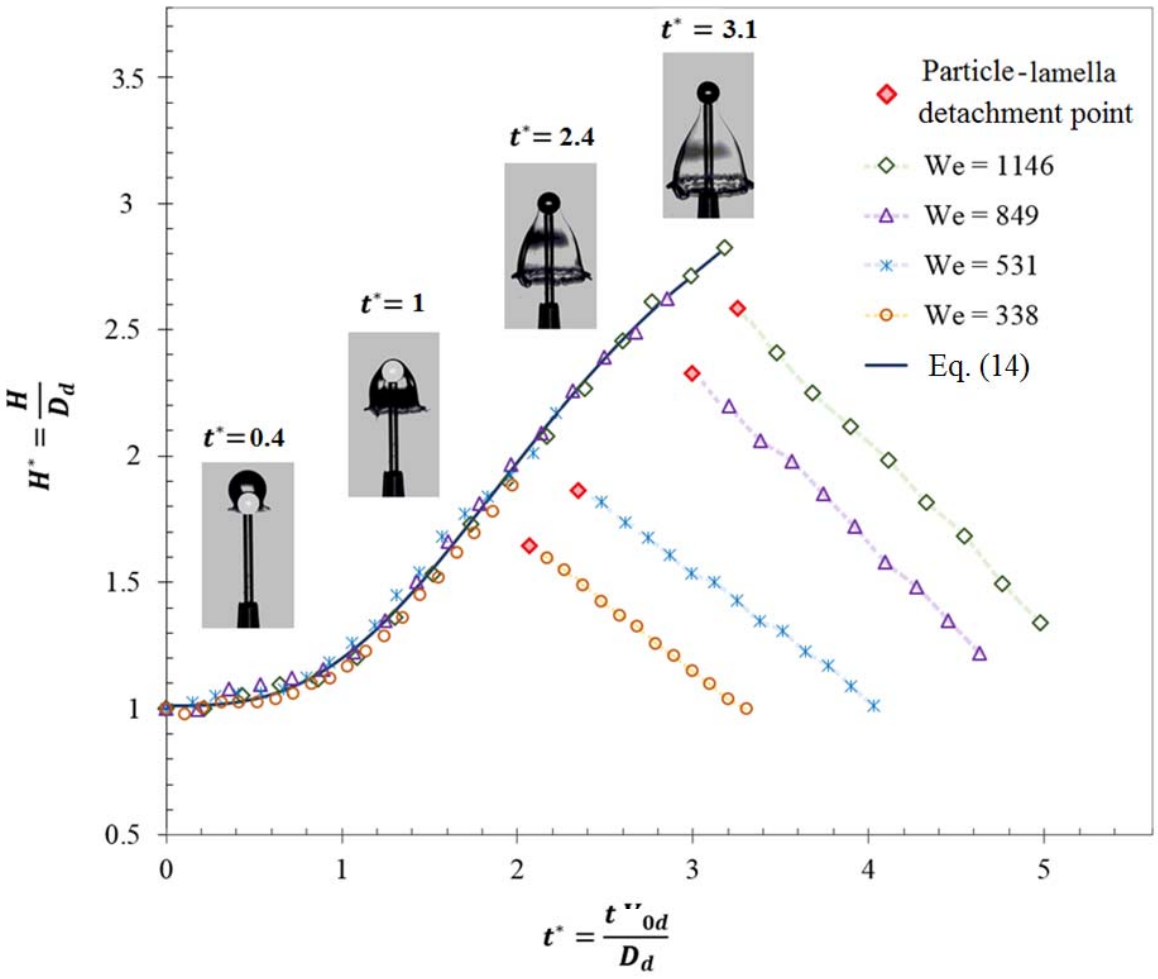

Figure 2-11 *Dimensionless variations of lamella height versus time in different Weber numbers. Frames illustrate lamella evolution for* We*=1146 at the corresponding times.*

The outcome of the current study can be used to predict collision products in similar impact cases. For the system studied here and the given particle geometry, having Figs. 2-8(b), 2-10 and 2-11 one would be able to find the geometric characteristics of the impact outcome (i.e. lamella length, base diameter, and height of the remaining liquid) for different times and various water droplet velocities.

Figure 2-12 illustrates a pictorial map of the literature for droplet impact onto a still spherical particle completed with the results of the current study (only impact on a

hydrophobic particle). This map enhances the literature in three ways. First, by filling the gaps between those Weber numbers previously studied in the literature. Secondly, by extending the range of Weber number by three times (i.e. We_{max} was increased from 356 in the literature to 1146). Thirdly, this is the first systematic study for droplet impact onto a still particle in which droplet-to-particle diameter ratio (D_r) is more than one and effect of particle wettability on impact outcomes is also investigated. As shown in Fig. 2-12, such a diameter ratio creates new impact products even in the range of Weber numbers that was already studied in the literature (e.g. see We=338 on the map).

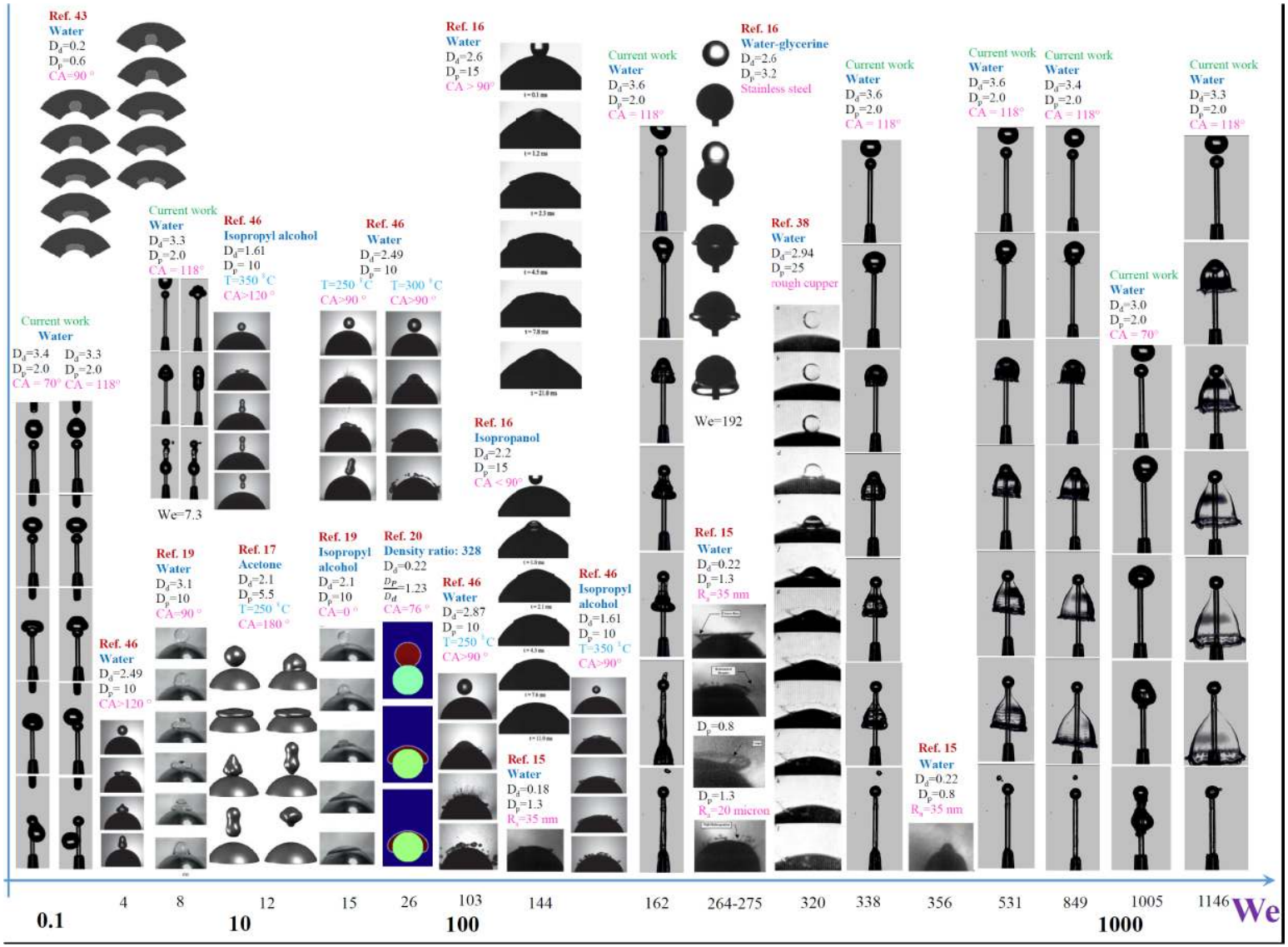

Figure 2-12 *Illustrative map of all existing works on droplet impact onto a still spherical particle; current work fills the gaps and extends the Weber number limit (Ra=surface roughness, CA=contact angle; all diameters are in mm). Reproduced from Phys. Fluids 19, 032102 (2007), with the permission of AIP Publishing. Reproduced with permission from: Chem. Eng. Sci. 149 (2016). Copyright 2016 Elsevier Ltd; Chem. Eng. Sci. 100 (2013). Copyright 2013 Elsevier Ltd; J. Fluid Mech. 573 (2007). Copyright 2007 Cambridge University Press; Int. J. Heat Fluid Flow 20 (1999). Copyright 1999 Elsevier Science Inc; Math. Phys. Eng. Sci. 269 (1971). Copyright 1971 The Royal Society; J. Vib. Shock 31, 20 (2012). Copyright 2012 Zhongguo Zhendong Gongcheng Xuehui; Int. J. Therm. Sci. 84 (2014). Copyright 2014 Elsevier Masson SAS.*

2.4 CONCLUDING REMARKS

Collision of a droplet onto a still spherical particle was experimentally studied. Droplet to particle diameter ratio has a significant effect on the impact outcomes, and based on the literature survey, D_d/D_p~1.75 was the subject of investigation in this work. Three main aspects of the phenomenon were studied and the conclusions are explained below.

1) Regarding the impact outcomes for particles of different wettabilities at various impact velocities we found that: For drop impact onto a hydrophilic particle, the droplet is neither disintegrated nor stretched enough to form a liquid film after impact. In fact, those deformations are not energetically favorable (regardless of the gravity, since no external force applied to the droplet and particle, the system seeks to reaching to the minimum energy state). Therefore, the droplet follows the particle curvature and slightly deforms around it in the entire velocity range studied here. However, starting from We~200 for impact on a hydrophobic particle, a liquid film forms as a result of the impact. As the Weber number is increased, the lamella length and cone angle are increased accordingly.

Furthermore, it was found that the lamella height and base diameter in dimensionless form (H^* and D^*, respectively) increases over time while height of the remaining liquid on the particle (h^*) decreases. For the entire range of impact velocity in which a lamella is formed, all h^* values overlap on a single curve. Likewise, there is a master curve for H^* at various Weber numbers in lamella stretching phase; the maximum stretching of lamella depends on the droplet velocity upon impact. Moreover, the empirical relation developed for D^* is shown to be valid beyond the current study as it can also

predict the impact outcome on similar curved surfaces from other works (e.g. Ref. [6] and Ref. [9] in Fig. 2-8(c)).

2) Regarding the effect of particle wettability on impact duration, we found that as particle wettability is increased, the elapsed time during the impact is decreased accordingly. When the particle is hydrophobic, for impact velocities larger than 1.8 *m/s* (*We*>162), the droplet creates a thin liquid film after impact. In fact, hydrophobicity of the particle repels the liquid from the surface and causes the droplet to form a conical lamella as it spreads on the particle. This mechanism is mainly effective at the initial stage of impact and before particle penetrates completely into the liquid.

3) Regarding the effect of contact angle variations on lamella geometry for hydrophobic particles, we found that increasing the contact angle from hydrophilic to hydrophobic zone has a considerable effect on geometry of the liquid film and lamella formation. However, increasing the contact angle of a hydrophobic particle after the threshold value of 110° does not have a significant effect on lamella geometry.

2.5 REFERENCES

[1] C. D. Stow and M. G. Hadfield, “An experimental investigation of fluid flow resulting from the impact of a water drop with an unyielding dry surface,” Proc. R. Soc. London A: Math. Phys. Eng. Sci. 373, 419-441 (1981).

[2] Fukai, Z. Zhao, D. Poulikakos, C. M. Megaridis, and O. Miyatake, “Modeling of the deformation of a liquid droplet impinging upon a flat surface,” Phys. Fluids A 5, 2588-2599 (1993).

[3] Šikalo, M. Marengo, C. Tropea, and E. N. Ganić, “Analysis of impact of droplets on horizontal surfaces,” Exp. Thermal Fluid Sci. 25, 503-510 (2002).

[4] I. V. Roisman, E. Berberović, and C. Tropea, “Inertia dominated drop collisions. I. On the universal flow in the lamella,” Phys. Fluids 21, 052103 (2009).

[5] J. Philippi, P. Y. Lagrée, and A. Antkowiak, “Drop impact on a solid surface: short time self-similarity,” J. Fluid Mech. 795, 96-135 (2015).

[6] A. Rozhkov, B. Prunet-Foch, and M. Vignes-Adler, “Impact of water drops on small targets,” Phys. Fluids 14, 3485-3501 (2002).

[7] A. Rozhkov, B. Prunet-Foch, and M. Vignes-Adler, “Impact of drops of polymer solutions on small targets,” Phys. Fluids 15, 2006-2019 (2003).

[8] E. Villermaux and B. Bossa, “Drop fragmentation on impact,” J. Fluid Mech. 668, 412-435 (2011).

[9] G. Juarez, T. Gastopoulos, Y. Zhang, M. L. Siegel, and P. E. Arratia, “Splash control of drop impacts with geometric targets,” Phys. Rev. E 85, 026319 (2012).

[10] L. S. Hung and S. C. Yao, “Experimental investigation of the impaction of water droplets on cylindrical objects,” Int. J. Multiph. Flow 25, 1545-1559 (1999).

[11] C. Chung, M. Lee, K. Char, K. H. Ahn, and S. J. Lee, “Droplet dynamics passing through obstructions in confined microchannel flow,” Microfluid. Nanofluid. 9, 1151-1163 (2010).

[12] D. Zhang, K. Papadikis, and S. Gu, “Investigations on the droplet impact onto a spherical surface with a high density ratio multi-relaxation time lattice-Boltzmann model,” Commun. Comput. Phys. 16, 892-912 (2014).

[13] Q. Li, Z. Chai, B. Shi, and H. Liang, “Deformation and breakup of a liquid droplet past a solid circular cylinder: A lattice Boltzmann study,” Phys. Rev. E 90, 043015 (2014).

[14] G. Liang, Y. Guo, Y. Yang, and S. Shen, “Liquid sheet behaviors during a drop impact on wetted cylindrical surfaces,” Int. Commun. Heat Mass Trans. 54, 67-74 (2014).

[15] Y. Hardalupas, A. Taylor, and J. H. Wilkins, “Experimental investigation of sub-millimetre droplet impingement on to spherical surfaces,” Int. J. Heat Fluid Flow 20, 477-485 (1999).

[16] S. Bakshi, I. V. Roisman, and C. Tropea, “Investigations on the impact of a drop onto a small spherical target,” Phys. Fluids 19, 032102 (2007).

[17] Y. Ge and L. S. Fan, “Droplet–particle collision mechanics with film-boiling evaporation. J. Fluid Mech. 573, 311-337 (2007).

[18] L. Yan-Peng and W. Huan-Ran, “Three-dimensional direct simulation of a droplet impacting onto a solid sphere with low-impact energy,” Can. J. Chem. Eng. 89, 83-91 (2011).

[19] S. Mitra, M. J. Sathe, E. Doroodchi, R. Utikar, M. K. Shah, V. Pareek, J. B. Joshi, and G. M. Evans, “Droplet impact dynamics on a spherical particle,” Chem. Eng. Sci. 100, 105-119 (2013).

[20] D. Zhang, K. Papadikis, and S. Gu, “Application of a high density ratio lattice-Boltzmann model for the droplet impingement on flat and spherical surfaces,” Int. J. Therm. Sci. 84, 75-85 (2014).

[21] J. M. Gac and L. Gradoń, “Lattice-Boltzmann modeling of collisions between droplets and particles,” Colloids Surfaces A 441, 831-836 (2014).

[22] V. V. Dubrovsky, A. M. Podvysotsky, and A. A. Shraiber, “Particle interaction in three-phase polydisperse flows,” Int. J. Multiphase Flow 18, 337-352 (1992).

[23] S. Mitra, M. J. Sathe, E. Dorrodchi, V. Pareek, J. B. Joshi, and G. Evans, “In-flight collision behaviour of droplets on a spherical particle falling under gravity,” NOVA. The University of Newcastle's Digital Repository (2013).

[24] V. Sechenyh and A. Amirfazli, “An experimental study for impact of a drop onto a particle in mid-air: The influence of particle wettability,” J. Fluids Struct. 66, 282-292 (2016).

[25] R. E. Pepper, L. Courbin, and H. A. Stone, “Splashing on elastic membranes: the importance of early-time dynamics,” Phys. Fluids 20, 082103 (2008).

[26] J. D. Bernardin, C. J. Stebbins, and I. Mudawar, “Effects of surface roughness on water droplet impact history and heat transfer regimes,” Int. J. Heat Mass Trans. 40, 73-88 (1996).

[27] R. Rioboo, M. Voué, A. Vaillant, and J. De Coninck, “Drop impact on porous superhydrophobic polymer surfaces,” Langmuir 24, 14074-14077 (2008).

[28] S. Mangili, C. Antonini, M. Marengo, and A. Amirfazli, “Understanding the drop impact phenomenon on soft pdms substrates,” Soft Matter 8, 10045-10054 (2012).

[29] Y. Mualem, S. Assouline, and H. Rohdenburg, “Rainfall induced soil seal (A) A critical review of observations and models,” Catena 17, 185-203 (1990).

[30] J. C. Bird, S. S. Tsai, and H. A. Stone, “Inclined to splash: triggering and inhibiting a splash with tangential velocity,” New J. Phys. 11, 063017 (2009).

[31] J. B. Lee and S. H. Lee, “Dynamic wetting and spreading characteristics of a liquid droplet impinging on hydrophobic textured surfaces,” Langmuir 27, 6565-6573 (2011).

[32] V. Bergeron, D. Bonn, J. Y. Martin, and L. Vovelle, “Controlling droplet deposition with polymer additives,” Nature 405, 772-775 (2000).

[33] G. B. Webber, R. Manica, S. A. Edwards, S. L. Carnie, G. W. Stevens, F. Grieser, R. R. Dagastine, and D. Y. Chan, “Dynamic forces between a moving particle and a deformable drop,” J. Phys. Chem. C 112, 567-574 (2008).

[34] S. Mitra, E. Doroodchi, V. Pareek, J. B. Joshi, and G. M. Evans, “Collision behaviour of a smaller particle into a larger stationary droplet,” Adv. Powder Technol. 26, 280-295 (2015).

[35] C. Josserand and S. T. Thoroddsen, “Drop impact on a solid surface,” Annu. Rev. Fluid Mech. 48, 365-391 (2016).

[36] C. S. Stevens, A. Latka, and S. R. Nagel, “Comparison of splashing in high-and low-viscosity liquids,” Phys. Rev. E 89, 063006 (2014).

[37] A. Rozhkov, B. Prunet–Foch, and M. Vignes–Adler, “Dynamics of a liquid lamella resulting from the impact of a water drop on a small target,” Proc. R. Soc. London A: Math. Phys. Eng. Sci. 460, 2681-2704 (2004).

[38] Z. Levin and P. V. Hobbs, “Splashing of water drops on solid and wetted surfaces: hydrodynamics and charge separation,” Philos Trans R Soc Lond A: Math. Phys. Eng. Sci. 269, 555-585 (1971).

[39] A. M. Podvysotsky and A. A. Shraiber, “Coalescence and break-up of drops in two-phase flows,” Int. J. Multiph. Flow 10, 195-209 (1984).

[40] A. L. Yarin, “Drop impact dynamics: splashing, spreading, receding, bouncing,” Annu. Rev. Fluid Mech. 38, 159-192 (2006).

[41] S. T. Thoroddsen and J. Sakakibara, “Evolution of the fingering pattern of an impacting drop,” Phys. Fluids 10, 1359-1374 (1998).

[42] S. D. Aziz and S. Chandra, “Impact, recoil and splashing of molten metal droplets,” Int. J. Heat Mass Trans. 43, 2841-2857 (2000).

[43] Y. E. Wang, J. H. Zhou, Y. L. Qin, P. L. Li, M. M. Yang, Q. Han, Y. B. Wang, and S. M. Wei, “Numerical simulation for behavior of a droplet impacting onto a target spherical surface,” Zhendong yu Chongji (J. Vib. Shock) 31, 51-56 (2012).

[44] G. Fang and A. Amirfazli, “Understanding the edge effect in wetting: a thermodynamic approach,” Langmuir 28, 9421-9430 (2012).

[45] M. Pasandideh-Fard, Y. M. Qiao, S. Chandra, and J. Mostaghimi, “Capillary effects during droplet impact on a solid surface,” Phys. Fluids 8, 650-659 (1996).

[46] S. Mitra, T. B. T. Nguyen, E. Doroodchi, V. Pareek, J. B. Joshi, and G. M. Evans, “On wetting characteristics of droplet on a spherical particle in film boiling regime,” Chem. Eng. Sci. 149, 181-203 (2016).

[47] S. Mitra, G. M. Evans, E. Doroodchi, V. Pareek, and J. B. Joshi, “Interactions in droplet and particle system of near unity size ratio,” Chem. Eng. Sci. (2017). https://doi.org/10.1016/j.ces.2017.03.059

Chapter 3

Effect of Viscosity, Gas Density, and Diameter Ratio on Impact Outcomes†

3.1 INTRODUCTION

Collision of droplets and moving solid particles in mid-air has a wide range of applications in chemical and petrochemical processes [1] (e.g. fluid catalytic cracking; FCC), pharmaceutical industries [2] (e.g. for coating tablets and granules of drugs), and particle coating [3] (e.g. for protection purposes against corrosion).

One of the most recent reviews on the general topic of drop impact on various solid surfaces is by Josserand and Thoroddsen [4]. They covered a wide range of theoretical and experimental works in the literature and discussed spreading, splashing, corona formation, and lifting of lamella from the surface. They mainly focused on explanation of the impact outcomes based on interplay of the various forces involved in the phenomenon. Formation of fingers and the effect of substrate properties such as roughness, wettability, and ambient air on impact products were also discussed. However, the focus of the present work is on droplet impact onto a spherical particle.

---

† This chapter has been submitted for publication as a journal paper: S. A. Banitabaei, A. Amirfazli," Droplet impact onto a solid sphere in mid-air: Effect of viscosity, gas density, and diameter ratio on impact outcomes", *Physics of Fluids.*

Yan-Peng and Huan-Ran [5] developed a numerical model for impingement of a droplet onto spherical targets. They studied impact behaviour and outcomes considering droplet size (D_d) of 5 mm, sphere sizes ranging from 1.26 to 50 cm, and impact velocities from 0.2 to 0.85 m/s. They found no significant difference in the time elapsed during the impact (i.e. from t=0 until the lamella is fully stretched) between droplet impact onto a particle and onto a flat surface. They also reported that the outcome of the impact process for particle diameter (D_p) of 1.26 was geometrically similar to that for D_p=50 (which represents a flat surface). However, their findings were mostly related to when the ratio of the droplet to particle size is less than one.

Gac and Gradon [6] performed a numerical study for head-on collision of a droplet and a spherical particle. Without mentioning the liquid type or its viscosity, they observed that when a droplet is larger than the particle, three collision scenarios were possible as Weber number increased from 0.6 to 70: (1) coalescence without disintegration, (2) ripping and coating with some small satellite droplets, and (3) shattering. During the last regime, a long conical film was created in form of a liquid skirt (i.e. lamella) which was eventually broken into many small droplets. A similar phenomenon was already reported by Dubrovsky *et al.*[7] and also later in [8] both for a similar range of Weber numbers (see Fig. 10 in [7] and Table 1 in [8]). They showed that the lamella length before the breakup and the time of breakup depend on the droplet to particle diameter ratio. Both studies found that when D_r was greater than one, a long lamella was generated during the impact (lamella formation was also reported in [9] for D_r =1.75 with *We*=1146, and for D_r =1.45 with *We*=2332 in [8]). Gac and Gradon also reported Weber number as the main parameter for impact characterisation. In their simulation work, they mentioned that D_r,

capillary number, and wettability of the particle influence the collision time rather than its outcome. Investigation of this claim requires studying impact cases in a wider range of D_r (majority of the literature studied the impact process for when D_r is ~1; see the illustrative map presented in Fig. 11 of [9]).

They used level-set method in formulation of Navier-Stokes equation and modelled moving contact lines using a static contact angle. Their results showed that regardless of the impact velocity and diameter of the target, the corresponding time for the primary spreading and recoiling process of a droplet on the surface remains almost unchanged. This is consistent with the results reported by Banitabaei and Amirfazli [4] for having a constant time scale when maximum lamella stretching happens for droplet impact onto a still particle ($t^*_{max} = 2.5$).

There are a few studies in the literature regarding droplet-particle collision in mid-air (see for instance Podvysotsky and Shraiber [10], Mitra *et al.* [11], and Dubrovsky *et al.*[7]. While the majority of studies in the literature is for $D_r < 1$, Sechenyh and Amirfazli [8] performed an experimental study for impact of a particle onto a falling droplet in mid-air with D_r>1. They investigated both hydrophilic and hydrophobic particles with D_r=1.45 (see Fig. 9 in [8]). For hydrophobic particles, they reported three different regimes depending on the relative velocity of the droplet and the particle (V_{rel}): bonding (V_{rel}<1.73 m/s), ripping and coating (V_{rel}~3.1 m/s), and shattering (3.9<V_{rel}<8.1 m/s). For the latter, they observed formation of a liquid skirt (i.e. lamella) during the impact and investigated the effect of impact velocity on lamella length, base diameter, and duration of lamella stretching phase. Later, Banitabaei and Amirfazli [9] performed an experimental and numerical investigation for head-on collision of a water droplet and a stationary spherical

target for D_r ~1.75. They found that in the case of impact on hydrophobic particles and a sufficiently large droplet velocity (We>162), a conical lamella is always formed. They explained the relationship between kinematic, geometrical, and physical characteristics of drop-particle system and properties of the impact outcome. However, both [8] and [9] only used water as liquid and within a narrow range of D_r for their experiments. Therefore, the effect of liquid viscosity and size ratio (specifically when D_r >1) on impact products were not covered and will be one of the main goals of the present work.

Another important aspect in studying droplet and particle impact is the effect of ambient gas on lamella formation for drop impact onto a flat surface. Xu *et al.* [12] identified the following two deciding factors to determine whether a drop impact leads to splashing or spreading: the drag force applied to the drop from the surrounding gas (F_d), which plays a destabilizing role by lifting and/or stretching the lamella, and the surface force (F_σ) which works in opposition by minimizing the surface area and preventing further stretching. Bird *et al.* [13] argued that for splashing to happen, the kinetic energy of the lamella should be high enough to lift the rim, and subsequently the entire liquid film, off the substrate. Moreover, they claimed that the trade-off between these two energy sources varies with density and pressure of the surrounding gas.

Riboux *et al.* [14] discussed cases where the lift force from the surrounding gas on the rim (i.e. edge of the lamella) is sufficiently large to prevent the rim from reattaching to the substrate. In this case, the lamella detaches from the surface and splashing would happen. They introduced a formula for determining the onset of splashing and similar to [12], this formula suggests that density and viscosity of the gas phase affect the splashing

onset. The effect of density and pressure of the ambient gas on spreading and lamella formation in droplet-particle impact has not been addressed in the literature yet.

In the present work, first, an experimental investigation was conducted on collision of a droplet onto a moving particle in mid-air (D_r~1.4 and We~1800). The droplet falls by gravity and the particle was shot upwards such that the angle between the two velocity vectors during the impact remained 180° (unlike some impact cases in the literature, see [7] and [8], for instance). This guarantees a completely head-on collision as the particle passes through the droplet. A numerical simulation model was then developed and verified against the available experiments. We have three main objectives in this chapter. As the first goal, the effect of liquid viscosity (μ) and droplet-to-particle diameter ratio (D_r) on both the impact products and the collision time was investigated. Using simulations, the general flow pattern inside the liquid film and the lamella rim was also examined to investigate the effect of viscosity on the flow field in the lamella (second goal). Moreover, the simulation was used to determine whether, and how, the physical properties of the ambient gas affect the lamella formation, which is our third goal in this chapter.

3.2 EXPERIMENTAL SETUP AND METHODS

3.2.1 TEST APPARATUS AND MATERIALS

Figure 3-1 shows the experimental setup used for studying droplet impact onto a particle in mid-air. A droplet with a diameter of $D_r \sim 2.9\ mm$ was generated through a syringe connected to a stepper motor which allowed generation of a single water droplet

gently (a few mm^3/sec) and precisely. The liquid volume and dispense rate were controlled through the computer. Vertical position of the syringe was adjustable to allow for varying the droplet velocity at the impact point. A spring-loaded particle launcher was used to shoot the particle upwards when the droplet passed the laser beam. Two perpendicular positioning stages were also used to let the operator adjust the particle location precisely beneath the needle. Two high speed cameras with a frame rate of 7000 *fps* captured images from two perpendicular views to verify whether a head-on impact had taken place; otherwise, the test was repeated with a new dry particle until a head-on impact occurred. Glass beads with a diameter of 2±0.01 *mm* were used as the particles. According to [9], a silanization procedure with OctaDecylTrichloroSilan (ODTS) was performed on the beads to create a contact angle of 118±2° on their surface. Droplet size, velocities, and the lamella geometrical parameters were determined by manual image processing using ImageJ software. For the experiments, a standard calibration grid with a mesh size of 0.25 *mm* was used to determine the pixel size in each frame. However, for the simulation results, the particle diameter was taken as the reference length for pixel size calibration to be used for measuring the lamella geometrical parameters. Specifications and adjustments of the cameras, the illumination system, image size and calibration were all similar to [9] and details were given therein.

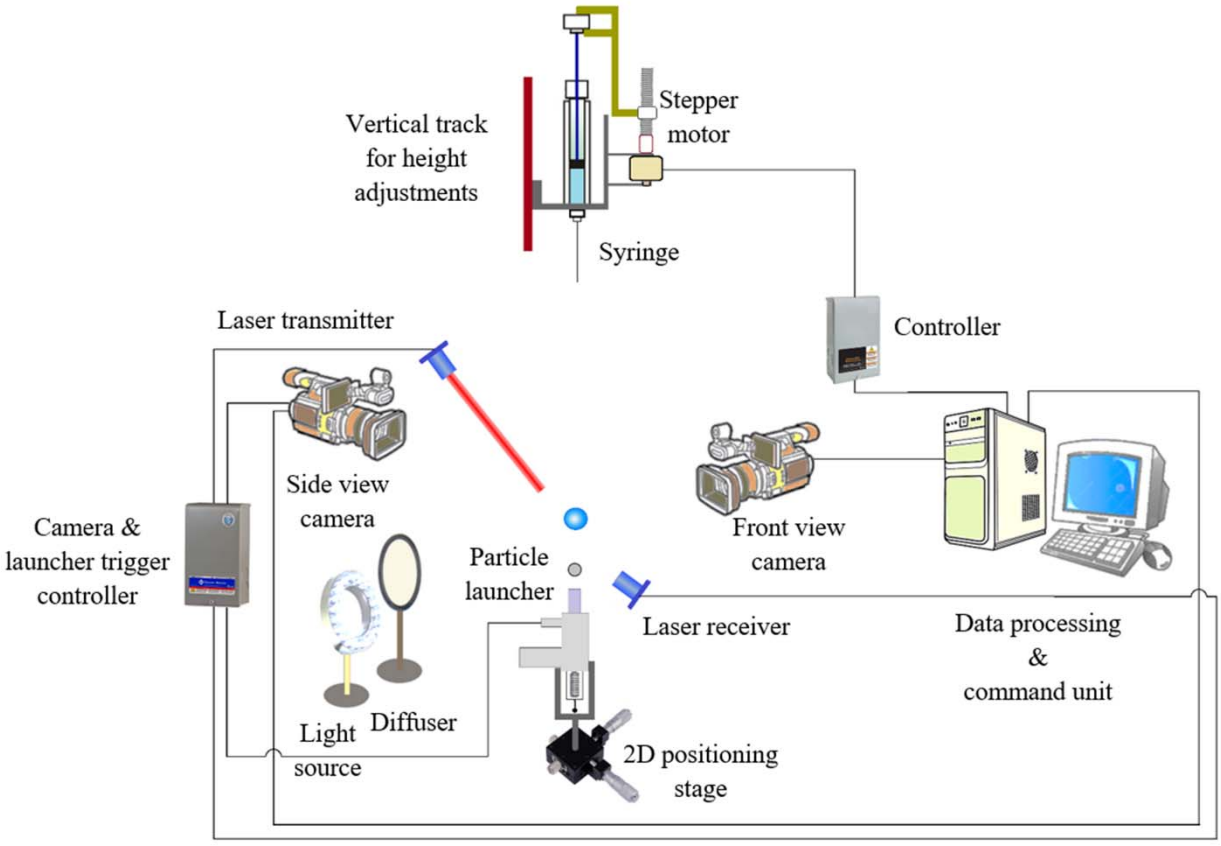

Figure 3-1 *Schematic of the experimental setup used for impact of a droplet onto a particle in mid-air.*

For the liquid used to generate the droplets, silicone oils with a wide range of viscosities were used in the simulations. See Table 3-1 for the physical properties of silicone oils used.

Table 3-1 *Physical properties of silicone oil droplets at* 20℃ [15]

No.	Viscosity (μ) cP	Surface tension (σ) mN/m	Specific gravity
1	1	17.4	0.851
2	2	18.7	0.873
3	5	19.7	0.918
4	20	20.6	0.950
5	50	20.8	0.960
6	100	20.9	0.966
7	200	21.0	0.968
8	350	21.1	0.970

3.2.2 NUMERICAL SIMULATION

For implementing the numerical simulation, CLSVOF method was used in ANSYS-Fluent 18.2. A 2D axisymmetric model was created with a User Defined Function (UDF) for the particle characteristics in Dynamic Mesh mode. 2D axisymmetric simulation is valid for studying lamella formation and has been widely used for liquid film behaviour in symmetrical impacts (see for instance [16]). However, it is worth mentioning that due to the 360° revolution of the axisymmetric results, the satellite droplets formed in a 2D model due to splashing are not meaningful. Some more important points regarding the numerical simulation are mentioned below and more details could be found in [9]. Since the domain is defined as axisymmetric, the mass and momentum conservation equations are solved in cylindrical coordinate system by Fluent. However, they are shown below in Cartesian system for the sake of clarity and compatibility with the literature:

$$\frac{\partial \rho}{\partial t} + \nabla \times (\rho \vec{v}) = 0 \quad (1)$$

$$\frac{\partial (\rho \vec{v})}{\partial t} + \nabla \times (\rho \vec{v} \vec{v}) = -\nabla \mathrm{P} + \nabla \times [\mu \nabla \vec{v} + (\nabla \vec{v})^T] + \rho \vec{g} + \vec{F_s} \quad (2)$$

in which $\rho, v, P, \text{and } F_s$ are density, velocity, pressure, and surface tension force, respectively. For calculating volume fraction of each phase (α), the advection equation is defined as (subscripts *l*, *g*, and *mix* denote the liquid, gas, and mixture, respectively):

$$\frac{\partial \rho_l \alpha_l}{\partial t} + \vec{v} \times \nabla \rho_l \alpha_l = 0 \quad (3)$$

$$\sum_{i=1}^{n} \alpha_i = 1 \quad (4)$$

The same momentum equation is solved for both gas and liquid phases. Properties of the fluid are calculated according to α value for the cell which is always between 0 and 1 (α_l=0 for gas and α_l=1 for the liquid):

$$\rho_{mix} = \alpha_l \rho_l + (1 - \alpha_l) \rho_g \quad (5)$$

$$\mu_{mix} = \alpha_l \mu_l + (1 - \alpha_l) \mu_g \quad (6)$$

Surface tension term ($\vec{F_s}$) in Eq. (2) is calculated by:

$$\vec{F_s} = \sigma \frac{\rho k \nabla \alpha}{\frac{1}{2}(\rho_l + \rho_g)} \quad (7)$$

where k is curvature of the free surface calculated by divergence of unit surface normal ($\hat{n}$). If θ is the angle between the interface and the wall, one can write:

$$\hat{n} = \hat{n}_w cos\theta + \hat{n}_t sin\theta \quad (8)$$

in which $\hat{n}$ is the normal vector of the interface and $\hat{n}_w$ and $\hat{n}_t$ are its unit vectors perpendicular and tangent to the wall, respectively.

In numerical simulations, it is often more convenient to consider a constant value for the droplet contact angle on the substrate surface. However, in droplet impact studies, the triple point line on the solid surface is not stationary. As a result, contact angle of the liquid on the particle surface varies with the velocity of the contact line. For impact of a falling droplet onto a moving particle in this study, the dynamic contact angle (DCA) was implemented to consider the effect of variations of the contact line velocity on contact angle. A second UDF was used to implement variations of the contact angle. Implementation of DCA had to be different to some extent from the literature since in addition to the liquid front, the solid particle also has a velocity that changes in time (see the Supplementary Information for more details and a comparison between solutions with and without DCA).

Mesh dependency of the simulation was tested and a variable time step (TS) was implemented in the simulations. TS was determined such that the value of Courant number always remained less than 0.2 (see [16] for more details). Number of iterations in each TS was fixed to 80 to assure that the normalized residual for continuity and velocities would be less than 10^{-6}. Results of the numerical simulation were compared to those of two sets of experiments: one performed using the experimental setup explained in Section 3.2.1, and the other with different liquid viscosity, particle, and droplet sizes taken from [17] (see Section 3.1).

3.3 RESULTS AND DISCUSSIONS

In the next sections, the developed numerical model is validated with the results of experiments for different conditions. Then, using the numerical simulation, dynamics

of the flow inside the liquid film was studied and used to explain the behaviour of the lamella upon impact. Moreover, the effect of droplet-to-particle diameter ratio on impact outcomes was investigated. A comprehensive study was also presented on the effect of liquid viscosity on lamella formation through the velocity field of flow inside the liquid film. Moreover, the effect of lift force applied by the ambient air on lamella formation is presented.

3.3.1 VERIFICATION OF THE NUMERICAL MODEL

Geometrical parameters of the lamella (e.g. lamella length, cone angle, and the base diameter) for the numerical simulation was measured and shown to be in a good agreement with two sets of different experimental results shown in Fig. 3-2. The maximum discrepancy in geometrical parameters measured between the numerical and experimental results for lamella length, cone angle, and the base diameter was 15%, 6%, and 8%, respectively (the measurement method was explained in Section 3.2.1). Volume of the liquid before and after impact was also calculated in ANSYS-Fluent and the maximum discrepancy of 0.013% indicates a very good mass conservation for the numerical solution. Therefore, the simulation tool was used in the next sections for parametric studies of the droplet-particle impact. Note that $D, v, \mu,$ and σ denote the diameter, velocity, viscosity, and surface tension, respectively. Subscripts *d* and *p* also refer to the droplet and particle, respectively. It is worth mentioning that right after the droplet impacts onto the particle, formation of an air cushion was observed on the north pole of the particle (and causes the grid in that area to be refined as well). However, this phenomenon has been well investigated in the literature of droplet impact (on both flat

surface and curved surfaces) and is not emphasized in the current study. For more studies on air cushion formation and wettability effect on it, please refer to Ref. [4] where several works have been introduced.

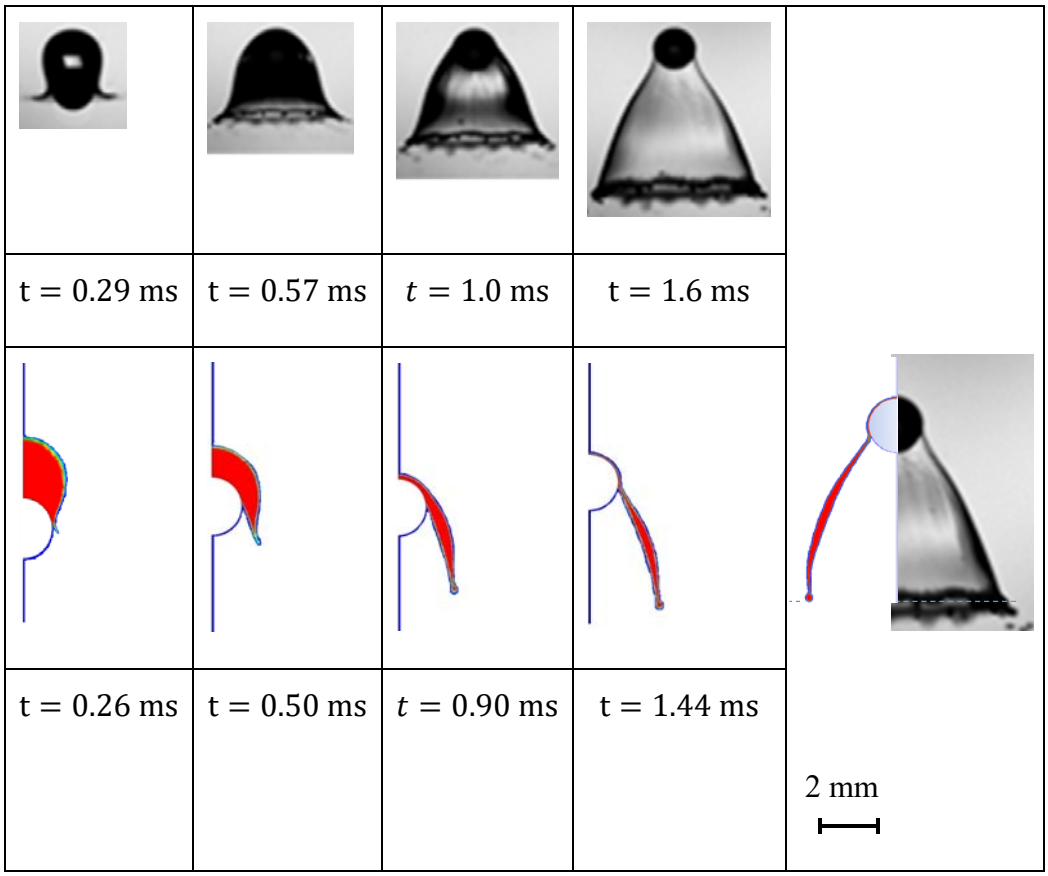

$D_d = 2.9\ mm, D_p = 2.0\ mm, v_d = 0.68\frac{m}{s}, v_p = 6.83\frac{m}{s}, \mu = 1\ cP, \sigma = 72\ mN/m$

(a)

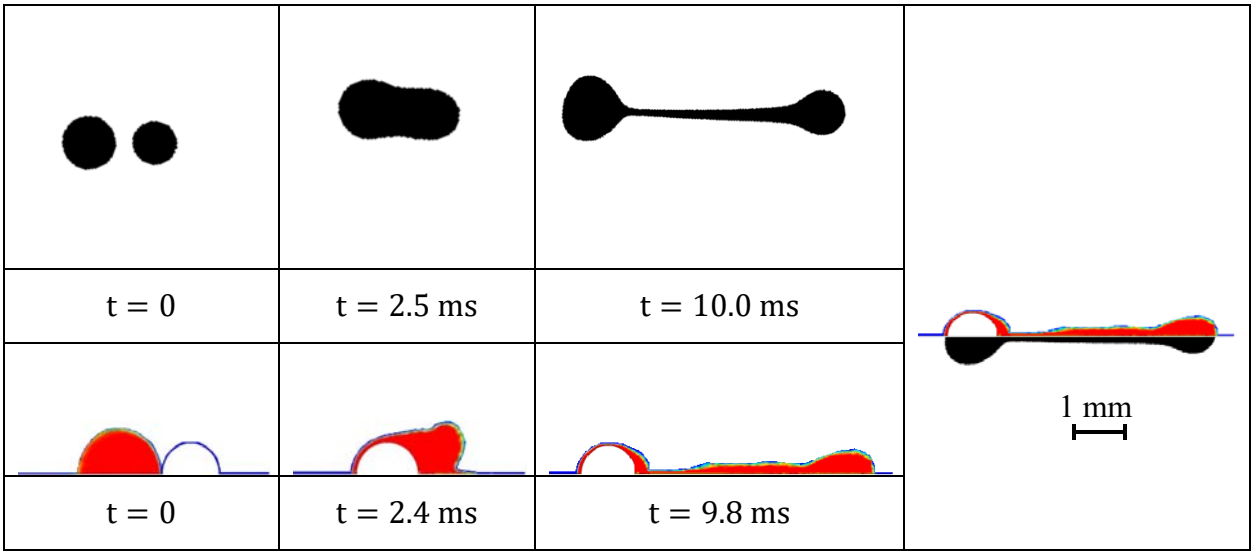

$$D_d = 1.5\ mm, D_p = 1.0\ mm, v_d = 0.75\frac{m}{s}, v_p = 2.22\frac{m}{s}, \mu = 6\ cP, \sigma = 14\ mN/m$$

(b)

Figure 3-2 *Comparison of experimental and numerical results of droplet-particle for two different cases: a) low-viscosity high surface tension liquid, b) low surface tension and a higher viscosity liquid (droplet: Silicon base-Duratherm S, Particle: glass bead; reproduced from Ref. [17] with permission).*

3.3.2 VELOCITY PROFILE INSIDE THE LAMELLA

During the collision, the particle starts penetrating into the droplet and accelerating the liquid around the particle surface. Figure 3-3 shows a 90° CCW rotated view of the impact. It is shown that the rim position remains almost unchanged, and during the lamella formation, the film is stretched along the same direction that particle moves (to the left in Fig. 3-3). A dimensionless time scale (t^*) was introduced to allow for comparison as: $t^* = \frac{4\mu t}{\rho D_d^2}$ where μ and ρ are viscosity and density of the liquid, respectively.

Interestingly, results of the simulation indicate that velocity vector of the flow becomes zero around the mid-lamella section. In other words, the flow inside the liquid film is in two opposite directions (see the area marked by the rectangle in panel (a-3) of Fig. 3-4. This is why the flow velocity inside the film is considerably smaller than the particle velocity (i.e. energy dissipation due to change in the flow direction).

As shown in Fig. 3-3, the radial distance of the liquid film (from the symmetry axis) is larger at the base-side ($r_2 > r_1$). This means that for the same Δx (an element of the lamella shown in the last row of Fig. 3-3), more liquid is necessary to form the lamella as *r* increases. A thick rim is also seen at the far right of the base which its growth requires liquid transfer (rim formation will be explained later). The required liquid for formation of the base-side of the lamella (i.e. vicinity of r_2) and the rim is from the flow reversal within the lamella. As shown in panel (a-1) of Fig. 3-4, right at the impact moment, a flow is initiated in the contact area which is opposite to the initial rightward flow inside the droplet. As the impact proceeds, the liquid film (lamella) is formed through these two opposite flows; the initial velocity of the droplet pushes the liquid around the particle and creates a flow towards the lamella base and forms the rim. On the other hand, particle momentum is transferred to the liquid as it keeps penetrating into the droplet. This intensifies the reverse flow and stretches the liquid towards the left (see the flow velocity shown in Figs. 3-4(a)-2 and 3). Reversal flows have been reported in other droplet impact cases too (see for instance, Fig. 9-C in [18] for droplet impact onto a flat surface with inhomogeneous wettability). It is worth mentioning that the radial component of the velocity inside the liquid film during the lamella stretching is towards the positive *r* direction which is why the lamella expands radially (see Fig. 3-3).

As the second objective of the chapter, the reason for rim formation can be inferred from the simulation results. At the tip of the lamella, while the change in pressure is accommodated by the interface curvature, the flow velocity inside the liquid film is decreased (compare regions A and B in Fig. 3-4(b)). Therefore, the surface energy overcomes the kinetic energy of the flow in that region trying to reduce the surface area. The minimum area would be achieved by formation of a toroidal shape which creates a circular cross section at the edge of the lamella.

(μs)	$t^* = \frac{4\mu t}{\rho D_d^2}$ ($\times 10^6$)	
312	156	
507	253	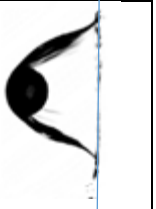
852	425	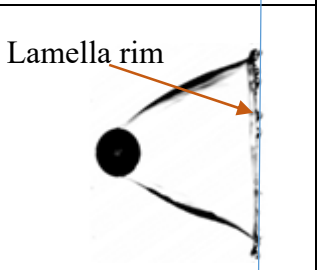
1011	504	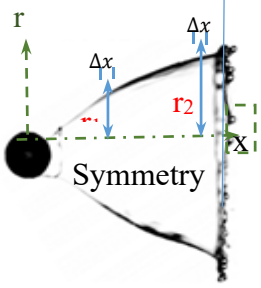

Figure 3-3 *During the lamella formation, the rim position remains almost the same while the base diameter is increased (water droplet, D_d=2.84 mm, V_d=0.68 m/s, D_p=2.0 mm, V_p=6.83 m/s).*

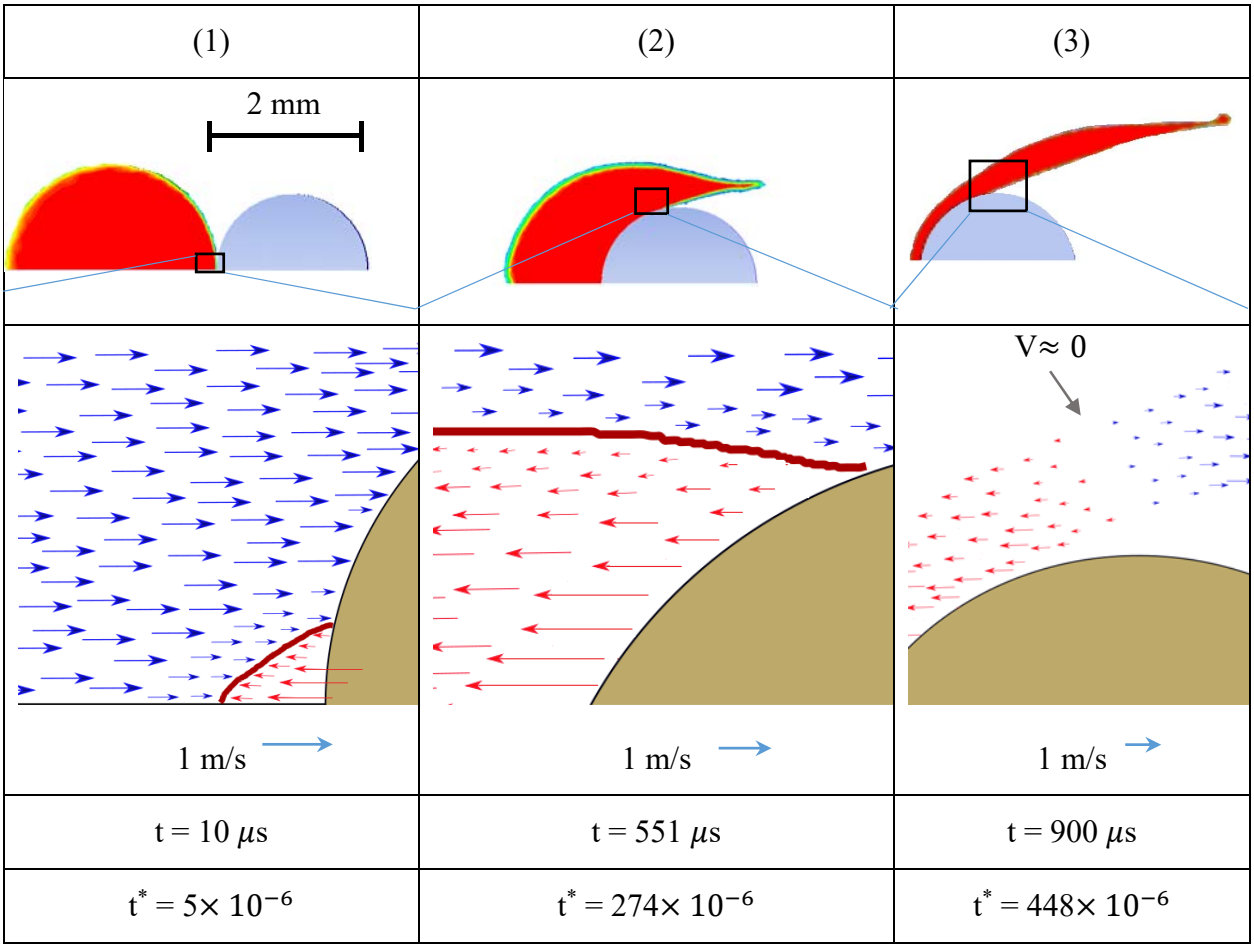

(a)

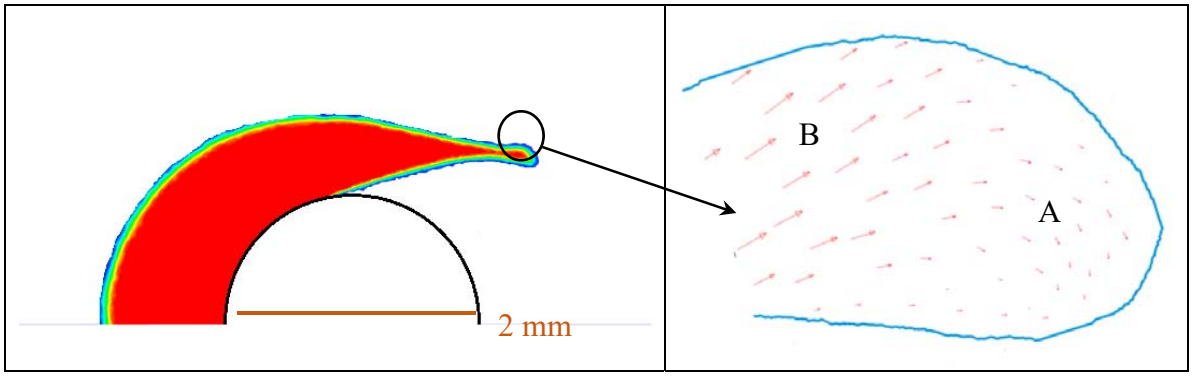

(b)

Figure 3-4 *a) Axial component of flow velocity inside the liquid film; a flow reversal is seen inside the lamella (solid lines are hand-drawn to aid with graphical clarity), b) velocity magnitude is reduced around the tip of the lamella causing rim formation (water droplet, D_d=2.84 mm, V_d=0.68 m/s, D_p=2.0 mm, V_p=6.83 m/s).*

3.3.3 EFFECT OF DROPLET-TO-PARTICLE DIAMETER RATIO

As shown in [9] and explained in Section 1, majority of studies in the literature worked on cases with D_r values close to one. Therefore, behavior of the impact outcomes for larger values of D_r is not clear and was defined as part of our first objective in this chapter. Simulations were performed to investigate the effect of droplet-to-particle diameter ratio for D_r >1 while the following parameters were kept constant: particle size D_p=2.0 mm, particle velocity V_p= 6.83 m/s, and droplet velocity V_d=0.68 m/s. Diameter of the water droplets was set as D_d=3.0 mm, 6.0 mm, and 10.0 mm to create diameter ratios of D_r=1.5, 3, and 5, respectively.

As shown in Fig. 3-5, for all impact cases a lamella was formed; i.e. the particle had enough initial momentum to penetrate into the droplet completely. Since the liquid mass should always be conserved, as droplet diameter was increased, the lamella length and thickness were also increased accordingly. Sechenyh and Amirfazli [8] had also experimentally shown that lamella length before the breakup, and the breakup timing, depend on D_r. However, as shown in Fig. 3-5, the cone angle for when the lamella was evolved did not change by much ($2\varphi \approx 36° \pm 3\%$). This is consistent with what Yan-Peng and Huan-Ran [5] reported that the impact outcome for D_p=1.26 was geometrically similar to that for D_p=50. The data presented in Fig. 3-5 is then in agreement with Gac and Gradon's [6] claim that droplet-to-particle diameter ratio influences mostly the collision time, rather than its scenario. Velocity vectors of the flow inside the larger lamella shown in Fig. 3-5 also indicates coexistence of two flow reversals as explained previously for $D_r \approx 1.5$.

A	B	C
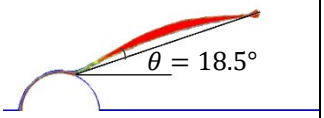	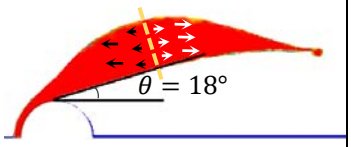	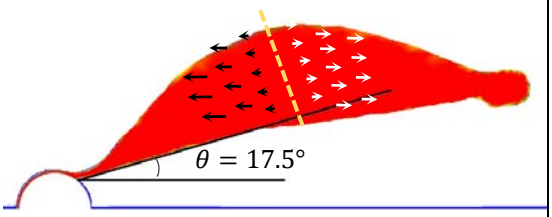
$D_r = 1.5$	$D_r = 3.0$	$D_r = 5.0$
t = 1443 μs	t = 2237 μs	t = 4548 μs
$t^* = 643\times 10^{-6}$	$t^* = 249\times 10^{-6}$	$t^* = 182\times 10^{-6}$
Oh = 1.91	*Oh* = 1.35	*Oh* = 1.05

Figure 3-5 *Effect of droplet to particle diameter ratio (D_r) on geometry of the impact outcomes, lamella cone angle, and the impact time (water droplets, D_p=2.0 mm, V_p=6.83 m/s, V_d=0.68 m/s).*

Moreover, since the inertia, surface tension, and viscous forces are all important in the outcome of the impact, one may use the Ohnesorge number as a non-dimensional indication of the ratio of these forces. Ohnesorge number is defined as:

$$\boldsymbol{Oh = \frac{viscous\ forces}{\sqrt{inertia \times surface\ tension}} = \frac{\sqrt{We}}{Re} = \frac{\mu}{\sqrt{\rho_r \sigma D_d}}}$$

in which $\boldsymbol{\mu}$ and $\boldsymbol{\sigma}$ and $\boldsymbol{D_d}$ are the dynamic viscosity, surface tension, and diameter of the water droplet, and $\boldsymbol{\rho_r}$ is the relative density of air to water. For the typical droplet diameter used in this study (i.e. D_d=2.84 mm), Ohnesorge number is calculated to be *Oh*=1.97 which, considering its order of magnitude, explains that viscous forces are equally important with inertia and surface tension. As seen in Fig. 3-5, when we increase the droplet diameter, *Oh* value will be reduced accordingly from 1.91 to 1.05 (it is still around one and conveying the same meaning for the forces balance as mentioned above).

3.3.4 EFFECT OF LIQUID VISCOSITY

As a part of the first objective of this study, we investigated the effect of liquid viscosity on impact outcomes. The particle and droplet diameters were kept constant in all simulations (i.e. D_p=2.0 *mm* and D_d=2.84 *mm,* respectively). Note that the values of D_p and D_d were selected such that D_r ~1.5 (according to discussions in Section 3.2 and Fig. 3-5, D_r needs to be larger than 1 for a lamella to be formed, and smaller than 2 for a thin liquid film to be generated). Velocity of the particle and droplet were also set to V_p=6.85 *m/s* and V_d=0.68 *m/s,* respectively. Viscosity of the liquids covered a wide range from 1 to 350 *cP* (see Table 1). Note that the simulation results for $\mu = 2$ and $\mu = 5\ cP$ are not shown as they did not generate significantly different results compared to what is shown in Fig. 3-6. As such, formation of lamella in case of drop impact onto particles and subsequent splashing is markedly different than splashing on flat surfaces. This is so, as in a recent work by Almohammadi and Amirfazli [19], it was shown that for flat surfaces splashing threshold behaves non-monotically with a change in viscosity, and viscosity of 5 cP is a turning point in dependency of splash threshold trend on viscosity.

As discussed in the literature, for a lamella to be formed, the particle must be hydrophobic (see Fig. 6 in [9]), and the liquid film should also have enough momentum to separate from the particle surface after impact. Figure 3-6 demonstrates the effect of liquid viscosity on lamella geometry and impact outcomes. As viscosity is increased, a larger portion of the pre-impact kinetic energy will be dissipated inside the film. Therefore, as shown for $\mu = 350\ cP$, the remaining kinetic energy is not enough to move liquid layers

on top of each other and create a thin enough film. So, the lamella is not formed and in case of higher viscosities, the particle may even get trapped inside the droplet.

Using the simulation results, a clear illustration of what happens inside the liquid film by increasing the viscosity is schematically demonstrated in Fig. 3-7. Velocity of the flow inside the film is also shown on each frame; the average velocity inside the liquid film for $\mu = 100\ cP$ is less compared to $\mu = 1\ cP$ due to higher energy dissipation (0.8 m/s compared to 3.3 m/s in panel (i); the blue line in the middle of lamella indicates the area around which the axial velocity is nearly zero). Therefore, for higher viscosities, the film thickness is higher, and consequently, a shorter lamella is generated. Furthermore, the remaining portion of the liquid on the particle is thicker for a liquid of higher viscosity. These are in agreement with the findings reported in [20] and [21] for droplet impact onto a still sphere and onto a cylinder, respectively, in which the film thickness on the substrate was increased with viscosity. Profile of the flow velocity inside the liquid film (shown with a circle in panels (iii) and (iv) in Fig. 3-7) confirms that at higher viscosities, average flow velocity inside the film $(\bar{V})$ is relatively smaller while $\mu\frac{\partial V}{\partial y}$ is larger. Therefore, free movement of the flow is hindered and a thicker layer is formed over the particle surface.

Figure 3-6 shows that as viscosity is increased, a larger rim is created at the tip of the lamella. This behaviour could be justified by the interplay between the kinetic and the surface energies around the rim area. The average flow velocity inside the film at the tip-side of the lamella for $\mu = 1$ and $\mu = 200\ cP$ is shown in panel (iii) of Fig. 3-7 (1.8 and 0.3 m/s, respectively). In lower viscosities, since the flow velocity inside the lamella is relatively high, the kinetic energy is dominant to all resistance sources (e.g. the viscous

dissipation and the energy associated with the increase in surface area) to fully stretch the lamella. However, as viscosity is increased, velocity inside the liquid film is accordingly decreased and so the surface energy starts to gain importance. Therefore, a larger rim is created at the tip-side to minimize the surface energy (i.e. less stretching of the surface area). This can also be interpreted by the energy balance below:

$$KE_p \cong KE_l + SE - VD \tag{9}$$

in which KE_p is the kinetic energy of the particle before impact, KE_l represents the kinetic energy of the liquid inside the film, SE is the surface energy, and VD denotes the viscous dissipation (surface energy of the droplet before impact has been neglected). When μ is increased, the flow velocity inside the lamella is decreased. Therefore, since the liquid film does not have as much kinetic energy (KE_l) for stretching the lamella, surface area and so *SE* would accordingly decrease. Therefore, based on Eq. (9), for KE_p to remain constant, the value of *VD* needs to be reduced as well ($VD \approx \mu(\bar{V}/h)^2$). Therefore, $\bar{V}$ needs to be decreased and lamella thickness (*h*) should be increased, both of which explain the results of numerical simulation shown in Fig. 3-6 from the first principles perspective. It is also worth mentioning that as shown in panel iv of Fig. 3-7, the velocity gradient grows as viscosity increases which indicates a higher value for the shear stress.

Droplet viscosity μ (cP)	Fully formed lamella	$t\ (\mu s)$	$t^* = \frac{4\mu t}{\rho D_d^2}$ ($\times 10^6$)
1	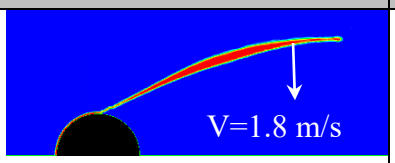	1,443	718
20	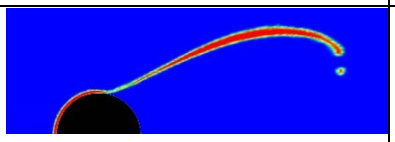	790	8,248
50	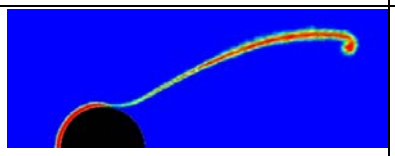	1,504	38,850
100	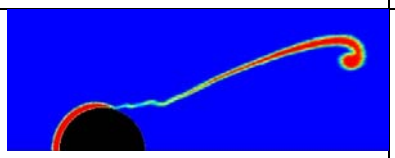	1,625	83,426
200	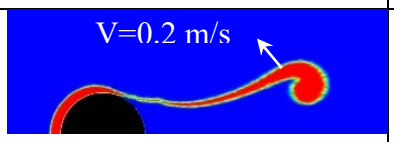	2,929	300,122
350		---	---

Figure 3-6 *Effect of liquid viscosity on lamella geometry in droplet impact onto a solid particle (silicone oil, D_d=2.84 mm, D_p=2.0 mm, V_p=6.83 m/s, V_d=0.68 m/s, σ ~ 20 mN/m)*

	(i)	(ii)	(iii)	(iv)
$\mu = 1\ cP$	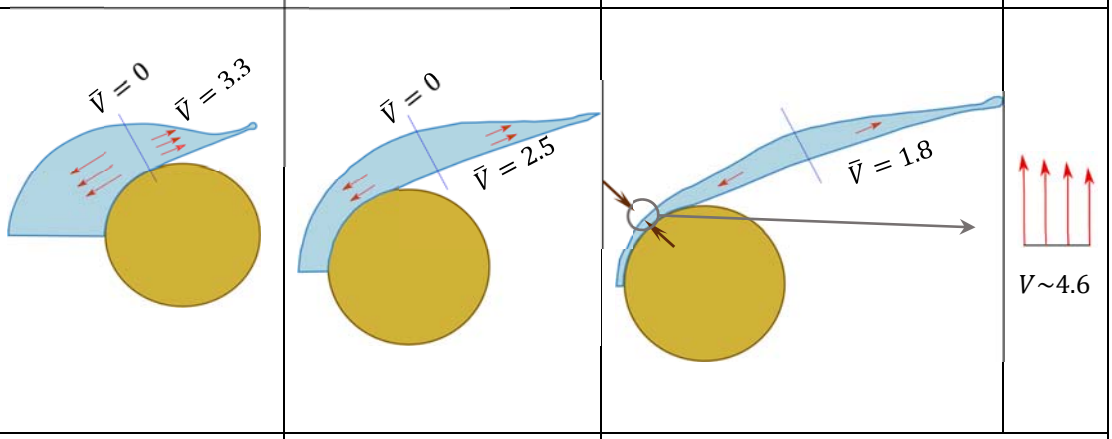			
t (μs)	253	457	672	
t^* $\times 10^{-6}$	126	228	335	
$\mu = 100\ cP$	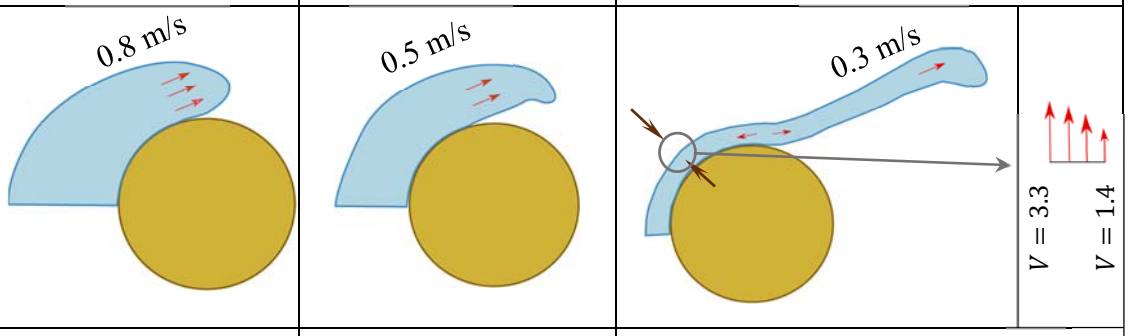			
t (μs)	241	409	1037	
t^* $\times 10^{-6}$	120	204	517	

Figure 3-7 *Schematic of the fluid flow inside the liquid film, lamella formation, and the remaining film thickness. Direction and magnitude of the velocity vectors were extracted from the simulation results; but arrows are not to the same scale (silicone oil, D_d=2.84 mm, D_p=2.0 mm, V_p=6.83 m/s, V_d=0.68 m/s, σ ~ 20 mN/m).*

It is also inferred that t^* by which a lamella is fully formed is not the same for all viscosities. This observation is similar to what was reported by Zhang *et al.* [21] for 2D Lattice-Boltzmann simulation of droplet impact onto a curved target. When they changed

Reynolds number by varying kinematic viscosity of the liquid, the non-dimensional time and film thickness curves did not collapse on a single curve in the inertia dominated phase. This may, in relation to our second objective, indicate that the lamella being completely stretched in various systems cannot be considered as a criterion to evaluate dynamics of the systems, although they look apparently similar.

3.3.5 EFFECT OF THE AMBIENT GAS

As mentioned in Section 1, the literature explains the effect of force by the ambient air on splashing for drop impact onto flat surfaces. However, an investigation is required to understand whether and how forces from the surrounding gas affect formation of the lamella for impact of a droplet and particle. Splashing in the traditional sense, usually refers to the liquid breakup due to the drop impact; however, here a prerequisite of splashing is the stretching of lamella which eventually ends in its breakup (splashing).

At the initial stage of lamella formation, shear stress is transferred by the drag force to change the shape of the leading edge of the liquid film on the particle surface. For hydrophobic particles, the thin edge of the lamella is separated from the surface (see Figs. 3 to 5 in [9]) and is driven by the interplay of the inertia force of the liquid flow inside the film, and the downward drag force due to the pressure difference between two sides of the lamella edge (see panel (b) in Fig. 3-8).

Therefore, a set of simulations was made in which density of the surrounding gas (which can also be a proxy for the gas pressure) was changed. The idea was to investigate how the lift force applied by the gas phase would impact the collision outcome. The lift force is defined as: $F_L = \frac{1}{2} C_L \rho A V^2$ in which C_L is the lift coefficient, ρ is the gas

density, A is cross sectional area of the object, and V is the relative velocity of the fluid and object. As Fig. 3-8 illustrates, by changing the ambient gas density from $\rho_{amb} = 0.2\rho_{atm}$ to $\rho_{amb} = 2\rho_{atm}$, no significant change in the lamella geometry was observed ($\rho_{atm} = 1\ bar$, and maximum discrepancy for lamella length, cone angle, and film thickness was less than 2.5% between two cases).

However, the simulation results indicate that further increasing the ambient gas density (i.e. from $2\rho_{atm}$ to $5\rho_{atm}$), increased the downward lift force applied on the lamella. This is inferred by comparing the pressure difference between the inner and outer parts of the liquid film (i.e. zones *A* and *B* shown in panels (*c*) and (*d*) in Fig. 3-8). The pressure difference (ΔP), which represents the magnitude of the lift force applied on the lamella, increases from 0.45 kPa in panel (c) to 3.2 kPa in panel (*d*) and bends the liquid film downwards. It is worth mentioning that a different behavior was reported for the effect of ambient gas pressure for drop splashing on a flat surface (i.e. $D_r \to 0$). Experimental studies of Xu *et al.* [12] showed that for impact of a droplet onto a flat dry surface, splashing will be suppressed if the pressure of the ambient gas is reduced from the atmospheric pressure (see Fig. 1 in [12]). They argued about two factors being operative: 1) restraining pressure of the gas on the liquid which has a destabilizing role and deflects the advancing front upwards, and 2) surface tension which works to keep the liquid together. They found that at the splashing threshold, two stresses created by these two factors are comparable (i.e. have the same order of magnitude), while decreasing the ambient pressure makes the surface tension force to be dominant, and the splashing to be suppressed. The ambient pressure in [12] was always below the atmospheric pressure, while in the present study, we investigated pressures up to 10 times the

atmospheric one; so the results are not similar. Also in [12], the major cause for lifting the liquid film off the surface is the shear stress from the ambient air. However, in the current study, the convex curvature of the surface together with its wettability also play an important role. Our simulation results indicate that when the ambient air density/pressure is further increased (e.g. $\rho_{amb} > 5\rho_{atm}$), the pressure difference between zones *A* and *B* in panel (e) is increased to 7.4 kPa which hinders the film stretching; as such a thicker lamella is formed and it is bent downwards. Note that the pressure difference is originated from the difference in density of the air molecules in two zones. Therefore, when the density of the ambient air is increased in the zones, the pressure difference is accordingly increased as well.

	Ambient gas density (kg/m^3)		Time (μs)
(a)	$0.2\rho_{atm} = 0.25$	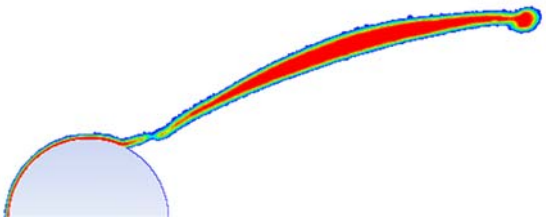	t=1450
(b)	$\rho_{atm} = 1.225$	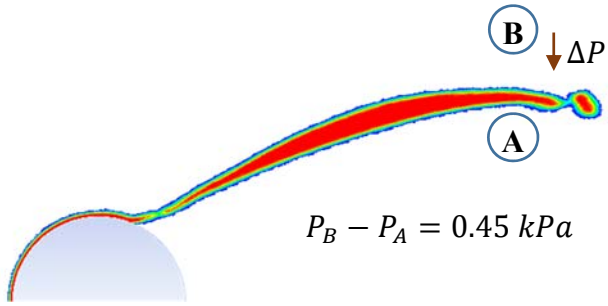	t=1450
(c)	$2\rho_{atm} = 2.45$	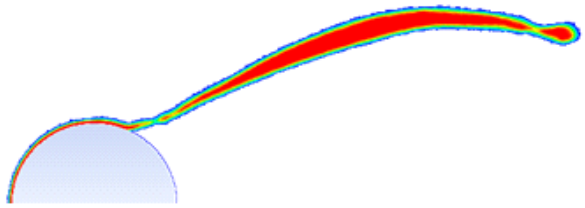	t=1450
(d)	$5\rho_{atm} = 6.125$	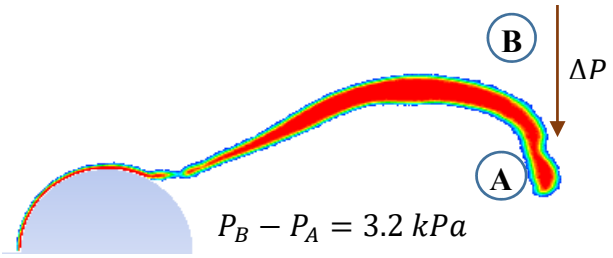	t=1450
(e)	$10\rho_{atm} = 12.25$	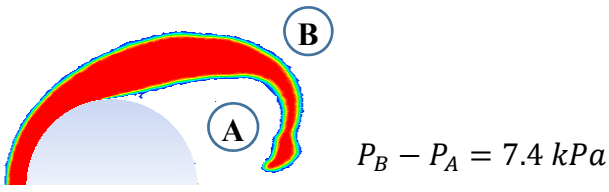	t=650

Figure 3-8 *Effect of drag force on lamella formation;* $\mu_l = 10\ cP$, $\sigma = 21\ m\,N/m$, D_p*=2.0 mm,* D_d*=2.84 mm.*

3.4 CONCLUSION

Impact of a droplet onto a spherical particle in mid-air resulted in formation of a liquid film. This lamella was studied using a validated numerical simulation model. Investigations were mainly to determine how various conditions affect the impact outcomes and change the lamella formation process. The concluding remarks are as follows:

1) The lamella is formed due to coexistence of two opposite flows within the liquid film; one is generated through the momentum transfer from the particle, and the other is created by the initial velocity of the droplet which is towards the lamella base. Moreover, since the flow velocity inside the liquid film is relatively lower around the lamella base, surface energy becomes the dominant player in that area and therefore, a rim is also formed to minimize the local surface energy.
2) A larger droplet-to-particle diameter ratio increases the impact duration (i.e. time elapsed from the impact moment until the expected product is formed) but does not change the impact scenario and the collision outcomes (when $1.5<D_r<5$). In this case, existence of two opposite flows still takes place inside a thicker liquid film and causes a shorter lamella to be formed.
3) A higher liquid viscosity makes the lamella shorter but increases its rim size. Simulation results indicate that when μ is reduced ($1<\mu<350$ cP), the average flow velocity inside the film is accordingly reduced which causes both the lamella thickness and the remaining film thickness on the particle to be increased.
4) The simulation results indicate that when the ambient air pressure (or density) is increased from the atmospheric value (e.g. gas density from $2\rho_{atm}$ up to $10\rho_{atm}$), the

lamella formation will be suppressed. The reason is that by increasing the ambient density/pressure, the pressure gradient between inner and outer parts of the lamella increases from 0.45 kPa to 7.4 kPa which applies a larger downward drag on the liquid film, prevents the film stretching, and bends the lamella. This is unlike the case in [12] for droplet impact on a flat surface in which $P_{amb} \leq P_{atm}$ and the lamella was further splashed as the ambient pressure was increased.

3.5 SUPPLEMENTARY INFORMATION

As mentioned in Section 2.2, a User Defined Function was integrated into the simulation to calculate DCA. The UDF sweeps the particle surface in each time step to locate the triple point (TP) coordinates. Therefore, changes in the TP location between two selected time steps (e.g. from t_i to t_{i+1}) was calculated to determine TP velocity and the *Capillary* number (see Eq. 11 and Fig. 3-9).

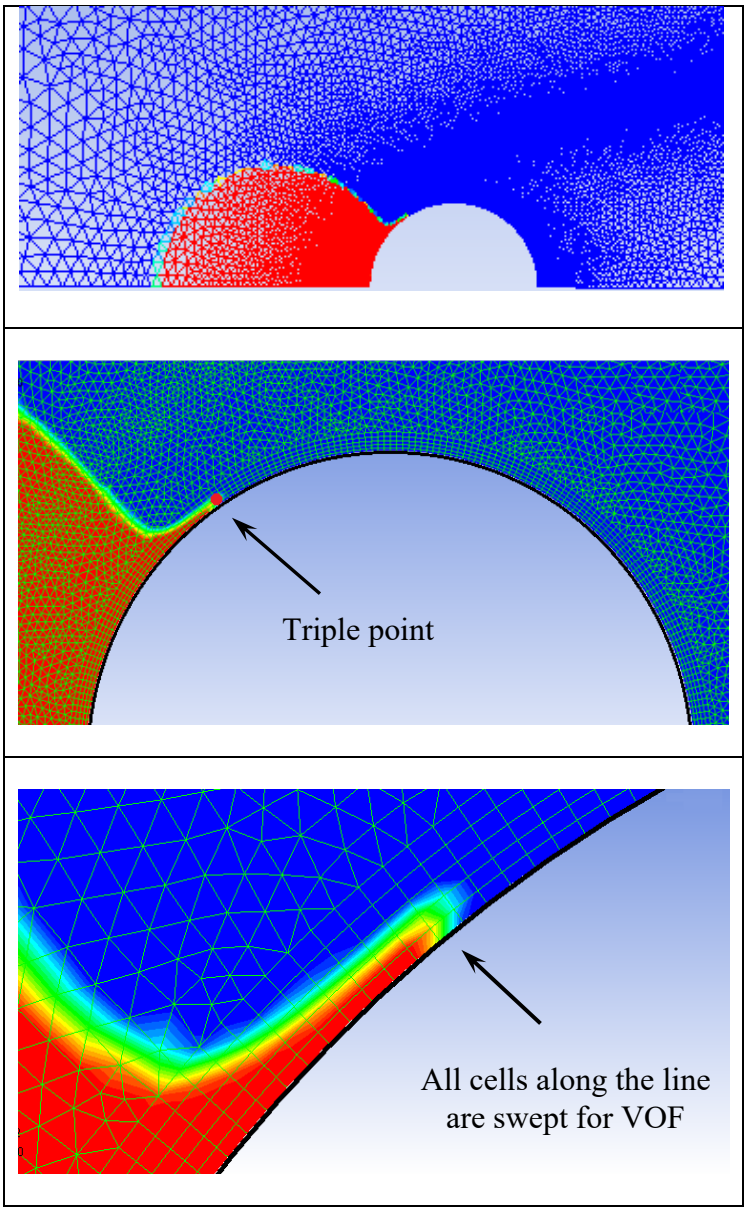

Figure 3-9 *Close up of the triple point on the particle surface; its velocity was calculated and used to find the dynamic contact angle using Eq. (12).*

It should be noted that the velocity of the TP was relatively higher at the initial stages of the impact and it decreased as the particle penetrated into the droplet. Therefore, for the sake of accuracy, the sampling frequency of the UDF in each step (i.e. the value of $t_{i+1} - t_i$) was variable based on the TP velocity calculated in the previous

step. The procedure below, illustrates how the DCA was calculated. First, the curvilinear displacement of the TP on the particle surface was calculated:

$$\Delta S = R_p\left|cos^{-1}\left[(x_2 - x_{G2})/R_p\right] - cos^{-1}\left[(x_1 - x_{G1})/R_p\right]\right| \quad (10)$$

where x_1 and x_2 are TP coordinates in two corresponding time steps. Since the particle was not stationary, location of its centre of mass will change and it is shown by x_{G1} and x_{G2} at t_1 and t_2, respectively.

$$V_{TP} = \frac{\Delta S}{t_2 - t_1} \qquad \Rightarrow \qquad Ca = \frac{\mu V_{TP}}{\sigma} \quad (11)$$

Note that Capillary number (*Ca*) is calculated based on relative velocity of the droplet and the particle. To calculate the contact angle related to the TP velocity, Kistler model was used [24] as shown in Eq. (12) in which θ_e is the equilibrium contact angle, and θ_d is the dynamic contact angle.

$$\theta_d = f_{Hoff}\left[Ca + f_{Hoff}^{-1}(\theta_e)\right] \quad (12)$$

Hoffman function and its inverse used in Eq. (12) are defined as:

$$f_{Hoff}(x) = acos\left[1 - 2\tanh\left(5.16\left(\frac{x}{1+1.31x^{0.99}}\right)^{0.706}\right)\right] \quad (13)$$

$$\left(f_{Hoff}^{-1}(\theta_e)\right)^{0.706} = \frac{1}{5.16}\left[1 + 1.31\left(f_{Hoff}^{-1}(\theta_e)\right)^{0.99}\right]^{0.706} tanh^{-1}\left[\frac{1-cos\theta_e}{2}\right] \quad (14)$$

The dynamic contact angle calculated by Eq. (12) was used as an input to the numerical simulation for all time steps between t_1 and t_2 and the process was repeated for the next time steps.

Figure 3-10 shows variations of DCA as the particle penetrates into the droplet during the impact. The highest contact angle is at the onset of the impact as velocity of the liquid film on the particle surface is maximum. As the impact process proceeds, the liquid film moves upwards on the curved surface of the particle and the velocity of the triple point is reduced. Therefore, the contact angle continues to decrease accordingly until the lamella separates from the particle at which point, the contact angle reaches an almost constant value.

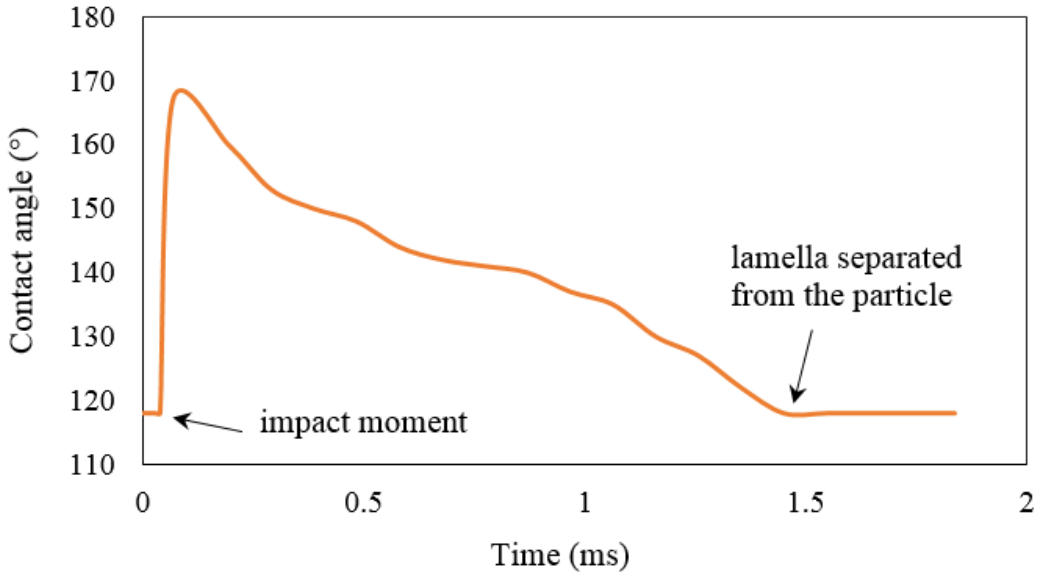

Figure 3-10 *Variations of the dynamic contact angle during impact of a water droplet* ($D_d = 2.9\ mm, v_d = 0.68\frac{m}{s}$) *and a particle* ($D_p = 2.0\ mm, v_p = 6.83\frac{m}{s}$), $\theta_{eq} = 118°$.

Banitabaei and Amirfazli [9] showed that for droplet impact onto a stationary particle, wettability of the substrate plays a crucial role on impact outcomes, up to $\theta = 110°$. For contact angles above $110°$, the impact outcome and the lamella geometry do not change (see Figs. 8(b) and 8(c) in [4]). In the present work, it would be interesting to see how

different the impact outcome would be with and without applying the dynamic contact angle. Figure 3-11 shows the results of two simulations, one with a constant value for the equilibrium contact angle ($\theta = 118°$), and the other when DCA was applied. The difference in lamella length, lamella thickness, and its cone angle during the impact was insignificant in two cases (i.e. the maximum deviation was 1.2%). This was, to some extent, predictable based on the results presented on Fig. 8(c) in [4] which reported no significant difference in lamella geometry for contact angles larger than $110°$ (note that the dynamic contact angle never goes below $110°$ in Fig. 3-10). However, for all other simulations in this chapter, DCA was kept on.

Time (μs)	**Dynamic Contact Angle**	**Equilibrium Contact Angle (118°)**
303	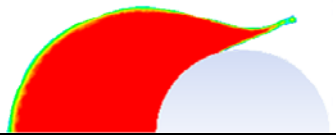	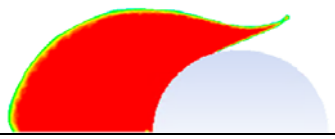
962	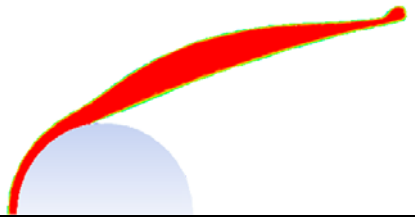	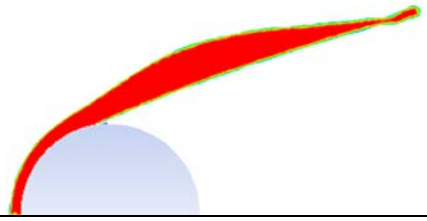
1497	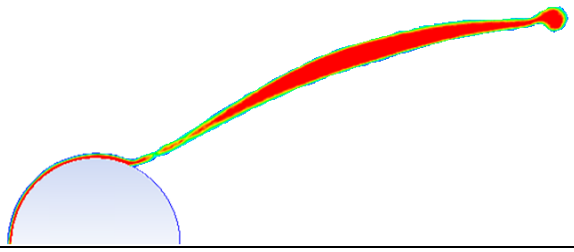	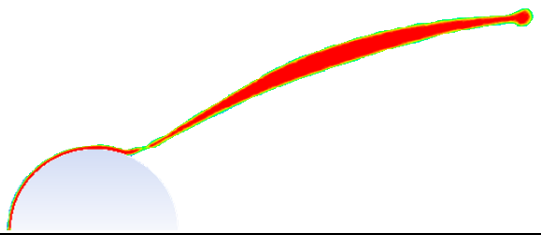

Figure 3-11 *Comparison of the simulation results with dynamic contact angle vs. equilibrium contact angle of* $118°$ *(*$D_d = 2.9\ mm, D_p = 2.0\ mm, v_d = 0.68\frac{m}{s}, v_p = 6.83\frac{m}{s}, \mu = 1\ cP, \sigma = 72\ mN/m$*).*

3.6 REFERENCES

[1] E. Teunou, and D. Pacolet, “Batch and continuous fluid bed coating – review and state of the art,” J. Food Eng. 59, 325–340 (2002).

[2] D. A. Bolleddula, A. Berchielli, and A. Aliseda, “Impact of a heterogeneous liquid droplet on a dry surface: Application to the pharmaceutical industry,” Adv. Colloid Interface Sci., 154,144-159 (2010).

[3] C. Vervaet, and J. P. Remon, “Continuous granulation in the pharmaceutical industry,” Chem. Eng. Sci. 60, 3949-3957 (1995).

[4] C. Josserand and S. T. Thoroddsen, “Drop impact on a solid surface,” Annu. Rev. Fluid Mech. 48, 365–391 (2016).

[5] L. Yan-Peng and W. Huan-Ran, “Three-dimensional direct simulation of a droplet impacting onto a solid sphere with low-impact energy,” Can. J. Chem. Eng. 89, 83–91 (2011).

[6] J. M. Gac and L. Gradon, “Lattice-Boltzmann modeling of collisions between droplets and particles,” Colloids Surf., A 441, 831–836 (2014).

[7] V. V. Dubrovsky, A. M. Podvysotsky, and A. A. Shraiber, “Particle interaction in three-phase polydisperse flows,” Int. J. Multiphase Flow18, 337–352 (1992).

[8] V. Sechenyh and A. Amirfazli, “An experimental study for impact of a drop onto a particle in mid-air: The influence of particle wettability,” J. Fluids Struct. 66, 282–292 (2016).

[9] S. A. Banitabaei, and A. Amirfazli, “Droplet impact onto a solid sphere: Effect of wettability and impact velocity,” Phys. Fluids 29, 062111 (2017).

[10] A. M. Podvysotsky, and A. A. Shraiber, “Coalescence and break-up of drops in two-phase flows,” Int. J. Multiphase Flow 10, 195–209 (1984).

[11] S. Mitra, M. J. Sathe, E. Dorrodchi, V. Pareek, J. B. Joshi, and G. Evans, “In-flight collision behaviour of droplets on a spherical particle falling under gravity,” in NOVA, The University of Newcastle’s Digital Repository, Australia (2013).

[12] L. Xu, W. W. Zhang, and S. R. Nagel, “Drop splashing on a dry smooth surface,” Phys. Rev. Lett. 94, 184505 (2005).

[13] J. C. Bird, S. Tsai, and H. Stone, “Inclined to splash: Triggering and inhibiting a splash with tangential velocity,” New J. Phys. 11, 063017 (2009).

[14] G. Riboux, and J. M. Gordillo, “Experiments of drops impacting a smooth solid surface: A model of the critical impact speed for drop splashing,” Phys. Rev. Lett. 113, 024507 (2014).

[15] http://www.clearcoproducts.com/pure-silicone-standard-viscosity (accessed on Sep. 2018)

[16] I. V. Roisman, E. Berberovi, and C. Tropea, “Inertia dominated drop collisions. I. On the universal flow in the lamella,” Phys. Fluids 21, 052103 (2009).

[17] M. Karimi, “Design and construction of a temperature cell to study the effect of temperature rise on particle–drop impact,” (M.Sc. Thesis), Department of Mechanical Engineering, Edmonton, Alberta, Canada (2013).

[18] K. A. Raman, “Dynamics of simultaneously impinging drops on a dry surface: Role of inhomogeneous wettability and impact shape,” J. Colloid Interface Sci. 516, 232–247 (2018).

[19] H. Almohammadi, and A. Amirfazli, “Droplet impact: Viscosity and wettability effects on splashing,” J. Colloid Interface Sci. 553, 22–30 (2019).

[20] D. Zhang, K. Papadikis, and Sai Gu, “Application of a high density ratio Lattice-Boltzmann model for the droplet impingement on flat and spherical surfaces,” Int. J. Therm. Sci. 84, 75–85 (2014).

[21] D. Zhang, K. Papadikis, and S. Gu, “Investigations on the droplet impact onto a spherical surface with a high density ratio multi-relaxation time lattice-Boltzmann model,” Commun. Comput. Phys. 16, 892–912 (2014).

Chapter 4

Pneumatic Drop Generator: Liquid Pinch-Off and Velocity of Single Droplets‡

4.1 INTRODUCTION

Generating single droplets in a controlled way, also known as drop-on-demand (DoD) technology, is one of the key elements in many industrial processes including inkjet and 3D printing with different materials [1,2], microfluidic systems [3], encapsulation of cells [4], dispensing solder balls onto circuit boards [5], depositing electrically conductive polymers for manufacturing electronic circuits [6], precise dielectric coating between micro-parts [7], and deposition of organic liquid drops in microarrays for biological tests [8].

One of the commonly used methods for single-drop generation is piezoelectric bending plates, whereby applying voltage pulses to a diaphragm, liquid is pushed out of the reservoir and a droplet is ejected from the nozzle. Although piezoelectric drop generators are widely used these days, they are mainly suitable to work within a narrow range of various fluids as they cannot generate droplets of highly viscous liquids. Moreover, since piezo-crystals cannot withstand very high temperatures, they are not generally suitable for generating drops from molten metals [9]. Pneumatic drop generation

‡ This chapter has been published as a journal paper: S. A. Banitabaei, A. Amirfazli, ”Pneumatic drop generator: Liquid pinch-off and velocity of single droplets”, *Colloids and Surfaces A*, **505** (2016) 204-213.

is an alternate technique in which an appropriate pressure pulse is applied to the surface of the liquid in a reservoir. This pressure pulse causes a small liquid jet to emerge from a nozzle attached to a reservoir and eventually a single droplet is detached from the liquid jet [10]. Although pneumatic DoD generators have a lower frequency of drop generation compared to piezoelectric devices, they do not have strict limitations on temperature and viscosity of working liquids.

Pneumatic drop generators do not have any moving part in contact with the liquid which provides for simplicity in construction and robustness in operation. Liquid is filled into a reservoir connected to pressurized air through a solenoid valve. By opening and closing the solenoid valve, a pressure pulse is applied to the surface of the liquid. A nozzle is attached to the reservoir and since viscous shear forces are operating on liquid boundary layer near the nozzle wall, the positive pressure pulse pushes out the central core of the liquid from the nozzle. As the trapped gas leaves the chamber through the pressure relief valve, a negative relative pressure is created in the reservoir that withdraws the liquid jet into the chamber and can prevent generation of satellite droplets. Pneumatic DoD generators have been used to produce droplets from a wide range of liquids and molten metals including water-glycerine mixtures [10], tin, indium, lead, zinc, and aluminium alloys [11–14].

Cheng and Chandra [15] studied a pneumatic drop generator to find the appropriate timing for solenoid valve and also importance of negative pressure on reducing satellite drops. They found that as the amount of water in the reservoir is increased, resonance frequency of pressure pulse and maximum suction pressure will be increased accordingly.

Amirzadeh and Chandra [9] conducted an extensive experimental study on water/glycerine mixtures in a pneumatic DoD generator. They used a nozzle oriented such that to eject drops against gravity by which the probability of dripping and formation of satellite droplets was reduced. They reported a time lag between oscillations of excitation pressure on liquid surface and liquid jet movements in nozzle which increases by decreasing liquid viscosity, or increasing nozzle diameter. They also showed that the suitable conditions for producing droplets is attained for an intermediate value of viscosity. Their findings described what was previously reported in [10] that small droplets could not be produced with very low or very high viscous liquids.

In a pneumatic drop generator, jet pinch-off is an important phenomenon for detaching droplets from the liquid column. An experimental investigation on final stages of dripping droplets pinch-off was performed in [16] for water and ethanol. They found that the minimum neck size and cone angle of the liquid jet, just before the pinch-off, show a self-similar behaviour regardless of the initial conditions of the flow. The self-repeating mechanism of breakup phenomenon was later studied numerically by Lakdawala *et al.* [17]. They explained the mechanism of capillary jet break up which led to formation of the main and satellite droplets due to temporal growth of surface perturbations. Peregrine *et al.* [18] investigated the pinch-off of liquid emerged from a nozzle as well as formation of secondary droplets. Based on experimental observations, they broke down the liquid pinch-off process into several stages including necking, pinch-off of the main drop, liquid column recoiling, and secondary pinch-off for particular configurations. However, they did not look in details of the double pinch-off cases to recognize the possible sub-categories of the phenomenon. They also explained that due to having an unbalanced surface

tension after the first pinch-off, an impulse is given to the recoiling liquid which generates strong undulations on the liquid column.

As mentioned earlier, the effect of various parameters on drop generation in a pneumatic device has been well covered in the literature (e.g. effect of nozzle size [10], valve timing and pressure pulse properties [9,15,19], liquid viscosity and surface tension [9,10]). However, there is no substantive study on velocity of droplets created by a pneumatic single drop generator. Velocity of the droplet has an important effect on dynamics of drop impact and also final shape of a droplet after impact onto a substrate. Here, the main question is: would a droplet achieve an initial velocity due to the applied pressure pulse? Therefore, the objective of this work is to investigate droplet velocity near the moment of drop generation for a pneumatic droplet generator. The effect of nozzle size and physical properties of the liquid on droplet velocity will be studied as well. Finally, two general scenarios for droplet pinch-off are introduced in which droplet velocity will be discussed: single break-off, and double break-off of the liquid jet for cases that a single droplet is generated.

4.2 BRIEF THEORETICAL BACKGROUND

Droplet generation is usually performed either through a droplet free fall (e.g. using a syringe to drip a droplet from a needle) or by applying an initial momentum to a small liquid jet to push it out of a nozzle, as happens in a pneumatic droplet generator.

In a free fall drop generation, a very small droplet forms and sticks to the tip of the needle due to the adhesion force between water and needle, and the drop starts growing in size until gravity overcomes the resistant forces. Therefore, a single droplet is detached

from the needle and starts falling down with an initial velocity of zero. In this method, the droplet size can be reduced by decreasing outer diameter of the needle. Nevertheless, as smaller droplets are generated, the effect of adhesion force becomes more dominant (due to increase of surface area to volume ratio) and therefore using an ordinary needle, it is not possible to generate droplets much smaller than 1 mm.

A thorough review on fundamental and technological aspects of liquid jets was presented by Eggers and Villermaux [20] which includes a detailed explanation for free-surface motion, hydrodynamic instability and singularity formation causing the drop breakup from a jet. Below, just a brief overview is provided.

To form a droplet in a pneumatic drop generator, fluid motion is initiated by kinetic energy of an abrupt pressure pulse applied on the liquid surface to emerge a liquid jet from the nozzle (gravity may also be of help). The resistance to drop formation is due to friction force at the nozzle walls, viscous forces between liquid layers, adhesion force between liquid jet and the nozzle when jet is about to emerge, as well as cohesion force of liquid column at the break-up point. Surface tension (γ) also works to reduce surface area, and its effect is seen through Laplace pressure (ΔP) given by:

$$\Delta P = P_{in} - P_{\infty} = 2\gamma K = \gamma\left(\frac{1}{R_1} + \frac{1}{R_2}\right) \quad (1)$$

where P_{in} is pressure inside the liquid, P_{∞} is ambient pressure, and *R* indicates radii of interface curvatures which is positive for a convex curvature and negative in a concave case. Hereafter, $\frac{1}{2}\left(\frac{1}{R_1} + \frac{1}{R_2}\right)$ is called the mean curvature of the interface (*K)*. As the liquid jet becomes thinner near the break-up point, an increase in curvature is observed which

corresponds to an increase in ΔP based on Eq. (1), which is equivalent to an increase in local pressure inside the neck area (P_{in}). So, the closer to the neck area, the larger the pressure would be inside the liquid. Therefore, a pinch-off in liquid jet will be initiated from the neck area as the fluid is pushed from high pressure area inside the neck outwards. Eventually, the liquid column ruptures and a droplet is generated.

In a simplified form, droplet generation procedure can be represented by the following energy equation:

$$E_{pp} = E_{kin} + E_{surf} + E_{res} \tag{2}$$

where E_{pp} is the total energy transferred to the liquid jet from the pressure pulse, E_{kin} is the kinetic energy that liquid jet acquires, E_{surf} indicates the change in surface energy due to an increase in liquid surface area, and E_{res} represents the collection of energy taken up by viscosity, wall shear stress, adhesion, and cohesion forces. Equation (2) can be used to explain the effect of various physical parameters on drop generation as reported by [9,10,21]. For instance, when a single droplet is generated by a constant pressure pulse, as liquid viscosity is increased, kinetic and surface energy together should decrease according to Eq. (2). If the velocity of the generated droplet remains the same, it means that a smaller droplet should be generated. However, if a liquid with a higher viscosity and a lower surface tension is used, the trade-off between dissipation and surface energy, determines the final size of the droplet. In fact, viscosity and surface tension are two of the main liquid parameters controlling drop generation.

4.3 EXPERIMENTAL SETUP AND MATERIALS

To conduct this study, we developed a new pneumatic DoD system. Three main capabilities were considered in this design: single drop generation without having any unwanted satellite drops, generating micro-droplets in various sizes, and working with different types of liquids.

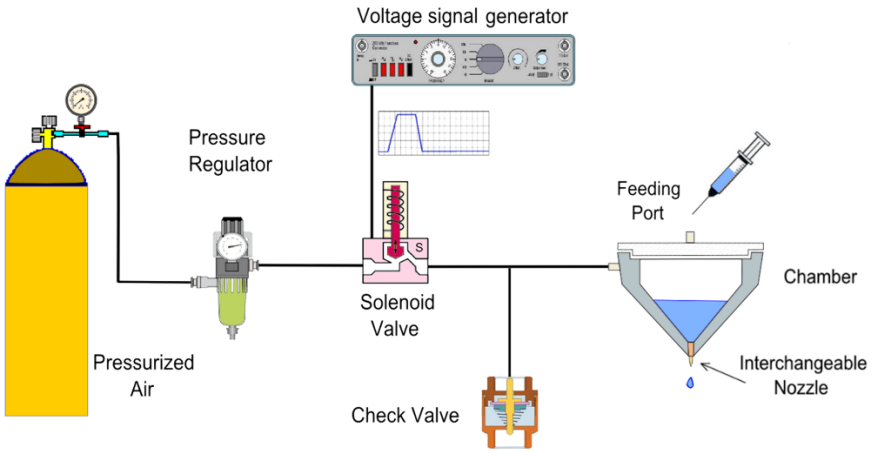

(a)

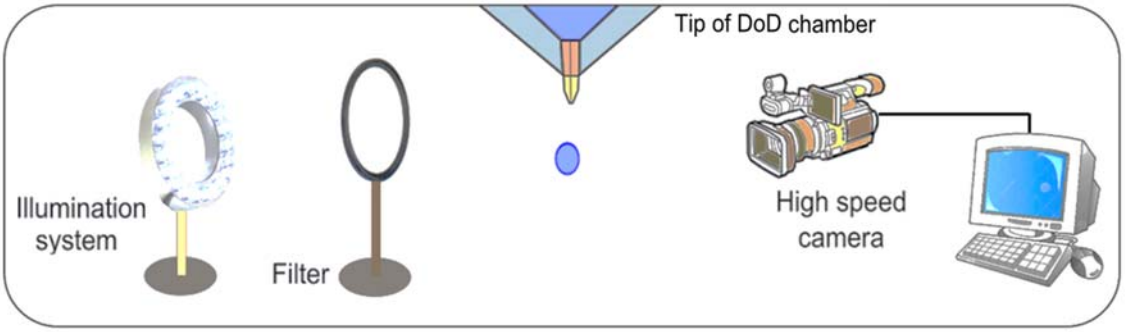

(b)

Figure 4-1 *a) Schematic of the pneumatic droplet generator system, b) Experimental setup used to study size and velocity of generated droplets by DoD system.*

Figure 4-1(a) illustrates different parts of the pneumatic DoD generator system schematically. To generate a single droplet of a desired size and from a specific liquid, an appropriate combination of nozzle size, air pressure and timing for the solenoid valve is required in a DoD system. Four nozzles were used with different orifice sizes of 0.10, 0.15, 0.20, 0.25 mm (maximum tolerance of 0.01mm) made from Sapphire (Swiss Jewel Company). The first three nozzles are from a similar family (planar orifice), while the last one (d_N= 0.25 mm) is a conical nozzle with a different appearance. Although there was a nozzle with smaller orifice size (d_N= 0.05 mm) which worked well with water, eliminating satellite drops for low surface tension liquids was not possible in that nozzle in spite of experimenting with different pressure pulses. On the other hand, using a high viscosity liquid in the pressure range used for these experiments, no droplet could be generated by the above nozzle. Therefore, limitations for generating a single droplet with a specific size exist because of the physical properties of the liquid.

Pressurized air supplied from a 1 MPa cylinder enters a single stage regulator (Festo-LRP-1/4-0.7) which is able to reduce the cylinder pressure in the range of 0 to 70 kPa. This regulator provides steps of 2 kPa increment to allow for a fine adjustment of pressure pulse magnitude. Since the chamber and tubing connections remained the same in all experiments, the pressure value was always measured at the regulator output, and referred to as the line pressure. Maximum response time of solenoid valve is 8 ms and air flow enters the reservoir as valve was trigged by the voltage generator. There is also a connection from the chamber inlet which is open to ambient air to allow the supplied air in the reservoir to evacuate after droplet is generated so to prevent formation of satellite droplets. A check valve with opening pressure of 2.55 kPa was installed at this

vent connection (see Fig. 4-1(a)) to prevent dripping from nozzle caused by air entrance into chamber while solenoid valve was closed. An O-ring was used for sealing of the chamber lid to prevent unwanted pressure drop in the reservoir (see Fig. 4-2).

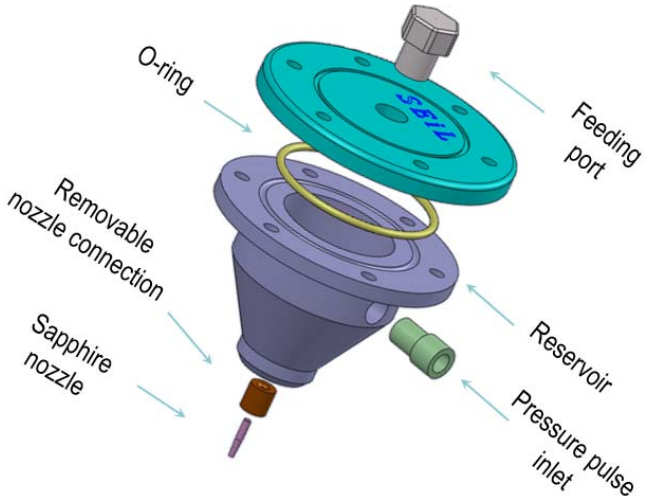

Figure 4-2 *Exploded view of the pneumatic DoD generator chamber as designed.*

Figure 4-2 shows an exploded-view of the drop generator chamber. Reservoir body was made of PEEK in order to be compatible with a wide range of liquids. Moreover, a conical shape was selected for internal wall of the reservoir to facilitate the distribution of pressure pulse without having any abrupt pressure reflection due to the sharp edges. Moreover, nozzle housing was designed to allow fitting of various nozzles in an interchangeable manner such that one would be able to change the nozzle heads without requiring to empty the reservoir. In fact, this facilitates generating droplets with different sizes from the same liquid while the reservoir is full.

As shown in Fig. 4-1(b), an AmScope LED-96S is used for illumination. Droplet generation process was recorded using a Phantom Miro-310 high speed camera having a 25.6 mm x 16.0 mm CMOS sensor with maximum resolution of 1280 x 800 at 3200 fps.

A Tamron Telephoto 180 mm, f/3.5 Macro Autofocus lens was mounted to the imaging system. Image processing techniques were used for droplet size and velocity measurements. The camera was set to 1000 fps and 28 μs exposure time. With an image resolution of 640×480 pixels, the precision of length measurement was determined to be 0.02 mm. However, for investigation of pinch-off phenomenon, the frame rate was increased to 25,000 fps with a 28 μs exposure time and resolution was manually adjusted to 384×288 pixels.

Table 4-1 lists various liquids used in the experiments that were chosen mainly based on their viscosity and surface tension. Water and acetylacetone both have a viscosity near 1cP, but different surface tensions. On the other hand, glycerin 50% with water has almost the same surface tension as water, near 70 mN/m, but a higher viscosity. Therefore, one can compare drop generation results to study the effect of each parameter independently. Acetylacetone is a poisonous and volatile liquid, and the experiments should be done under a fume hood.

Table 4-1 *Properties of liquids used in pneumatic DoD generator, T=25 ºC [22,23].*

Liquid	**Density** (kg/m^3)	**Viscosity** (cP)	**Surface tension** (mN/m)
Water	998	0.89	72.0
Acetylacetone	975	0.82	31.2
Glycerin-water 50% *wt*	1120	5.34	67.4

4.4 RESULTS AND DISCUSSION

4.4.1 DROPLET SIZE AND VELOCITY

Figure 4-3 shows water droplets produced by the new pneumatic droplet generator using different nozzle sizes (d_N). For each case, the corresponding mean drop size (D_d) and velocity (V_d) are shown for comparison. Velocity measurements in all experiments were performed 2 mm below the nozzle exit. However, in order to keep the same frame size and scale for all non-similar nozzles, frames shown in Figs. 4-3 to 4-5 do not necessarily demonstrate the droplet at the exact measurement points. Line pressure (P) was adjusted for each liquid and nozzle size such that only a single droplet was ejected. However, a slight decrease in line pressure (e.g. 2 kPa) generated no drop as the inertia force was not sufficient to overcome surface tension and cohesion force of the liquid jet. But, increasing the pressure above the value shown in Fig. 4-3, led to generation of one or more satellite droplets (see below). All experiments were repeated five times and range of variations for each parameter was calculated. Pressure values indicated are all gauge pressures.

d_N =0.10 mm P =26 kPa $D_d = 0.36^{+0.02}_{-0.02}\ mm$ $V_d = 0.18^{+0.04}_{-0.03}\ m/s$	d_N =0.15 mm P =24 kPa $D_d = 0.40^{+0.04}_{-0.02}\ mm$ $V_d = 0.20^{+0.03}_{-0.02}\ m/s$	d_N =0.20 mm P =20 kPa $D_d = 0.54^{+0.04}_{-0.06}\ mm$ $V_d = 0.17^{+0.05}_{-0.03}\ m/s$	d_N =0.25 mm P =14 kPa $D_d = 0.64^{+0.08}_{-0.04}\ mm$ $V_d = 0.21^{+0.04}_{-0.04}\ m/s$

Figure 4-3 *Size and velocity of single water droplets generated using various nozzle sizes (d_N).*

For small droplets presented in Fig. 4-3, gravity force is in the order of $10^{-6}N$, i.e. not large enough to overcome the resistant forces and release the droplet from the nozzle. Intuitively, one may expect a small droplet generated by a pneumatic device to acquire an initial velocity from the applied pressure pulse (i.e. the droplet is shot out).

Figure 4-3 indicates that as the nozzle diameter increases, the droplet size grows accordingly. However, velocity measurements indicate that droplets do not have a significant initial velocity upon ejection. Moreover, velocity magnitudes are quite similar, and do not change considerably in the range of nozzle sizes tested here.

The experiments described above were repeated using acetylacetone and with the same nozzle sizes. It can be seen from Fig. 4-4 that a decrease in surface tension while viscosity and density of the liquid are similar to water led to generation of smaller droplets for all nozzle sizes. This trend was seen in [10] and is also predictable by Eq. 2 since E_{kin} and E_{res} will remain almost the same while surface tension (γ) decreases. Therefore, for a constant pressure pulse (E_{pp}), droplet size should increase to satisfy Eq. 2. Since E_{pp} is decreased to prevent satellite drops generation, droplet size is decreased accordingly.

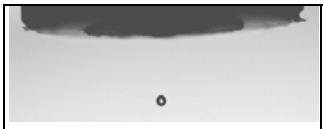	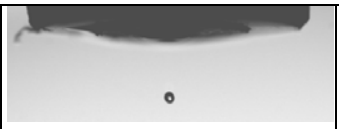		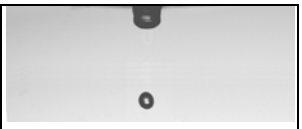
d_N =0.10 mm P =14 kPa $D_d = 0.30^{+0.02}_{-0.04}\ mm$ $V_d = 0.21^{+0.01}_{-0.03}\ m/s$	d_N =0.15 mm P =12 kPa $D_d = 0.34^{+0.04}_{-0.04}\ mm$ $V_d = 0.23^{+0.06}_{-0.04}\ m/s$	d_N =0.20 mm P =10 kPa $D_d = 0.42^{+0.04}_{-0.06}\ mm$ $V_d = 0.20^{+0.02}_{-0.02}\ m/s$	d_N =0.25 mm P =6 kPa $D_d = 0.56^{+0.06}_{-0.06}\ mm$ $V_d = 0.22^{+0.04}_{-0.02}\ m/s$

Figure 4-4 *Size and velocity of single acetylacetone droplets generated using various nozzle sizes (d_N).*

A comparison between acetylacetone droplets with those of water droplets in Fig. 4-3 reveals that there is no considerable change in droplet velocity 2 mm below the nozzle exit. The same tests were also performed for mixture of glycerine-water 50% *wt* which has a density and surface tension very close to water but a viscosity 5 times higher. Based on the data presented in Figs. 4-3 and 4-5, for each nozzle size, an increase in size of droplet is seen as viscosity is increased which agrees well with the results in [9], and can be explained by Eq. 2. Moreover, droplet velocity measurements in Fig. 4-5 proves that as long as droplet generator works in its optimum pressure (to generate stable single drops without having satellite droplets), as the liquid viscosity is increased, no remarkable change in velocity of droplet is observed. This is similar to what was presented in Fig. 4-3 for water with a lower viscosity but similar density and surface tension. A summary of all the results presented above is provided in Fig. 4-6.

It should also be noted that working frequency of a pneumatic droplet generator is usually limited based on the maximum operating frequency of the solenoid valve. For the current device, the maximum working frequency was determined to be 2 Hz for single water droplet generations. As the focus of this work is on velocity of single drops generated without having any unwanted satellite droplet(s), we did not determine the maximum frequency for other systems.

		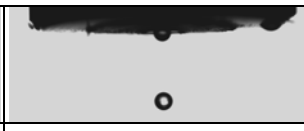	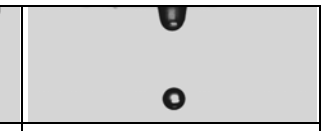
d_N=0.10 mm P =36 kPa $D_d = 0.54^{+0.02}_{-0.02}\ mm$ $V_d = 0.21^{+0.02}_{-0.04}\ m/s$	d_N =0.15 mm P =32 kPa $D_d = 0.56^{+0.04}_{-0.04}\ mm$ $V_d = 0.26^{+0.02}_{-0.02}\ m/s$	d_N =0.20 mm P =26 kPa $D_d = 0.62^{+0.06}_{-0.08}\ mm$ $V_d = 0.25^{+0.03}_{-0.04}\ m/s$	d_N =0.25 mm P =20 kPa $D_d = 0.82^{+0.06}_{-0.08}\ mm$ $V_d = 0.20^{+0.05}_{-0.03}\ m/s$

Figure 4-5 *Size and velocity of single droplets (glycerine-water 50% wt) generated by various nozzle sizes (d_N).*

Comparing the discussion in Section 2 for droplet size generated by free fall with the results for a pneumatic drop generator shown in Figs. 4-3 to 4-5, one can conclude that applying an abrupt air pulse in a typical pneumatic device can significantly decrease the size of the droplets. This is due to applying an extra pressure to push the liquid jet out of the nozzle and break-off a single droplet from liquid column.

Note that for a drop formed on tip of a needle when it falls down due to gravity, velocity is zero upon detachment. In a free fall droplet generation, regardless of air resistance effects, droplet velocity is independent of size and is calculated to be 0.20 m/s, 2 mm beneath the detachment point. Therefore, considering the results presented in Fig. 4-6(b), it is observed that in a pneumatic droplet generator working by its optimal pressure pulse, the velocity of generated droplets is inherently similar to a free fall. Fig. 4-6(b) also indicates that within the range of parameters studied here, regardless of the nozzle geometry and the physical properties of the liquid, velocity of the generated droplet is always the same. As such, a dimensional analysis, seen in literature, may not be necessary given the insensitivity of drop velocity to the above parameters.

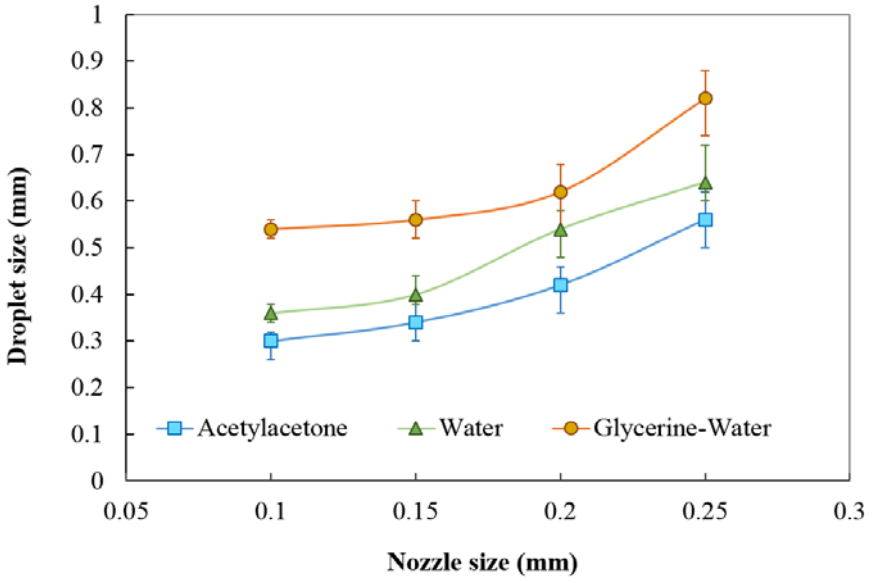

(a)

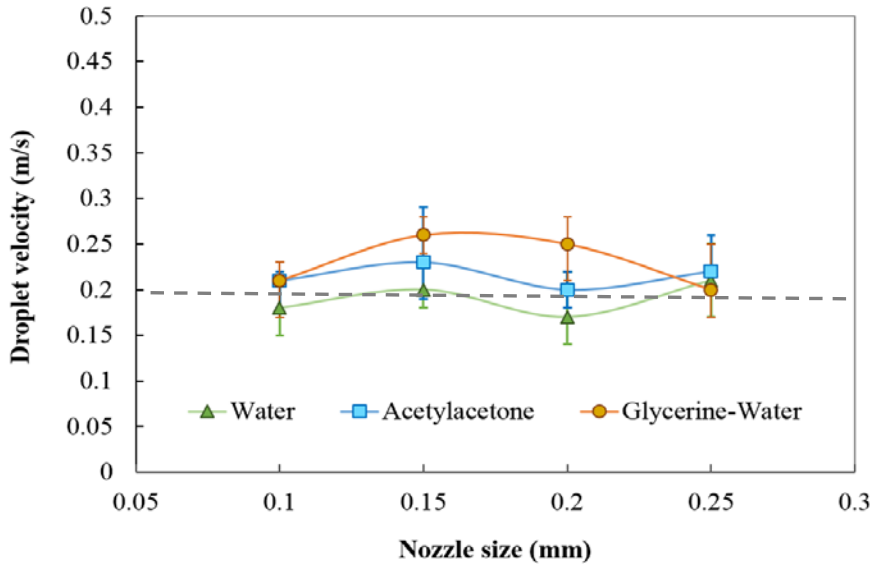

(b)

Figure 4-6 *(a) Size and (b) velocity of single droplets 2 mm beneath the nozzle exit versus nozzle size generated by various liquids. The horizontal dotted line indicates velocity of a drop in free fall 2 mm beneath the detachment point having a zero initial velocity. Solid lines are to guide the eye.*

4.4.2 SINGLE PINCH-OFF

An image sequence of what occurs during a liquid pinch-off in a DoD generator is shown in Fig. 4-7(a) for water. In frame A, solenoid valve was activated by a short voltage pulse (t<10 ms; note that voltage pulse width did not necessarily correspond to the exact time during which the valve was open). In frame B, the valve was still open and pressure pulse was active; however, total energy balance did not favour anymore to continue stretching the liquid column downward. Therefore, to reduce surface energy, the liquid jet started developing a bulge instead of stretching down, while the neck was narrowing as shown in frame C of Fig.4-7. Analysis by image processing and an axisymmetric liquid volume assumption indicates a 1.5% increase of liquid volume in frame C compared to frame B. As such, the valve was still open in frame C (in case valve was closed at this stage, liquid volume should have decreased as liquid column was shrinking to maintain minimum surface energy). However, in frame D of Fig.4-7 valve was closed and pressure pulse decayed. Therefore, the negative pressure applied on top of the liquid inside the reservoir pulled the jet back into the nozzle. At this stage, the liquid neck was sufficiently thin to be broken while the rest of the liquid was sucked back into the reservoir as shown in frames E-H of Fig.4-7. The detached volume of liquid outside the nozzle formed a sphere to minimize surface area (frames F-H). However, since initially in frames B-D the liquid column was shrinking upwards (as it was still connected to the nozzle from one side), the resulting droplet after detachment had a dominant upward velocity as illustrated by frames G and H in Fig. 4-7(a) (see droplet centre of mass). This case clearly demonstrates how a droplet ejected from a pneumatic drop generator may not obtain an initial velocity from the applied pressure pulse. In fact, as shown in Fig. 4-7(c), a pure free

fall of water droplet happens as it stops moving upward and starts falling from a zero velocity (zero slope on displacement curve marked with an asterisk at t=11.2 ms).

The same pinch-off procedure is shown in Fig. 4-7(b) for a mixture of glycerine-water 50% *wt*. As discussed in [10], high viscous liquids tend to create a more stretched neck before breaking up. This effect can markedly mitigate the upward motion of the droplet. However, the droplet positions in frames E-H indicate that droplet had a very low velocity upon ejection.

Taken all together, when a pneumatic drop generator operates with its optimal pressure, a single droplet is generated which is not shot out of the nozzle, and it's velocity profile is ultimately similar to a drop generated through dripping due to gravity.

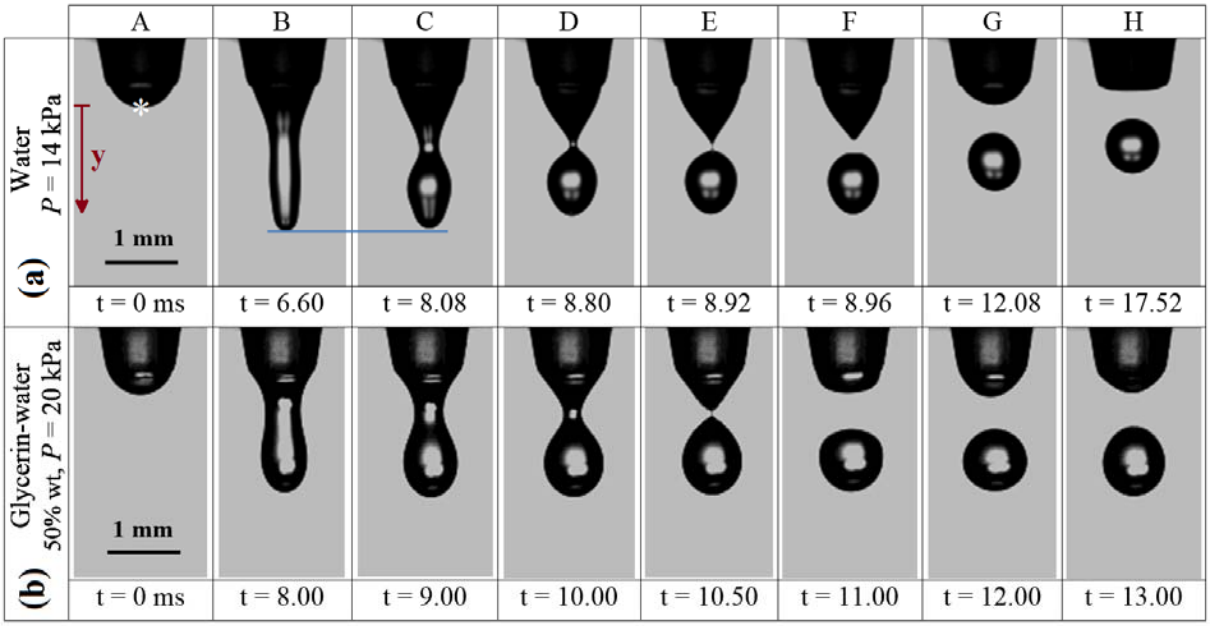

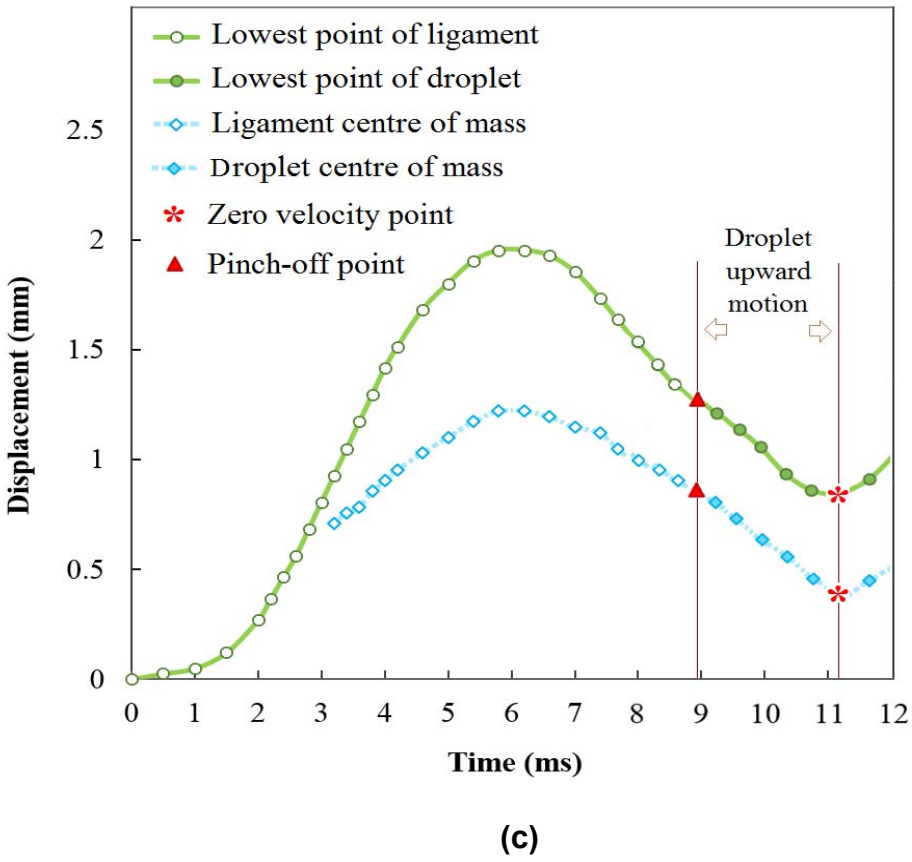

(c)

Figure 4-7 *Image sequence of liquid jet pinch-off in a pneumatic droplet generator for (a) water, and (b) water-glycerine mixture; (c) Displacement of the lowest point and centre of mass for ligament or droplet (d_N=0.25 mm).*

4.4.3 DOUBLE PINCH-OFF

The discussion thus far was centered around droplet generation due to a single jet break-off in liquid column. There are also two interesting alternative scenarios for droplet pinch-off in a droplet generator which have not been considered in the literature. In both of these cases, two pinch-offs took place in the liquid column, but a single droplet was resulted. The reason for two pinch-offs is that the liquid bridge (connecting emerging drop to the liquid bulk at the nozzle) develops two necks rather than one neck as seen in Section 4.2. The existence of two necks results in generation of an intermediate satellite droplet; however, eventually a single droplet is generated as shown in Figs. 4-8 and 4-9. Trajectory of the smaller droplet in each of the two cases is different depending on which of the two pinch-offs took place first. As Fig. 4-8 illustrates, if the liquid bridge which connects the droplet to the emerging liquid from the nozzle first breaks off from the nozzle side (frame C), the liquid column still remains connected to the main droplet (for 0.08 ms in this case). Therefore, to reduce the surface energy, this small liquid ligament started shrinking towards the large droplet. Meanwhile, the remaining neck had become narrow enough for the second pinch-off to took place (see frame D). However, since the small liquid column had a downward velocity (see frames C and D), the small droplet kept moving downward after the pinch-off (frame E). Therefore, it collided with the large droplet and they merged (frames F-I). As a result, a single drop was generated which moves upward (see frames I and J). It should be noted that the large drop had an initial upward motion which was initiated earlier due to the shrinkage of the liquid jet emerged from the nozzle for energy minimization (before frame B) and was already explained in Section 4.2.

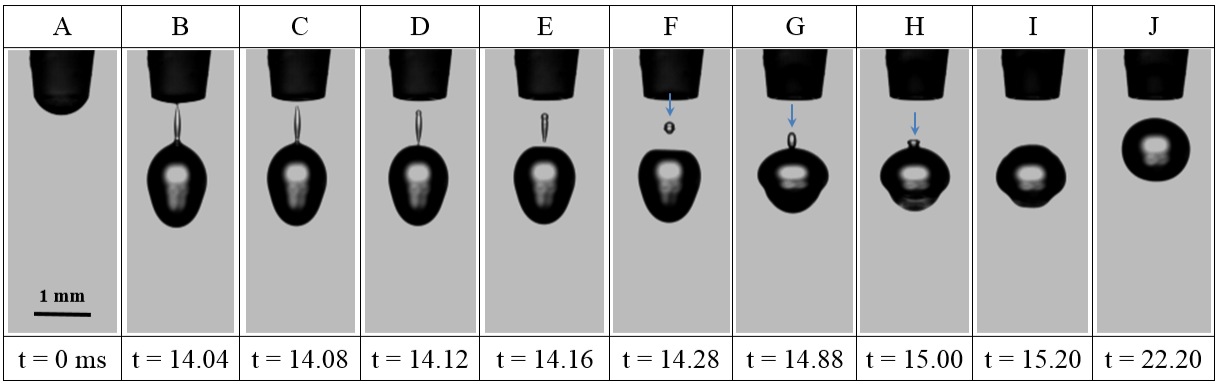

Figure 4-8 *Sequence of images demonstrating the double pinch-off of liquid jet in a pneumatic droplet generator; satellite droplet coalesced with the main drop (water, d_N=0.50 mm, P=6 kPa).*

Figure 4-9 illustrates the second scenario which is similar to the first one, but the sequence of pinch-offs was different. As shown in frame D, the first pinch-off took place in the lower end of the liquid bridge and so the liquid column remained connected to the nozzle. Therefore, it shrank towards the nozzle as shown in Frames D-E, and attained an initial upward velocity before the second pinch-off took place (frame F). Due to this upward motion, the resulting droplet after the second pinch-off moved upward towards the nozzle. Therefore, it coalesced with the liquid at the nozzle exit and again a single drop was eventually generated. It is clear from frames G-J that the resulting large drop had an upward motion as was observed and explained before.

Looking at the results above together with those of Section 4.2, one can understand that the droplet attains an initial motion towards the break-off point. In cases where there are two pinch-off points, the direction for the motion of the satellite drop will depend on which neck will break-off first, but the main droplet will always translate towards the region of break-off whether there are one pinch-off point or two.

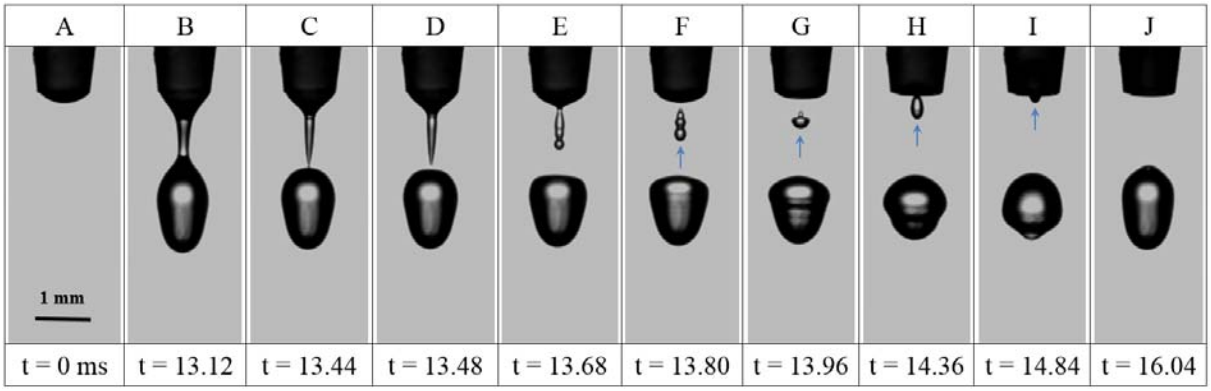

Figure 4-9 *Sequence of images demonstrating the double pinch-off of liquid jet in a pneumatic droplet generator; satellite droplet moved upward back into the nozzle (water, d_N=0.50 mm, P=6 kPa).*

4.4.4 FORMATION OF SATELLITE DROPS

As discussed earlier, upward shrinkage of the liquid column right before pinch-off is the main cause of a droplet's upward velocity after pinch-off (see Fig. 4-7(a)). However, if magnitude of the applied pressure is slightly increased beyond the ideal condition for a single droplet formation, pinch-off phenomenon can lead to a state in which a satellite droplet is about to appear. Therefore, as shown in Fig. 4-10(a), the emerged liquid jet was stretched more (compared to Figs. 4-7 to 4-9) and the shrinkage of the liquid column before pinch-off did not take place anymore. In fact, based on Fig. 4-10(b), the distance of the tip of the liquid jet (shown with an asterisk in frames A and B) from the nozzle exit is continuously increasing before break-up happens. This indicates that pinch-off occurs meanwhile the pressure pulse was still stretching the liquid column. Therefore, the detached droplet neither moved upwards nor fell down like a free fall, but momentum of the pressure pulse gave a downward initial velocity to the droplet upon detachment (0.6 m/s in Fig. 4-10).

However, this state is transitional and not an optimum working point for the drop generator system. As shown in frames E-H, the detached droplet is not stable as liquid pinch-off is followed by formation of capillary waves on the surface of the liquid, and slightly beyond this pressure, satellite droplet(s) will be formed as well.

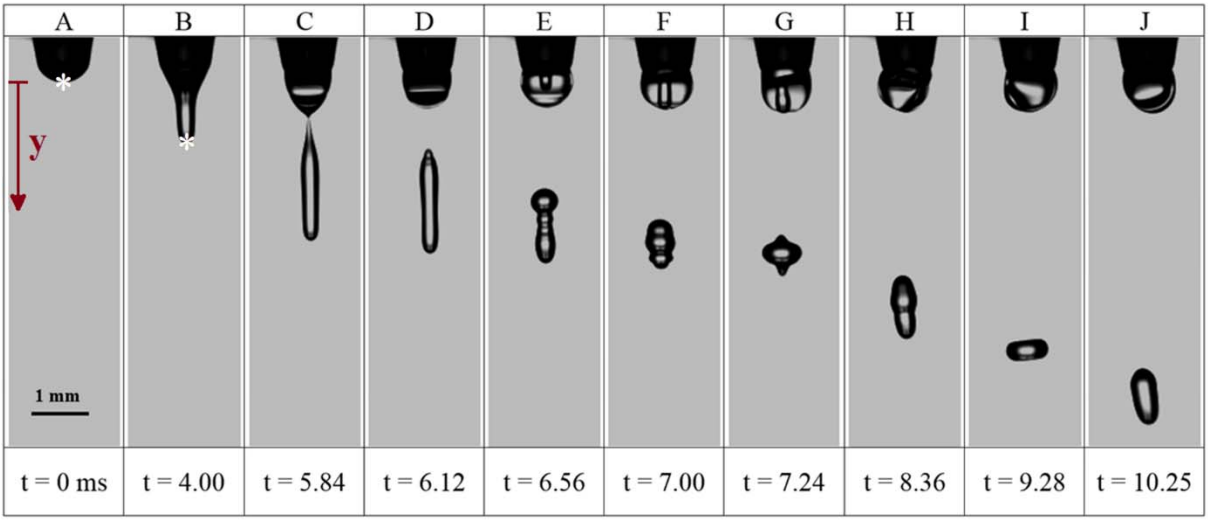

(a)

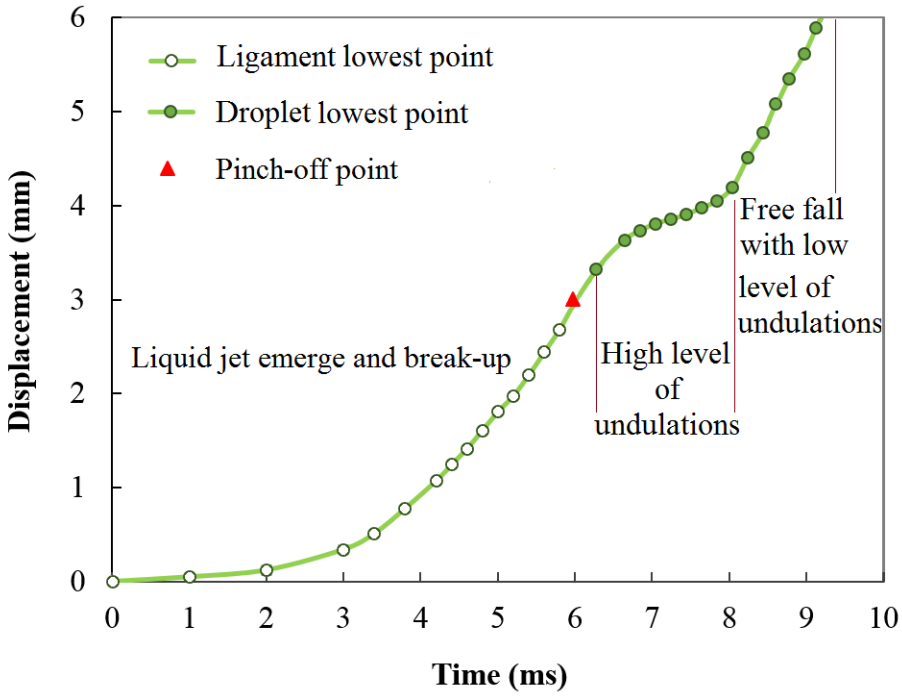

(b)

Figure 4-10 *a) Sequence of images demonstrating a pneumatic droplet generator working in transitional pressure domain, b) Displacement of lowest point of the droplet. (water, d_N=0.25 mm, P=18 kPa, V_d=0.8 m/s).*

When applied pressure is increased in a pneumatic drop generator, the liquid column after ejection experienced more instabilities compared to the case in which the pressure was just enough to generate a single droplet. Therefore, based on the nozzle size, physical properties of the liquid and magnitude of applying pressure pulse, different numbers of satellite droplets with various behaviors might be generated due to the pinch-off. Figure 4-11 shows an example that as a result of the liquid column break-off, three droplets were generated for which size, velocity and trajectory of each droplet can be explained through the same principles mentioned earlier. In frame B, liquid column was

emerged from the nozzle, the first pinch-off happened and the main droplet was formed. In frame C, as the remaining jet shrank to minimize the surface, the negative pressure sucked the liquid back into the nozzle. Therefore, the liquid jet became thinner in its neck and the second pinch-off occurred at the nozzle exit. The order by which these two pinch-offs took place and the time delay between them, gave the detached liquid column an upward velocity (see frame D). Various instabilities of shrinking liquid jet led to break up of a satellite droplet in frame E. In this case, since the pinch-off occurred at the lower part of the satellite drop while it was shrinking downward along with the liquid column, the resulting droplet achieved a downward velocity as shown in frames E-G. Finally, the satellite droplet collided with the larger satellite drop, changed direction due to a quasi-elastic impact and started moving upward. In fact, having a careful observation on Fig. 4-11, a summary of all the phenomena investigated in Sections 4.2 and 4.3 can be reviewed.

It should also be noted that in case of any change in the structure of the chamber, the optimal conditions for drop generation will be changed accordingly. However, one can find the new conditions by which the same pinch-off phenomenon can take place and a single droplet can be generated. To corroborate further this point, one can refer to chambers for DoD in the literature [18,24] that are constructed differently than the current one, but have shown similar pinch-off results (note none of the literature studies examined the droplet velocity). For instance, Lexmond and van der Geld [24] used a different droplet generation method than ours, see Figs. 3 and 4 in their paper, but showed the same double pinch-off scenario explained here for Fig. 4-9. Peregrine *et al.* [18] investigated pinch-off of liquid emerged from a nozzle as well as formation of secondary droplets, and

their results in Figs. 5 to 9 are similar to the pinch-off observations in this study. Figure 8 of [18] also explains undulations appearing on the liquid column as reported here in Fig. 4-11.

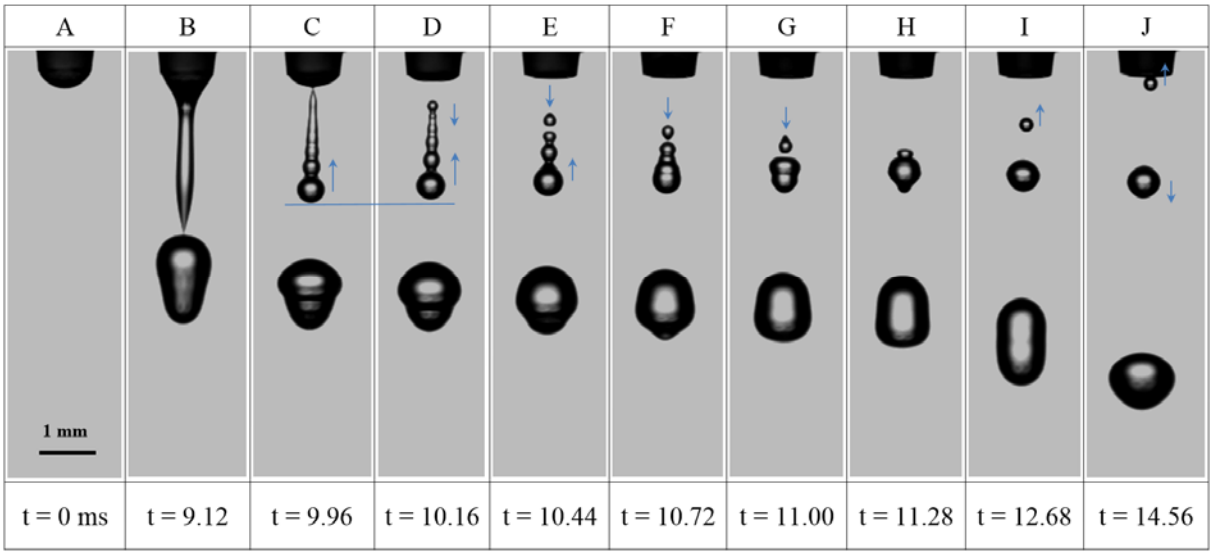

Figure 4-11 *Satellite droplet generation as applying pressure is increased in a pneumatic drop generator (water, d_N=0.50 mm, P=10 kPa).*

4.5 CONCLUSIONS

Velocity of droplets produced by a drop generator has been rarely investigated in the literature. In this work, size and velocity of droplets generated by a pneumatic drop generator were studied for various liquids. A new pneumatic droplet generator was designed having interchangeable nozzles with capability of single drop generation with different sizes. For the selected range of nozzle size, liquid viscosity and surface tension, three different scenarios were observed based on the magnitude of the pressure pulse: 1) When droplet generator works within the range of its optimal working pressure, a single droplet is generated having a negligible initial velocity. 2) If the magnitude of the pressure

pulse is increased away from its optimal point, initial velocity of droplet/ligament will be increased accordingly, but also capillary waves start appearing on the droplet/ligament surface. In such high pressures, instabilities can also break-off the liquid ligament which leads to formation of satellite droplets. 3) If the pressure pulse magnitude takes a transitional value (just beyond the optimal pressure), a secondary pinch-off took place in the emerged liquid jet and a tiny satellite droplet was also generated. This droplet either collides with the main droplet and merges, or moves upwards and merges into the liquid meniscus at the nozzle tip. Therefore, a single drop is finally formed by droplet generator having a zero initial velocity.

4.6 REFERENCES

[1] G. Sui, M.C. Leu, Investigation of layer thickness and surface roughness in rapid freeze prototyping, ASME J. Manuf. Sci. Eng. 125 (2003) 556–563.

[2] M. Fang, S. Chandra, C.B. Park, Building three-dimensional objects by deposition of molten metal droplets, Rapid Prototyp. J. 14 (2008) 44–52.

[3] J. Xu, D. Attinger, Drop on demand in a microfluidic chip. J. Micromech. Microeng. 18 (2008) 065020.

[4] J.F. Edd, D. Di Carlo, K.J. Humphry, S. Köster, D. Irimia, D. A. Weitz, M. Toner, Controlled encapsulation of single-cells into monodisperse picolitre drops, Lab Chip 8 (2008) 1262-1264.

[5] M. Orme, R.F. Smith, Enhanced aluminum properties by means of precise droplet deposition, ASME J. Manuf. Sci. Eng. 122 (2000) 484–493.

[6] B.J. De Gans, P.C. Duineveld, U.S. Shubert, Inkjet printing of polymers: state of the art and future developments, Adv. Mater. 16 (2004) 203–213.

[7] D.J. Hayes, W.R. Cox, M.E. Grove, Micro-jet printing of polymers and solder for electronics manufacturing, J. Electron. Manuf. 8 (1998) 209-216.

[8] M. Schena, R.A. Heller, T.P. Theriault, K. Konrad, E. Lachenmeier, R.W. Davis, Microarrays: biotechnology's discovery platform for functional genomics, Trends Biotechnol. 16 (1998) 301–306.

[9] A. Amirzadeh, S. Chandra, Small droplet formation in a pneumatic drop-on-demand generator: experiments and analysis, Exp. Therm. Fluid Sci. 34 (2010) 1488–1497.

[10] A. Amirzadeh Goghari, S. Chandra, Producing droplets smaller than the nozzle diameter by using a pneumatic drop-on-demand droplet generator, Exp. Fluids 44 (2008) 105–114.

[11] S.X. Cheng, T. Li, S. Chandra, Producing molten metal droplets with a pneumatic droplet-on-demand generator, J. Mater. Proc. Technol. 159 (2005) 295–302.

[12] S. Chandra, R. Jivraj, Apparatus and method for generating uniform sized droplets, U.S. Patent No. 6446,878, 2002.

[13] V. Foutsis, Producing small molten metal drops with a pneumatic generator, M.A.Sc. Thesis, University of Toronto, 2004.

[14] A. Amirzadeh, M. Raessi, S. Chandra, Producing molten metal droplets smaller than the nozzle diameter using a pneumatic drop-on-demand generator, Exp. Therm. Fluid. Sci. 47 (2013) 26–33.

[15] S. Cheng, S. Chandra, A pneumatic droplet-on-demand generator, Exp. Fluids. 34 (2003) 755-762.

[16] J.R. Castrejón-Pita, A.A. Castrejón-Pita, E.J. Hinch, J.R. Lister, I.M. Hutchings, Self-similar breakup of near-inviscid liquids, Phys. Rev. E 86 (2012) 015301.

[17] A.M. Lakdawala, R. Thaokar, A. Sharma, DGLSM based study of temporal instability and formation of satellite drop in a capillary jet breakup, Cem. Eng. Sci. 130 (2015) 239-253.

[18] D.H. Peregrine, G. Shoker, A. Symon, The bifurcation of liquid bridges, J. Fluid Mech. 212 (1990) 25-39.

[19] D. Xie, H. Zhang, X.Y. Shu, J.F. Xiao, S. Cao, Multi-materials drop-on-demand inkjet technology based on pneumatic diaphragm actuator, Sci. China Technolog. Sci. 53 (2010) 1605-1611.

[20] J. Eggers, E. Villermaux, Physics of liquid jets, Rep. Prog. Phys. 71 (2008) 036601.

[21] S.X. Cheng, Development of a molten metal droplet generator for rapid prototyping, M.A.Sc. Thesis, University of Toronto, 2002.

[22] J. Timmermans, The physico-chemical constants of binary systems in concentrated solutions, Vol. 4. Interscience Publishers (1960) 252–267.

[23] http://cameochemicals.noaa.gov, accessed on 8 April 2016.

[24] A.S. Lexmond, C.W.M. van der Geld, The effect of fluid flow on the detachment of drops in the wake of a flat plate, Exp. Therm. Fluid Sci. 29(3), (2005) 363-370.

Chapter 5

Concluding Remarks and Future Works

5.1 CONCLUSIONS

The studies were performed in two main parts: collision of a droplet onto a still spherical particle, and droplet impact on a moving particle in mid-air. For impact on a still particle in Chapter 2, it was understood that the droplet to particle diameter ratio has a significant effect on the impact outcomes. Therefore, according to the literature survey, D_r~1.75 was selected for the investigations and three main aspects of the phenomenon were studied as below:

a) Regarding the impact outcomes for particles of different wettabilities at various impact velocities we found that: For drop impact onto a hydrophilic particle, the droplet was neither disintegrated nor stretched enough to form a liquid film after impact. In fact, those deformations are not energetically favorable. Therefore, the droplet follows the particle curvature and slightly deforms around it in the entire velocity range studied here. However, starting from We~200 for impact on a hydrophobic particle, a liquid film forms as a result of the impact. As the Weber number was increased, the lamella length and cone angle were increased accordingly.

   Furthermore, it was found that the lamella height and base diameter in dimensionless form (H^* and D^*, respectively) increases over time while height of the remaining liquid on the particle (h^*) decreases. For the entire range of impact velocity in which a lamella was formed, all h^* values overlap on a single curve. Likewise, there is a master curve for H^* at various Weber numbers in lamella stretching phase; the

maximum stretching of lamella depends on the droplet velocity upon impact. Moreover, the empirical relation developed for D^* was shown to be valid beyond the current study as it can also predict the impact outcome on similar curved surfaces from other works.

b) Regarding the effect of particle wettability on impact duration, we found that as particle wettability was increased, the elapsed time during the impact was decreased accordingly. When the particle is hydrophobic, for impact velocities larger than 1.8 *m/s* (*We*>162), the droplet creates a thin liquid film after impact. In fact, hydrophobicity of the particle repels the liquid from the surface and causes the droplet to form a conical lamella as it spreads on the particle. This mechanism is mainly effective at the initial stage of impact and before particle penetrates completely into the liquid.

c) Effect of variations of the particle contact angle on lamella geometry was also investigated. For hydrophobic particles, we found that increasing the contact angle from hydrophilic to hydrophobic zone has a considerable effect on geometry of the liquid film and lamella formation. However, increasing the contact angle of a hydrophobic particle after the threshold value of 110° did not have a significant effect on lamella geometry.

In Chapter 3, impact of a droplet onto a spherical particle in mid-air was studied using a numerical simulation tool verified by the experiments. Investigations were mainly to determine how various conditions affect the impact outcomes and change the lamella formation procedure. The concluding remarks are as follows:

I. While the lamella is formed, two opposite flows coexist within the liquid film; one is generated through the momentum transfer from the particle, and the other is created

by the initial velocity of the droplet which is towards the lamella base. Formation of a rim at the lamella base is due to the lower liquid velocity and the surface energy being the dominant player there.

II. A larger droplet-to-particle diameter ratio increased the impact duration but did not change the impact scenario and the collision outcomes ($1.5<D_r<5$). Therefore, a lamella was still formed and two opposite flows existed in a thicker liquid film.

III. A higher liquid viscosity makes the lamella shorter but increases its rim size. Simulation results indicated that when μ is reduced ($1<\mu<350$ cP), the average flow velocity inside the film is accordingly reduced which causes both the lamella thickness and the remaining film thickness on the particle to be increased.

IV. Pressure distribution around the lamella rim measured from the simulation results indicated that when density of the ambient gas was increased to $\rho_{gas} > 5\rho_{air}$, the lift force applied to the liquid film was decreased, bent the lamella downwards, and hindered its stretching. However, for smaller values of ρ_{gas}, the lamella formation was not affected by the ambient gas density.

One of the requirements for studying the impact phenomena is to generate single droplets to be collided to the moving particle in mid-air. In Chapter 4, a pneumatic droplet generator was designed and manufactured with interchangeable nozzles capable of single drop generation without producing any satellite droplet. While performing the tests, size and velocity of droplets generated by the pneumatic drop generator were studied for various liquids. For the selected range of nozzle size, liquid viscosity and surface tension, three different scenarios were observed based on the magnitude of the pressure pulse:

1) When droplet generator worked within the range of its optimal working pressure, a single droplet was generated having a negligible initial velocity.

2) If the magnitude of the pressure pulse was increased away from its optimal point, initial velocity of droplet/ligament was increased accordingly, but also capillary waves started appearing on the droplet/ligament surface. In such high pressures, instabilities could also break-off the liquid ligament which led to formation of satellite droplets.

3) If the pressure pulse magnitude was assigned a transitional value (just beyond the optimal pressure), a secondary pinch-off took place in the emerged liquid jet and a tiny satellite droplet was also generated. This droplet either collided with the main droplet and merged together, or moved upwards and merged into the liquid meniscus at the nozzle tip. Therefore, a single drop was eventually formed by the droplet generator having a zero initial velocity.

5.2 FUTURE WORKS

The following studies are considered as open windows to continue the investigations of the present work:

- ✓ All of our studies here were implemented in ambient temperature. However, literature has shown that temperature of the target surface could have a significant effect on impact products (e.g. Mitra *et al.*, 2013). Effect of the particle surface temperature on outcome of the droplet impact onto a spherical target is worth investigating.

- ✓ We did not measure the roughness of our particles. However, effect of surface roughness on impact products could also be worth studying. This could be performed by adding artificial roughness on the particle surface.

- ✓ We studied the effect of droplet-to-particle size ratio (D_r) by varying the droplet size in the numerical simulation. An experimental verification of this is suggested to be done by changing the particle diameter.
- ✓ As already mentioned, physical properties of liquid are important in impact products. We have studied the effect of viscosity and a similar investigation could be carried out to study the effect of surface tension on impact outcomes.
- ✓ In the present work, only spherical particles were used as the substrate. However, there are numerical studies in the literature showing the effect of non-spherical particles on impact products (see for instance Gac and Gradon, 2014). A similar experimental work could be done to study the effect of particle shape on droplet impact in mid-air.

- ✓ Impact of a droplet onto a hydrophilic particle may leave a coating on the particle surface and the method can be calibrated and used for particle coating. Therefore, a thorough study may be conducted to investigate and tabulate the effect of various parameters such as particle wettability, impact velocity, etc. on coating thickness and efficiency.
- ✓ In the present study, head-on collision of a droplet and a particle was always studied. In case of an off-center impact, the flow dynamics and collision products will be significantly changed due to asymmetric nature of the impact. Therefore, experimental and numerical investigation of off-center impacts is worth investigation. In that case, 3D simulation has to be done.
- ✓ The present study was focused on impact phenomena from before impact until the lamella is fully stretched. Shrinkage of the lamella is the next stage of the impact process which leads to the film break-off and formation of smaller droplets and can be studied for both symmetric and asymmetric impact cases.

Appendix – A

Shedding of Multiple Sessile Droplets by an Airflow §

Due to the capabilities developed in numerical modeling, a side-study was also performed to investigate how the arrangement of multiple sessile droplets affects the airflow around the droplets. In this Appendix, shedding of multiple sessile droplets were examined in various arrangements and on both hydrophilic and hydrophobic surfaces and velocity of onset of motion was determined and studied.

A.1. INTRODUCTION

Shedding of sessile droplets due to a shearing airflow is of particular interest due to its applications in spray coating [1], distillation [2], condensation [3], controlling cell adhesion by the viscous forces of fluids [4], and icing [5]. A droplet which is placed on a surface and is exposed to an airflow, can shed, if the aerodynamic drag force overcomes the droplet's adhesion to the surface. The minimum airflow velocity which leads to a sessile droplet shedding, is called the critical air velocity (U_{cr}). Shedding of a single sessile droplet has been studied before [6-8]. However, often more than one droplet appears on a surface in the above applications. While shedding of a pair of sessile droplets has been investigated through a limited number of experimental and numerical studies [9-10], shedding of multiple sessile droplets remains untouched. Moghtadernejad et al. [9] used

---

§ This appendix has been published and recognized as a Featured and Influential Article by American Institute of Physics. This paper is focused on the results of numerical simulations performed for various conditions of the droplets configuration. The experimental work was already published in a separate paper. I have done all the numerical simulations of this paper: A. Razzaghi, S. A. Banitabaei, A. Amirfazli, The role of drag force in shedding of multiple sessile drops, *Physics of Fluids* **30**, (2018) 087104.

the VOF coupled with LES turbulence to simulate the shedding and coalescence of two sessile droplets placed in tandem on a superhydrophobic surface at 1000<Re<13000 (based on diameter of the sessile droplet). In [9] the initial center to center distance ratio to a droplet's baseline length was 1.88; as the air with a constant velocity flows over the droplets, they moved towards each other, and coalesced. The flow pattern and the drag force variation with time was presented in [9] for both droplets; however, it is not clear how the interaction of the droplets' wakes changes the shedding behavior compared to a single sessile droplet. In our previous work [10] on the shedding of a pair of tandem and side-by-side sessile droplets on hydrophilic and hydrophobic surfaces, our results indicated that the critical air velocity (U_{cr}) can increase by 42% (compared to a single droplet) depending on the droplet pair's arrangement, spacing, and substrate wettability. Also, we determined the range of the spacing within which a pair of droplets are interacting; beyond this range, sessile droplets shed independently, at the U_{cr} of a single droplet.

In the literature, shedding of multiple sessile droplets in the presence of an airflow has not been studied. Drag and adhesion are the two forces that co-interact leading to the shedding of sessile drops. As discussed in our earlier work [10], one can expect that the adhesion force of a sessile droplet not to be affected significantly due to presence of a neighboring droplet.

To form a basis, due to a lack of information for sessile drops, we first review the drag force variation with arrangement, and spacing, for multiple suspended bodies. Tsuji et al. [11] experimentally studied the turbulent flow (Reynolds of ~40000 inside a tube)

over a group of solid spheres arranged in the form of a repeating square and hexagonal grids, while the center to center distance between any two spheres was twice as the diameter of each sphere. They reported that regardless of the type of the arrangement, all spheres within a repeating grid showed a lower drag coefficient compared to a single sphere. As the number of repeating cells increased, the drag coefficient for each sphere decreased; also, the spheres in hexagonal arrangement showed a larger drag coefficient compared to those in a square arrangement. At a similar spacing of spheres (ratio of the center to center distance to the diameter of a sphere) to that of [11], Liang et al. [12] studied the drag coefficient for suspended solid spheres in hexagonal, and cubical arrangements at $Re \leq 100$. Their results indicate that in contrast to [11], a sphere in both arrangements, experienced a higher drag coefficient compared to that of a single sphere. This could be due to difference in flow regimes, i.e. turbulent in [11] and laminar in [12]. Still, both [11] and [12] agree that in a hexagonal arrangement, spheres show a higher drag coefficient value compared to that of a cubical arrangement. In [12], as spacing was increased (from 2 to 2.5), the drag coefficient decreased by 5%. Zhu et al. [13] also emphasized the significance of the spheres' spacing on the drag coefficient which is experienced by a solid sphere placed at the center of cubically arranged spheres at Re of 23. In [13] there was a maximum 38% increase in drag coefficient at spacing of 2.5. However, the amount of changes in drag coefficient, with respect to spacing, can vary significantly from one study to another. Ozgoren [14] experimentally (using particle image velocimetry technique) obtained the flow pattern over three suspended spheres arranged in an equilateral triangular configuration; in [14] the spacing ranged from 1 to 2.5 and the Re number of the spheres was 5,000. They showed the flow pattern is changing with the

spacing and the interaction of the two downstream spheres, which led to the fluctuation of the whole flow field.

You et al. [15] numerically simulated the flow over multiple spheres in a cubical arrangement at Re<100. Their results show that similar to [12], by reducing the spacing between the spheres, the drag coefficient increases. For three suspended solid spheres arranged in a linear array, Maheshwari et al. [16] numerically obtained the flow pattern and the drag coefficient values. They found that when the spacing is equal to 2, the drag coefficient on all spheres is less than that of a single sphere; the lowest drag coefficient was for the middle sphere. As the spacing increased to 4, the drag coefficient on the upstream sphere increased beyond the value for a single sphere.

Considering the above literature, for multiple suspended spheres, compared to a single sphere, drag coefficient is significantly affected due to the interaction of the flow over the neighboring spheres. The type of the arrangement can alter the value of the drag coefficient; typically, spheres in a hexagonal arrangement have a higher drag coefficient compared to those in a cubical arrangement [11] [12]. The change in drag force was also affected by the flow regime. The above studies also showed the effect of the spacing and arrangement on the drag force is different for a pair of spheres than that of multiple spheres. For instance, in [15], increasing the spacing of suspended spheres results in increasing the drag coefficient on a pair of spheres arranged in tandem, but decreasing the drag for multiple spheres arranged cubically. As such, one can expect that the shedding of multiple sessile droplets will also be influenced by the arrangement types and the spacing of sessile droplets, but the question is: how?

The current study is carried to investigate the critical air velocity for shedding of the upstream droplet(s) in various arrangements such as, equilateral triangle, square, reversed equilateral triangle, and diamond. Also, how the findings for shedding of a pair of sessile droplets can be extended to the case of multiple sessile droplets within the above arrangements, is addressed in this study.

A.2. METHODS

A.2.1. EXPERIMENTAL METHODS

Figure A-1 shows the schematic of the experimental setup used. The experiments were performed inside a closed-loop wind tunnel; the height, width and the length of the test section is 6.4, 10.2 and 30.5 cm, respectively. Maximum airflow of 12 m/s is generated by a EBM-Papst fan, and to control the speed of the airflow, a voltage regulator was used to increase the speed of the fan. The level of turbulence in tunnel is 0.2 % (at 8.65 m/s); and at the maximum airflow velocity, the flow inside the test section is laminar; for details see [10]. The speed of the airflow was measured using an EE75 hot film anemometer. The experiments were conducted for droplets' Re number ranging from 547 to 812 ($Re = {\rho U_{cr} H}/{\mu}$, where U_{cr} is the air velocity at the incipient motion of upstream droplets, and H is the height of the sessile droplet).

Figure A-2 shows the arrangements for sessile droplets. These arrangements can be considered as a repeating unit cell in a population of droplets (e.g. seen in dropwise condensation). All sessile droplets within an arrangement had the same size, and experiments were conducted with 5 and 10 μl DI water droplets. Droplets were placed on

hydrophilic and hydrophobic surfaces by a syringe; immediately after droplets were placed, air speed was increased with the rate of ~1 m/s^2 until the shedding was achieved. Image J software was used to measure that the desired spacing between the droplets was achieved (error for the spacing was ~4%). No significant evaporation was observed during the shedding process as the experiments typically took 10 seconds to complete after the start of the airflow. Hydrophilic surface was an aluminum substrate that was spin coated using a PMMA solution [2% (w/w) PMMA in Toluene]; advancing and receding contact angles were 74° and 58°, respectively. Hydrophobic surface was an aluminum substrate that was spin coated using a Teflon solution [5:1 (v/v) FC-75, 3-M / Teflon AF]; advancing and receding contact angles were 122° and 107°, respectively.

Dimensionless spacing (S) is defined as the droplets' center to center length divided by a droplet's baseline length (as measured on the plane of the substrate). The baseline length of a 10 μl droplet on hydrophilic and hydrophobic surface is 4.32 and 2.63 mm, respectively. For the other droplet volume, these information is provided in the Supporting Information. For a constant droplet volume, given that S depends on droplet geometry and droplet geometry is affected by the surface wettability, the droplets' separation and wettability cannot be independent of one another. As will be shown later, taking S as a dimensionless parameter for different surface wettabilities will not affect the conclusion, but it will provide a more compact form of analyzing the problem. In our previous study [10], for a hydrophilic surface, the upstream droplet in a tandem arrangement showed a maximum ~42% increase in U_{cr} (compared to that of a single droplet) at S≈1.5. For two droplets in side-by-side arrangement, the maximum increase in U_{cr} (~30% compared to that of a single droplet) was observed at S≈3.5 [10]. For a

hydrophobic surface, these values of spacing were 1.5 and 2.5, respectively [10]. For the arrangements mentioned in this study, which are mostly formed by combining the tandem and the side-by-side arrangements, these two spacing were considered, so to allow observation for large changes in the U_{cr}.

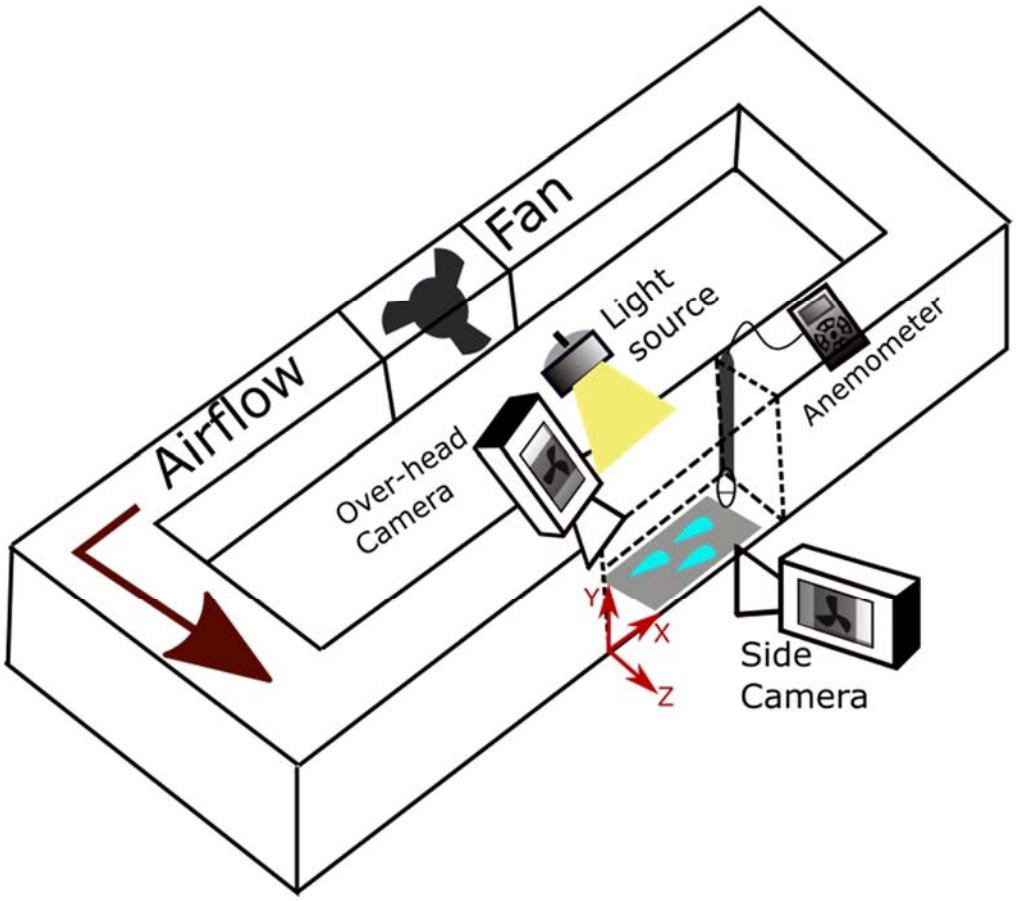

Figure A-1 *Schematic view of the experimental setup; the closed loop wind tunnel, high speed cameras, light source, and anemometer are shown.*

To track the shedding of the sessile droplets, two Phantom high speed cameras (one for side, and one for overhead view) were operating synchronously, capturing

images at 450 frames per second. The incipient motion is defined as the moment when the contact line of the upstream droplet(s) moved 5 pixels (220 μm) on the surface in accordance to our past practice [6] [10]. The air velocity at the incipient motion is the so called critical air velocity (U_{cr}). Experiments were repeated three times and the standard deviation of the dataset is reported as the error.

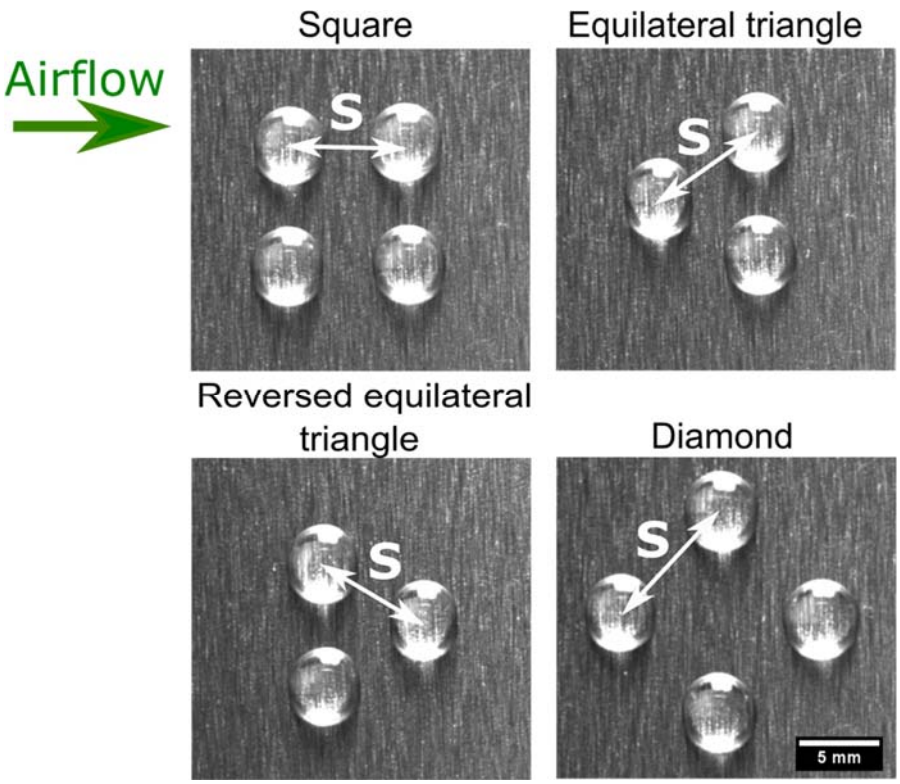

Figure A-2 *Sessile droplets in various arrangements on a hydrophilic surface. Droplets were identical for each arrangement. The apparent texture of the solid substrate has no notable effect on the results as there was a 1.3% deviation in the U_{cr} when surfaces were turned 90°.*

A.2.2. NUMERICAL METHODS

To enhance our understanding of the flow interaction with the droplets at the moment of the incipient motion, a 3D numerical simulation was performed. The governing equations of continuity and momentum are:

$$\nabla \cdot \vec{U} = 0 \tag{1}$$

$$\rho \frac{D\vec{U}}{Dt} = -\nabla p + \mu \nabla^2 \vec{U} \tag{2}$$

where μ is the dynamic viscosity, and ρ is the density of air.

We considered a steady-state simulation rather than a transient one, since flow interaction with the droplets at the moment of incipient motion was of interest in this study. It means that the time-dependent velocity term in Eq. 2 is absent in the simulations. For simplicity, we considered droplets as solid objects; the geometry of the solid objects was fashioned after the shape of sessile droplets at the incipient motion. Note that for the actual droplets there would be a small degree of slip as a result of shear stresses on the droplet interface, which was not considered in simulations. The details regarding the geometry of the objects, representing the sessile droplets at the moment of incipient motion, is provided in the Supporting Information.

The computational domain, and the position of the simulated droplets is shown in Figure A-3 for $10\mu l$ droplets. The dimensions of the domain are considered 1.5 times larger than the dimensions at which velocity and pressure fields show steady conditions

to ensure the independence of the results from the domain size. The upstream droplet(s) were positioned 27 mm downstream from the inlet (i.e. ~ 6 times the droplet's baseline length). Note that the droplets' height is at the same order of the boundary layer thickness (velocity profile in the Y direction is provided in the Supporting Information).

At the inlet, uniform airflow velocity was imposed. The value of the fluid velocity was taken from the experimentally observed U_{cr}, for each case. The "pressure outlet" walls of the domain were at the atmospheric pressure, and had the same velocity magnitude as the inlet. On the surface, there was "no slip" condition, so the boundary layer only forms on the bottom wall. ANSYS Fluent 18 software was used to solve the equations above. SIMPLE solution with a second order pressure and a second order upwind momentum for incompressible flow, were used.

Size of the mesh inside the boundary layer and around the simulated droplets was 0.01mm, and it was 0.5mm in the rest of the domain. To ensure the grid independency, the mesh size was reduced to a quarter of the current sizes. However, no notable changes in the results were observed, while the computational time was significantly increased.

Note that the drag force which can be calculated through the simulations is not the objective. As such, our simulation was not focused on the exact value of the drag as the flow velocity changes, but rather on how the arrangement of droplets and their spacing affects flow field. As such, we wished to glean fluid dynamics information from simulations about reasons for the observed shedding behavior in the experiments.

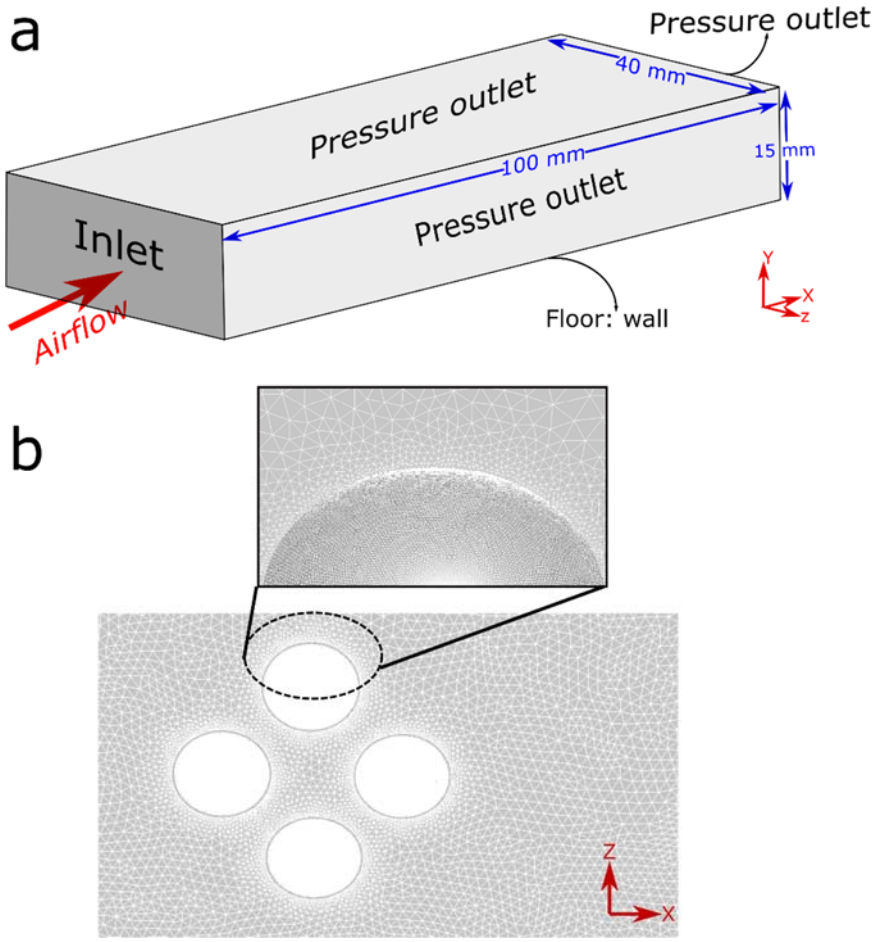

Figure A-3 *(a) Computational domain and the boundary conditions; (b) Mesh at the X-Z, Y=0 plane for diamond arrangement of 10μl simulated droplets at S=1.5. The inset shows the mesh density around the surface of the simulated droplets at the X-Y plane.*

For the numerical simulation, the velocity field and the streamline pattern for each arrangement was examined through plots at the X-Z, Y=0.5 H plane, where H is the simulated droplet's height (e.g. it is 1.4 mm for a 10 μl simulated droplet on a hydrophilic surface). Due to the no-slip boundary condition on the solid substrate, the simulation plots

at the X-Z, Y=0 plane is not interesting to observe. For interested readers, plots at the X-Z, Y=0.75 H plane are provided in the Supporting Information.

To determine the interaction intensity in each arrangement, different parameters, e.g. velocity field, vorticity field, or the size of the vortices cell, can be used. In this study, the length and form of the ring-like vortices from numerical simulations was used. In the Supporting Information, the vorticity field is also presented. It should be mentioned that regardless of which comparison criteria is used, the conclusion regarding the effects of arrangement and spacing on the critical air velocity remains the same.

The vortex length was measured from surface of the simulated droplet to the point where streamlines converged together. Note that in the Supporting Information it is shown that the vortex length, for each case, is the same for X-Z planes with two different Y values. It has been shown by Chen and Wu [17] that at a constant airflow velocity, the compression of the vortices cell at the aft of a suspended solid sphere (due to the presence of a neighboring sphere) results in reduction of the form drag. For the *Re* number studied in this chapter ($547 \leq Re \leq 812$), the relative importance of the form drag is much higher than the friction drag [18], so the compression of the vortices cell is an indication of the aerodynamic drag force reduction. However, one should note that as simulations were conducted at the airflow velocity of U_{cr}, aside from droplets' interaction, the change in the airflow velocity from case to case may also lead to variation of the size and form of the vortex cells. To elucidate this point, Figure A-4 shows the velocity field, and streamline pattern for a single droplet ($10\mu l$) on a hydrophilic surface at two different airflow velocities: 6.1 m/s, and 8 m/s. The former velocity is the U_{cr} for a single sessile

droplet and the latter is the average U_{cr} for the upstream droplet(s) in the triangle, square, reversed triangle, and diamond arrangements, at S=1.5. By increasing the airflow velocity (from 6.1 to 8, i.e. by 31 %), the ring-like vortex deforms and compresses by 27%, see Figure A-4.

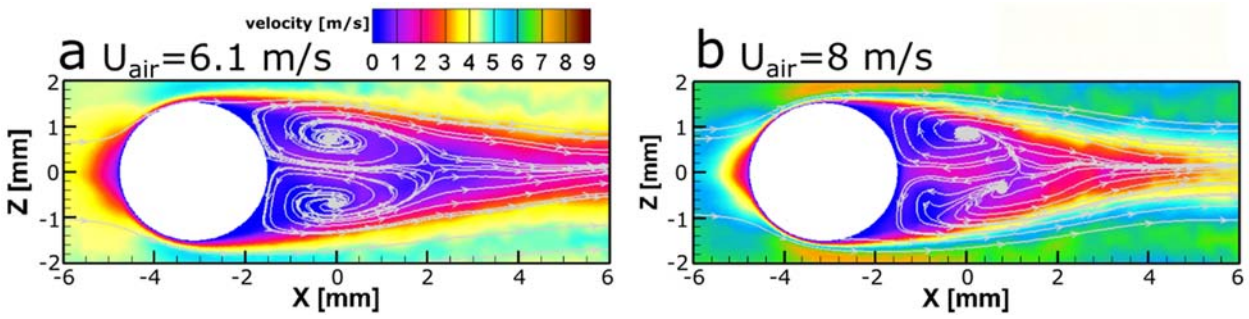

Figure A-4 *Time-independent velocity field and streamline for a single simulated droplet at two airflow velocities of a) 6.1 m/s, and b) 8 m/s. At 6.1 m/s the length of the ring-like vortex is 3.7 mm. At 8 m/s, vortex ring length is 2.7 mm. Plots are for a 10 μl simulated droplet on a hydrophilic surface at the X-Z, Y=0.5 H plane. Color plots online.*

A.3. RESULTS AND DISCUSSIONS

In all arrangements and any spacing, the upstream droplet(s) shed first. At spacing of S=1.5, the common behavior seen was that the upstream droplet(s) hit the downstream droplet(s), and shed as a larger unit. So, our focus in this study is on comparison of shedding, and more specifically, the U_{cr} for the upstream droplets, in various arrangements. To provide an overall view of findings, first, Figure A-5 shows the U_{cr} /$(U_{cr})_{single}$ for the upstream droplet(s) in various arrangements on a hydrophilic (PMMA) surface. A figure similar to Figure A-5, but for 5 μl droplets is provided in the Supporting Information. The amount of change in U_{cr} /$(U_{cr})_{single}$ with respect to type of arrangement and spacing, is very similar for both droplet sizes. The results for droplets on a

hydrophobic (Teflon) surface will be discussed later when effects of surface wettability is presented.

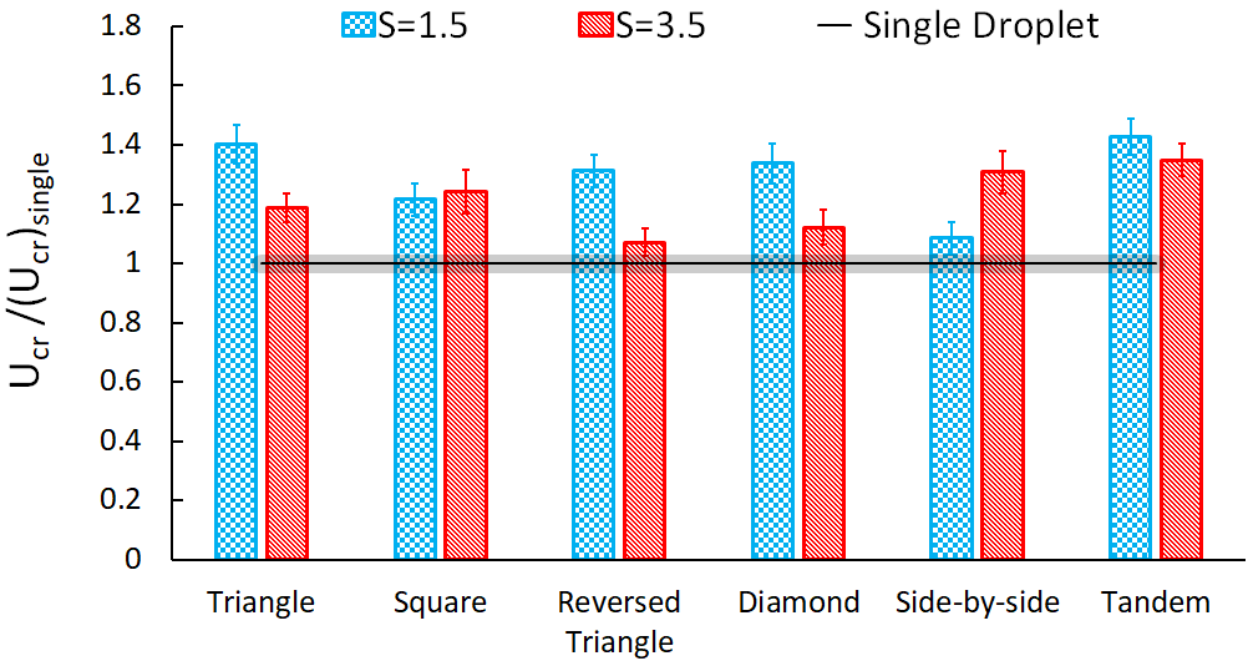

Figure A-5 *Critical air velocity ratio for the upstream droplet(s) in different arrangements at two spacing (S) values. The data shown is for 10 μl droplets on a hydrophilic (PMMA) surface. The error of the Ucr for the single sessile droplet is denoted by the shaded band. Data for tandem and side-by-side droplets are reproduced from [10].*

Below, detailed discussion for various arrangements, and the effect of wettability is provided.

A.3.1. EQUILATERAL TRIANGLE ARRANGEMENT

As it is seen in Figure A-5, the upstream droplet in an equilateral triangle arrangement shows a 40% increase in U_{cr} (compared to that of a single sessile droplet) at S=1.5. As spacing increases to 3.5, U_{cr} decreases; but it is still 18.6% higher than the

value for a single droplet. Figure A-6 shows the velocity field and streamlines for droplets arranged in an equilateral triangle configuration at the X-Z, Y=0.5 H plane. At S=1.5 (Figure A-6(a)), the vortices at the rear of the upstream droplet shrink in length, with respect to that of a single droplet, by 73%. Considering the effect of the airflow velocity on the vortex length (Figure A-4), the observed reduction in Figure A-6(a) cannot be solely due to a higher airflow velocity. The suppression of the flow at the rear of the upstream droplet is similar to that observed by Ozgoren [14] for three suspended spheres in an equilateral triangle arrangement at S=1.5, and Re of 5,000. The streamlines were squeezed at the aft of the upstream droplet due to the blockage effects of the two downstream droplets, which leads to reduction of drag. So, a higher air velocity is required to overcome the adhesion force.

At the spacing of 3.5 (Figure A-6(b)), the upstream droplet's vortex cell shows a 19% compression compared to that of a single droplet. Considering the above discussions, the compression most likely is due to a higher airflow velocity for triangle arrangement at S=3.5, and not due to the interaction of the simulated droplets. The increase in U_{cr} which were observed in experiments, however, implies that still exists a degree of interaction between the droplets at S=3.5. In fact, assumptions made to simplify the simulations, e.g. steady-state solution, and using simulated droplets, limits the exact observation of the interaction between droplets (e.g. due to oscillation of droplets seen in experiments). Still, both experimental, and simulation results indicate that the interaction between the droplets decreases with spacing, and the U_{cr} approaches the value for that of a single droplet.

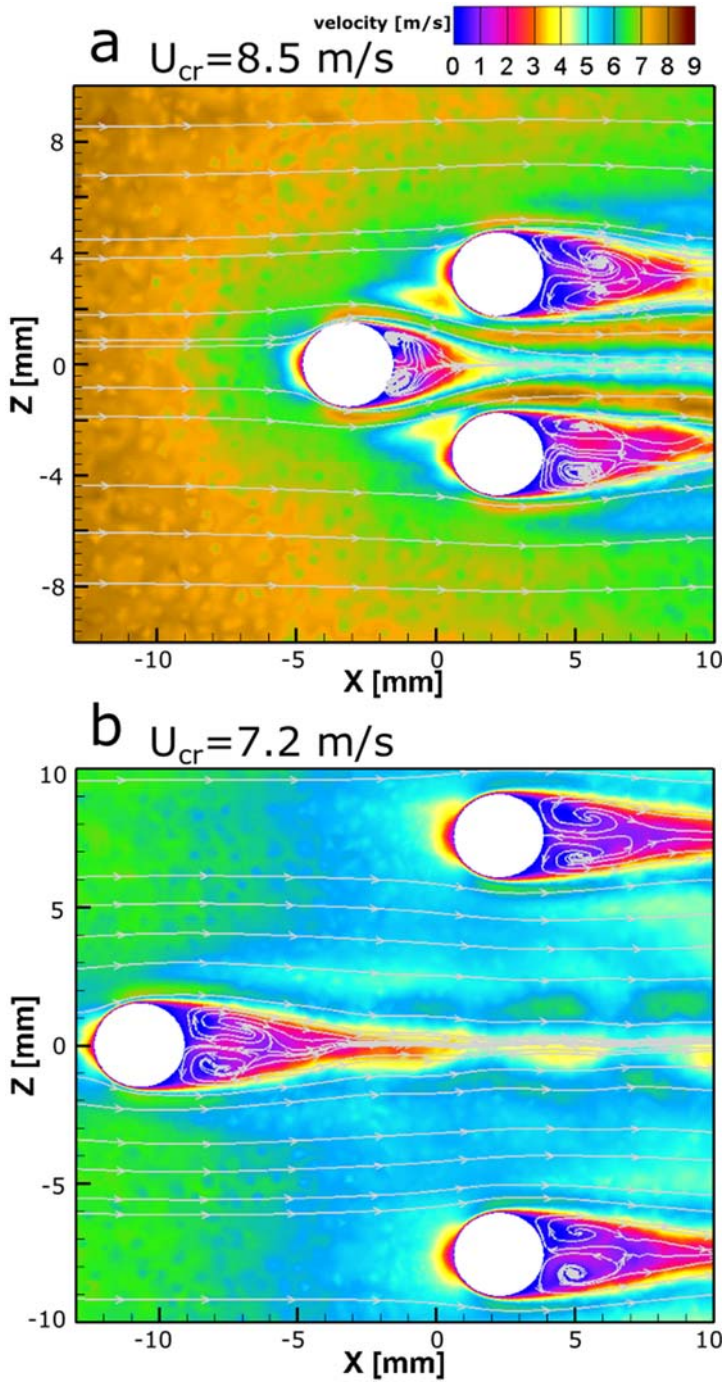

Figure A-6 *Time-independent velocity fields and streamline patterns for three simulated droplets in an equilateral triangle arrangement at a) S=1.5, and b) S=3.5. Plots are for 10 μl simulated droplets on a hydrophilic surface at the X-Z, Y=0.5 H plane. Color plots online.*

A.3.2. SQUARE ARRANGEMENT

Square arrangement of four droplets is formed by two pairs of tandem droplets placed side-by-side; the $U_{cr}/(U_{cr})_{single}$ for the upstream droplets in a square arrangement is shown in Figure A-5. For comparison, the $U_{cr}/(U_{cr})_{single}$ of the upstream droplet in a tandem arrangement, and two droplets in a side-by-side arrangement [10] is also shown in Figure A-5. At the spacing of 1.5, the upstream droplets in a square arrangement show a U_{cr} higher than that of a pair of side-by-side droplets, but lower than that of the upstream droplet in a tandem arrangement. By increasing the spacing to 3.5, no significant change in U_{cr} is observed for the upstream droplets in a square arrangement.

The velocity fields and streamline patterns for tandem, side-by-side, and square arrangements at S=1.5, at the X-Z, Y=0.5 H plane, is shown in Figure A-7. In both tandem and square arrangements (Figure A-7(a) and Figure A-7(c)), the ring-like vortices fill the entire space between the upstream and downstream droplets. This is similar to the streamline patterns obtained by Tsuji et al. [19] over two suspended spherical particles placed in tandem at S=1.5 for Re of 250. As a result of flow suppression at the gap between the upstream and downstream droplets, the drag reduces (compared to that of a single droplet) in both tandem and square arrangements. In [19] the amount of the reduction in drag coefficient was $\sim$15%. In this study, as drag decreases, a higher U_{cr} is required to overcome the adhesion of the upstream droplets to the surface (see Figure A-5).

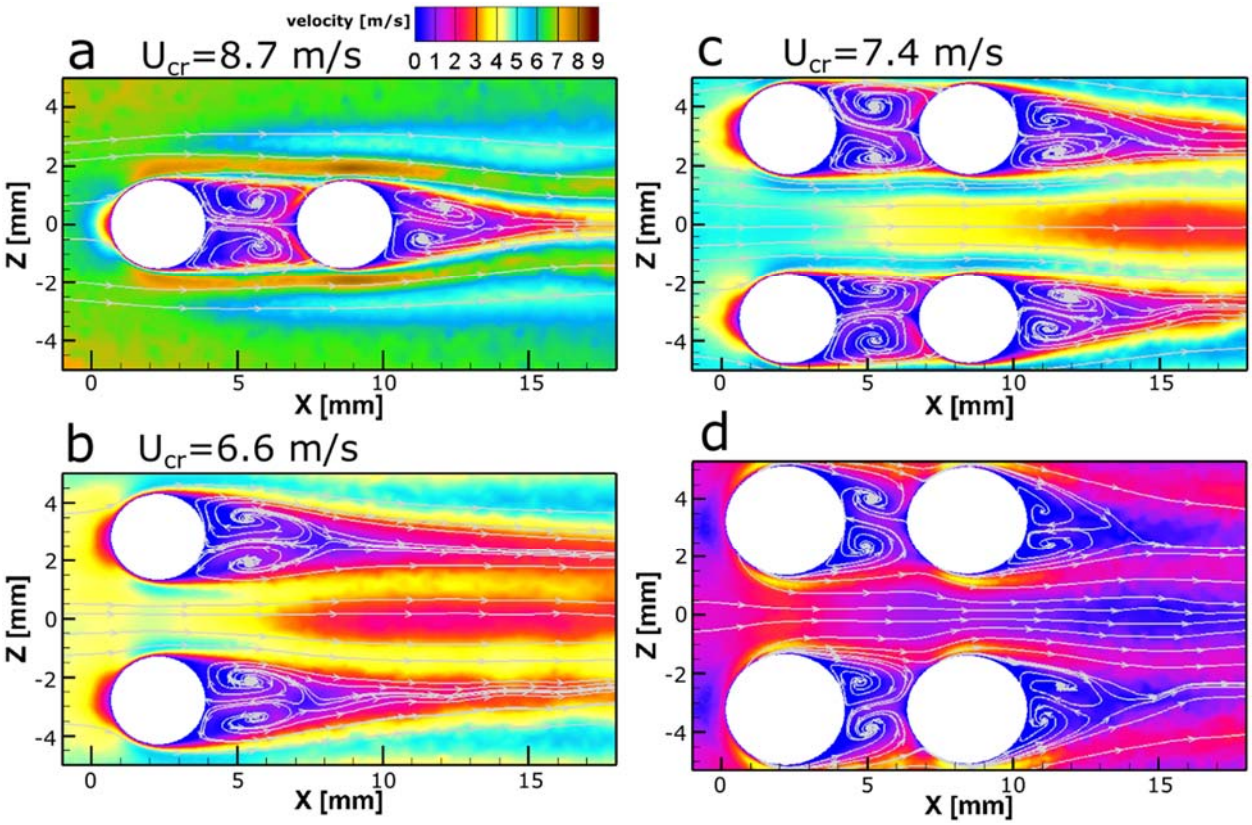

Figure A-7 *Time-independent velocity fields and streamlines for a) Tandem, b) Side-by-side, c) Square arrangements of simulated droplets all at the X-Z, Y=0.5 H plane, and d) Square arrangement of simulated droplets at the X-Z, Y=0.14 H plane (hence droplet foot print is seen to be larger than Y=0.5 H plane). Plots are for 10 μl simulated droplets on a hydrophilic surface at S= 1.5. Color plots online.*

Still, at S=1.5, the U_{cr} of the upstream droplets in a square arrangement is lower than that of a tandem arrangement. The possible explanation can be the acceleration of the airflow at the gap between the upstream, side-by-side droplets. Due to the shape of a sessile droplet on a hydrophilic surface, i.e. curvature of the interface, such an acceleration was not detected at the X-Z, Y=0.5H plane (Figure A-7(b)). So, the velocity field for square arrangement is also examined at the X-Z, Y=0.14 H, where droplets are closer together due to droplet curvature (see Figure A-7(d)). At S=1.5, the flow

acceleration at the gap between the side-by-side bodies was found to increase the drag coefficient by ~11% (compared to that of a single body) [20]. The counter effects of the tandem and side-by-side arrangements on drag, results in upstream droplets of square arrangement showing a U_{cr} between those of the tandem and side-by-side droplets.

From Figure A-5 it can be understood that as spacing increases to 3.5, the U_{cr} decreases for the upstream droplet of tandem arrangement, and it increases for the side-by-side droplets. Accordingly, U_{cr} of the upstream droplets in the square arrangement, which is the combination of tandem and side-by-side arrangements, does not change significantly. The most likely reason for the increase of the U_{cr} of the side-by-side droplets at spacing of 3.5 is the continuous interaction of the droplets' recirculation wakes and vortices, due to the oscillation of the sessile droplets (as observed in experiments). It has been reported by Zhou et al. [21] that the oscillation of the side-by-side bodies results in the drag coefficient reduction (from the value for that of a single body) at an intermediate spacing. In fact, the interference of the separate wake regions of the side-by-side bodies reduces the flow strength, and causes such a reduction in drag [21]. However, such an interaction of wakes and vortices cannot be detected in our simulation results due to the simplifications mentioned earlier.

A.3.3. REVERSED TRIANGLE AND DIAMOND ARRANGEMENTS

The upstream droplets in a reversed triangle arrangement show the same U_{cr} as the upstream droplet in a diamond arrangement, at both spacing of 1.5 and 3.5, considering the error bars (see Figure A-5). The velocity field and the streamline patterns for droplets in a reversed triangle, and diamond arrangements, is shown in Figure A-8 at

the X-Z, Y=0.5 H plane. For reversed triangle, at S=1.5 (Figure A-8(a)), the upstream vortices are compressed by ~26%, compared to that of a single simulated droplet at the same airflow velocity of 8 m/s (see Figure A-4(b)). For diamond arrangement, the amount of the compression of the upstream vortices is even more; about 37% (Figure A-8(c)). This implies that the suppression of the flow due to the interaction of the nearby droplets should decrease the drag coefficient, since U_{cr} increases above the value for that of a single droplet.

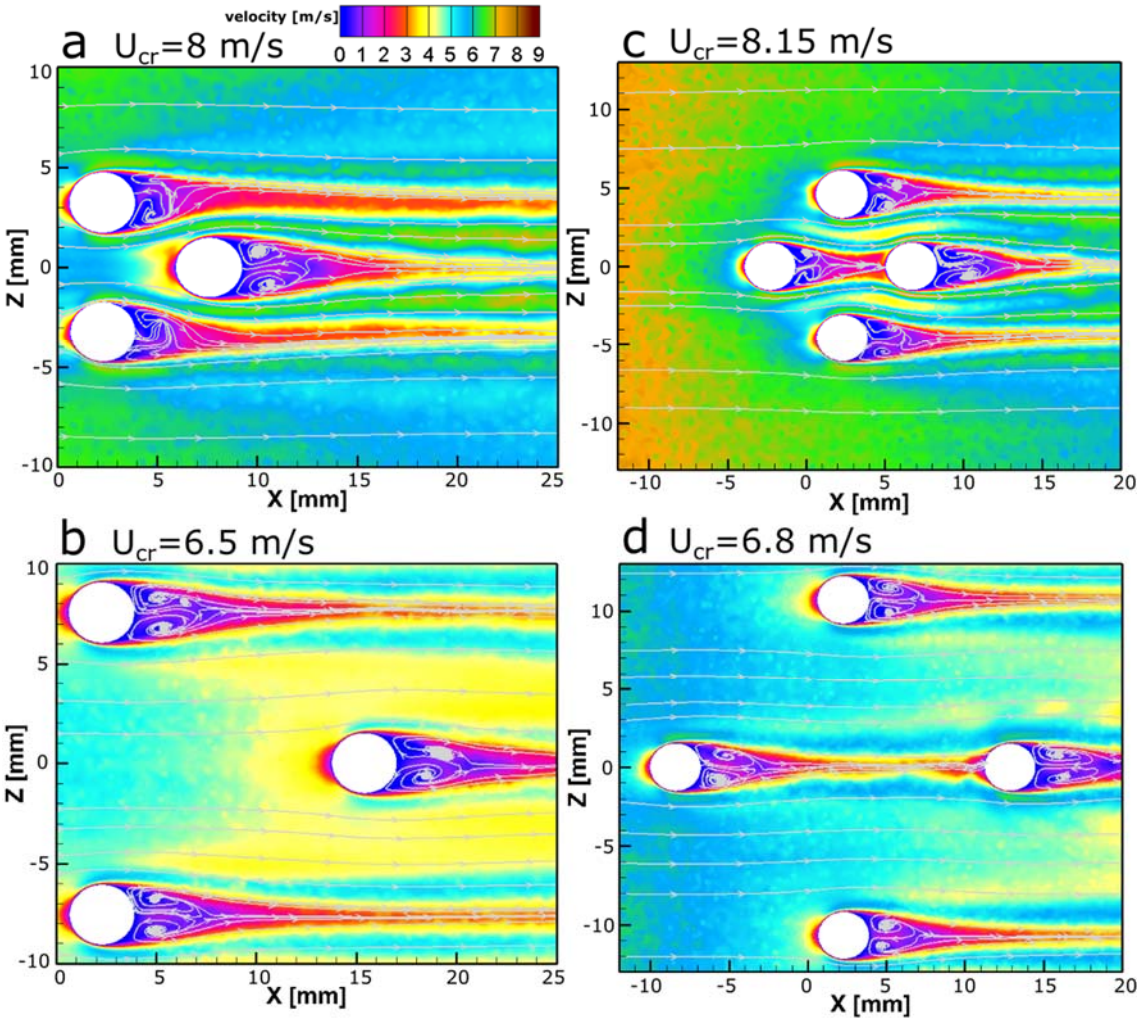

Figure A-8 *Time-independent velocity fields and streamline patterns for simulated droplets in reversed triangle arrangement a) At S=1.5, b) At S=3.5, and diamond arrangement c) At S=1.5,*

d) At S=3.5; at the X-Z, Y=0.5 H plane. Plots are for 10 μl simulated droplets on a hydrophilic surface. Color plots online.

As spacing increases to 3.5, Figures A-8(b) and 8d show that the interaction of the flow around the droplets almost diminishes; as the vortices have a similar size to that of a single simulated droplet (see Figure A-4(a)).

A.3.4. EFFECTS OF SURFACE WETTABILITY

The wettability of the solid surface changes the shape of a sessile droplet, so the flow pattern and wake interactions will be changed. On a hydrophilic surface, compared to a hydrophobic surface, sessile droplets have a flatter shape and present a larger baseline length. Since the spacing is the ratio of droplets center to center distance to the baseline length; at a constant spacing, droplets are closer to each other on a hydrophobic surface, due to the smaller baseline length. Figures A-9(a) to A-9(d) show the flow fields and streamlines for simulated droplets in triangle and square arrangements at S=1.5 on a hydrophobic (9a and 9c) and a hydrophilic (9b and 9d), surfaces. Figure A-9 is plotted at the X-Z, Y=0.5 H plane; where H is 2mm for the simulated droplets on a hydrophobic surface, and that is 1.4mm on a hydrophilic surface. For the square arrangement on a hydrophobic surface (Figure A-9(a)) the streamlines between the upstream side-by-side simulated droplets are more squeezed compared to that of a hydrophilic surface (Figure A-9(b)). Also, the suppression of the upstream vortices is more pronounced on a hydrophobic surface. For the triangle arrangement, the vortices formed at the rear of the upstream droplet are more compressed on the hydrophobic surface (9-c) compared to that of the hydrophilic surface (9-d). In fact, the comparison of the flow fields indicates

that the interaction of the simulated droplets is more intense on a hydrophobic surface than that of ones on a hydrophilic surface. This is not surprising since at a constant spacing, droplets are closer to each other on the hydrophobic surface. Also, a more spherical shape of the droplet on the hydrophobic surface, leads to a higher intensity of interaction, compared to a flatter shape of droplets on the hydrophilic surface [22].

Despite the higher interaction of neighboring droplets on a hydrophobic surface, Figure A-9(e) shows a similar amount of increase in the U_{cr} for both surface wettabilities. On average, there is a maximum 40% increase for triangle, and a minimum 20% increase for square arrangement. Only, the upstream droplets in a reversed triangle arrangement exhibit a ~13 % increase in the U_{cr} on a hydrophobic surface compared to the hydrophilic one. Similar results in terms of the U_{cr} variation with substrate wettability was observed for 5 μl droplets; data are provided in the Supporting Information. One explanation for the similar $U_{cr}/(U_{cr})_{single}$ variation with droplets' arrangement type, on both surface wettabilities, may be the proportional evolution of the drag and adhesion forces up to the shedding moment. In [10], it was shown that due to the increasing airflow velocity, drag force increases; adhesion force, as a resistance to drag, evolves equally with drag force up to the point of incipient motion (after which adhesion cannot further increase, but drag will). As such, even if on the hydrophobic surface (compared to the hydrophilic) the amounts of the change in drag force is larger (due to the higher interaction of the droplets), the change in lateral adhesion force also will be larger. So, $U_{cr}/(U_{cr})_{single}$ remains the same for both surface wettabilities.

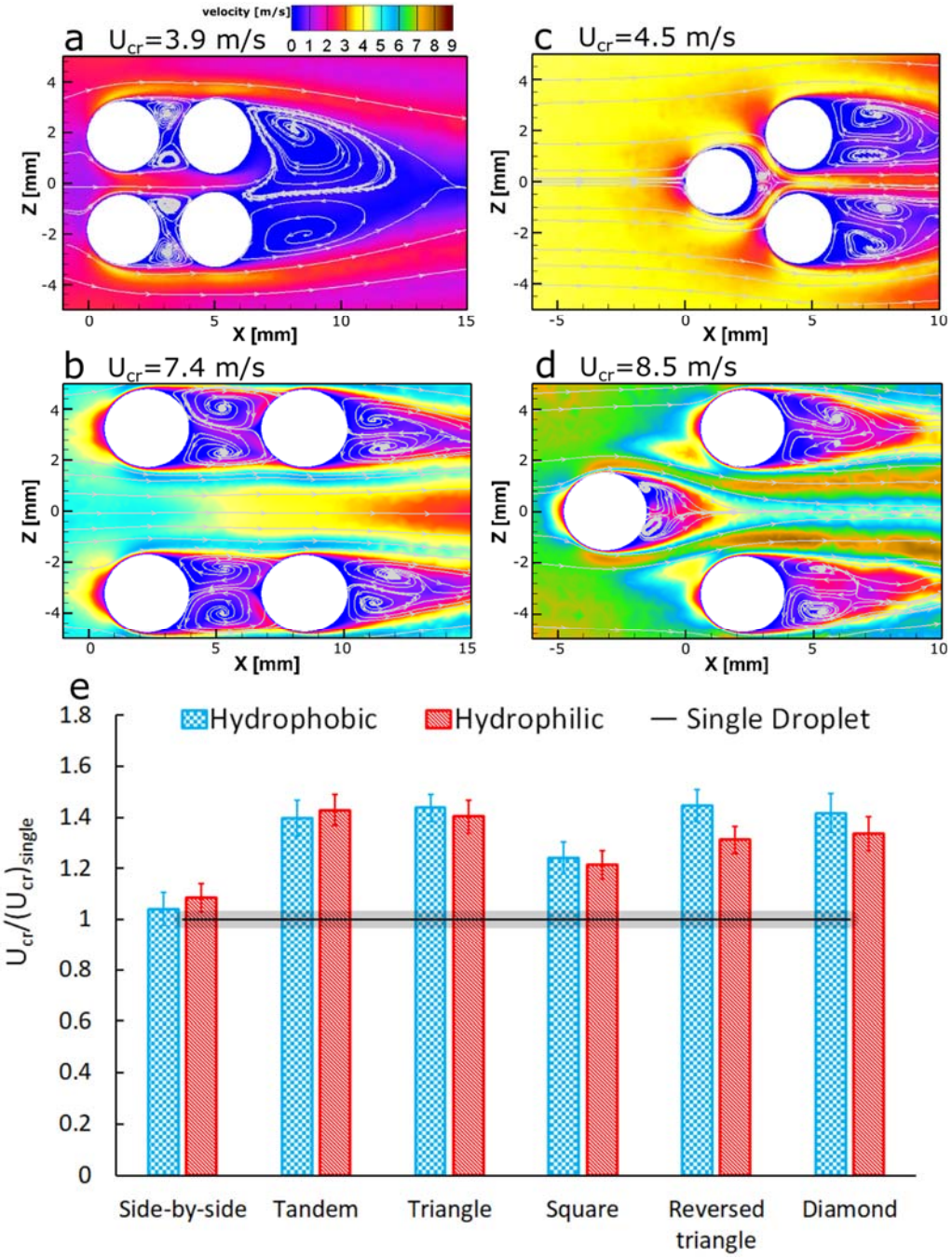

Figure A-9 *Time-independent velocity fields and streamlines for the simulated droplets in a) Square arrangement on a hydrophobic surface, b) Square arrangement on a hydrophilic surface, c) Triangle arrangement on a hydrophobic surface, d) Triangle arrangement on a hydrophilic surface, and e) Critical air velocity ratio comparison for the upstream droplet(s) in various arrangements on hydrophobic (Teflon) and hydrophilic (PMMA) surfaces. Plots are for 10 μl droplets at S=1.5.*

In addition, the oscillation of the sessile droplets found to be more intense on a hydrophilic surface compared to a hydrophobic surface. Milne et al. [23] showed that the frequency of the lateral oscillation for a 13 μl droplet on a hydrophilic surface is $\sim$ 35% higher than that of a hydrophobic surface. Effects of the droplets' oscillation were not considered in the numerical simulations in this study. On the other hand, it has been found that the oscillation can significantly alter the vortex shedding, and the size of the recirculation wake for the bluff bodies [24][25]. Generally, higher frequency of oscillation is associated with a wider recirculation wake [25]. As such, the current flow fields represent the intensity of the interaction for multiple sessile droplets with limitations.

A.3.5. COMPARISON OF THE ARRANGEMENTS

As it is seen in Figure A-5, for a fix number of sessile droplets, the type of the droplets' arrangement affects the U_{cr}. For three sessile droplets, within a small spacing, the upstream droplet in a triangle arrangement shows a higher U_{cr} compared to the upstream side-by-side droplets in a reversed triangle arrangement. Similarly, for four droplets, the upstream droplet in a diamond arrangement, presents a higher U_{cr} compared to the upstream droplets in a square arrangement.

As it was discussed before, two side-by-side sessile droplets, at an intermediate spacing, have the maximum U_{cr}, probably due to the aforementioned oscillations of sessile droplets, which increase the interaction between them. However, by presence of one droplet (like reversed triangle arrangement), or two droplets (like square arrangement), at the downstream of the side-by-side droplets, U_{cr} decreases. As such, at

S=3.5, the upstream droplets in the reversed triangle, and square arrangements, have 22% and 5% lower U_{cr} compared to that of a pair of side-by-side droplets, respectively.

In general, there is a maximum ~40% increase in U_{cr} for the upstream droplet in tandem and triangle arrangement at S=1.5 on both hydrophilic and hydrophobic surfaces. As the spacing increases to 3.5, U_{cr} decreases for the upstream droplets in triangle, reversed triangle, and diamond arrangements; whereas in square arrangement the spacing does not affect the U_{cr}.

A.3.6 INDEPENDENT SHEDDING OF MULTIPLE SESSILE DROPLETS

As the effects of the droplets arrangement, and spacing on U_{cr} is identified, the next question to ask is when will droplets shed independently from each other at the U_{cr} of a single droplet, regardless of the type of arrangement.

To answer this question, we start from our findings in [10] for shedding of a pair of sessile droplets; it was observed that when two droplets are at $S \geq 5.5$ on a hydrophilic surface, and at $S \geq 3.5$ on a hydrophobic surface, they shed independently, at the U_{cr} of a single droplet. This was true for both tandem and side-by-side arrangements. For side-by-side arrangement, both droplets also shed at the U_{cr} of a single droplet for $S \leq 1.5$ on both surface wettabilities [10]. To see if the “no interaction” spacings hold for shedding of three or four sessile droplets, the following arrangements were considered: triangle at S=5.5, and rectangle at $S_{side\text{-}by\text{-}side} \times S_{tandem} = 1.5 \times 5.5$. One may hypothesis that the “no interaction” spacing can be the same for both triangle and tandem arrangement. Also, rectangle arrangement of four droplets consists of two pairs of side-by-side and tandem

droplets, both within “no interaction” spacings. As it is shown in Figure A-10, droplets shed independently and at the U_{cr} of a single droplet. This means that as long as the droplets are placed at the “no interaction” spacing (found from experiments with a pair of droplets), they will shed independently, regardless of the type of the arrangement. The argument above is also true for 5 μl droplets; a graph similar to Figure A-10 is provided in the Supporting Information.

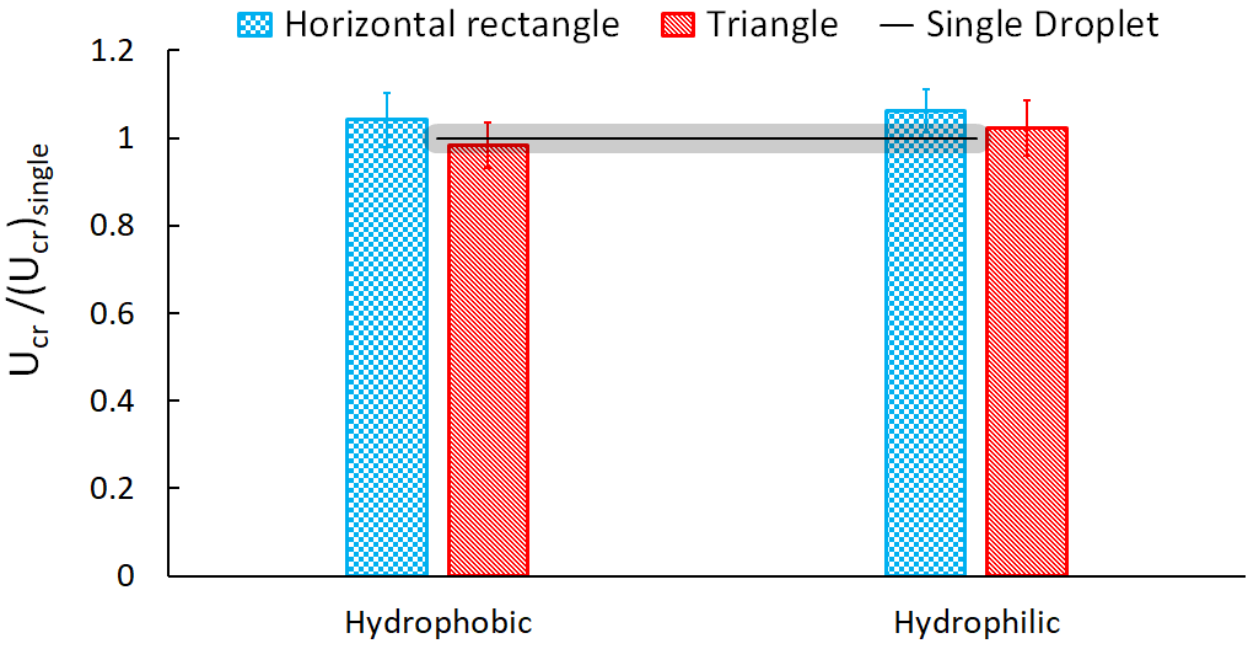

Figure A-10 *Critical air velocity ratio to that of a single droplet for the upstream droplets in a rectangle arrangement, and the upstream droplet in a triangle arrangement on both hydrophobic, and hydrophilic surfaces for 10 μl droplets. The value of spacing for the rectangle arrangement is Sside-by-side×Standem =1.5×3.5 on a hydrophobic surface, and is Sside-by-side×Standem =1.5×5.5 on a hydrophilic surface. For triangle arrangement, S is 3.5 for hydrophobic surface, and it is 5.5 for a hydrophilic surface. The error of the Ucr for the single sessile droplet is shown by the shaded band.*

It can be understood from the above discussions that there exists a critical value for spacing which is dependent to the surface wettability. For the spacings smaller than the critical value, both the arrangement type, and value of spacing affect the U_{cr} of the upstream droplets. Beyond the critical spacing, regardless of the type of arrangement, all droplets shed independently with the U_{cr} of a single sessile droplet.

A.4. CONCLUSIONS

Shedding of three and four sessile droplets, in proximity of each other, and with different arrangements were investigated. At a specific airflow velocity (i.e. U_{cr} for each case), the flow structure over the droplets changes with the arrangement type for droplets, and spacing between them. As such, for each case, the air velocity to overcome the adhesion force, is changed. Upstream droplets in all arrangements show a higher U_{cr} compared to that of a single droplet; with the highest value observed for triangle arrangement at S=1.5 (~40% higher), and the lowest for reversed triangle arrangement at S=3.5 (same as the single droplet). Similar results were found for both surface wettabilities. Increasing the spacing for triangle, reversed triangle, and diamond arrangement leads to a decrease in U_{cr}; however, U_{cr} of the upstream droplets in square arrangement does not show sensitivity to spacing. When there are three droplets on a surface, the upstream droplet in triangle arrangement sheds at a relatively higher U_{cr} than the side-by-side droplets of reversed triangle arrangement. The same is true for comparison of the upstream droplet(s) in diamond and square arrangements for four droplets. The above change in U_{cr} was explained using simulations to understand the flow around droplets. The change in U_{cr} is due to change in drag on droplets as a result of changes in vortex interaction at a given airflow speed. Finally, it was shown when the

droplets are placed far enough from each other (S=5.5 for hydrophilic and S=3.5 for hydrophobic surface), the configuration of the arrangement has no effect on the U_{cr}.

A.5. REFERENCES

[1] P. Dimitrakopoulos and J. J. Higdon, “On the displacement of three-dimensional fluid droplets from solid surfaces in low-Reynolds-number shear flows,” J. Fluid Mech. 377, 189 (1998).

[2] P. Dimitrakopoulos and J. J. Higdon, “Displacement of fluid droplets from solid surfaces in low-Reynolds-number shear flows,” J. Fluid Mech. 336, 351 (1997).

[3] A. D. Sommers, J. Ying, K. F. Eid, “Predicting the onset of condensate droplet departure from a vertical surface due to air flow—Applications to topographically-modified, micro-grooved surfaces,” Exp. Therm. Fluid Sci. 40, 38 (2012).

[4] H. Ding and P. D. Spelt, “Onset of motion of a three-dimensional droplet on a wall in shear flow at moderate Reynolds numbers,” J. Fluid Mech. 599, 341 (2008).

[5] T. Cebeci and F. Kafyeke, “Aircraft icing,” Annu. Rev. Fluid Mech. 35, 11 (2003).

[6] A. J. B. Milne and A. Amirfazli, “Drop shedding by shear flow for hydrophilic to superhydrophobic surfaces,” Langmuir. 25, 14155 (2009).

[7] J. Fan, M. C. Wilson, N. Kapur, “Displacement of liquid droplets on a surface by a shearing air flow,” J. Colloid Interface Sci. 356, 286 (2011).

[8] H. Ding, M. N. Gilani, P. D. Spelt, “Sliding, pinch-off and detachment of a droplet on a wall in shear flow,” J. Fluid Mech. 644, 217 (2010).

[9] S. Moghtadernejad, M. Tembely, M. Jadidi, N. Esmail, A. Dolatabadi," Shear driven droplet shedding and coalescence on a superhydrophobic surface," Phys. Fluids. 27, 032106 (2015).

[10] A. Razzaghi and A. Amirfazli, "Shedding of a Pair of Sessile Droplets," Int. J. Multiphase Flow. Revision Submitted, July 2018.

[11] Y. Tsuji, Y. Morikawa, Y. Fujiwara, "Pipe flow with solid particles fixed in space," Int. J. Multiphase Flow. 11, 177 (1985).

[12] S. C. Liang, T. Hong, L. S. Fan, "Effects of particle arrangements on the drag force of a particle in the intermediate flow regime," Int. J. Multiphase Flow. 22, 285 (1996).

[13] C. Zhu, K. Lam, H. H. Chu, X. D. Tang, G. Liu, "Drag forces of interacting spheres in power-law fluids," Mech. Res. Commun. 30, 651 (2003).

[14] M. Ozgoren, "Flow structures around an equilateral triangle arrangement of three spheres," Int. J. Multiphase Flow. 53, 54 (2013).

[15] C. You, H. Qi, X. Xu, "Drag force in dense gas-particle two-phase flow," ACTA Mech. Sin. 19, 228 (2003).

[16] A. Maheshwari, R. P. Chhabra, G. Biswas, "Effect of blockage on drag and heat transfer from a single sphere and an in-line array of three spheres," Powder Tech. 168, 74 (2006).

[17] R. C. Chen, J. L. Wu, "The flow characteristics between two interactive spheres," Chem. Eng. Sci. 55, 1143 (2000).

[18] R. Clift, J. R. Grace, M. E. Weber, "Bubbles, drops, and particles," (Dover Publications: Mineola N.Y. USA, 2005, 103).

[19] T. Tsuji, R. Narutomi, T. Yokomine, S. Ebara, A. Shimizu, “Unsteady three-dimensional simulation of interactions between flow and two particles,” Int. J. Multiphase Flow. 29, 1431 (2003).

[20] R. Hassanzadeh, B. Sahin, M. Ozgoren, “Large eddy simulation of flow around two side-by-side spheres,” J. Mech. Sci. Technol. 27, 1971 (2013).

[21] Y. Zhou, Z. J. Wang, R. M. So, S. J. Xu, W. Jin, “Free vibrations of two side-by-side cylinders in a cross-flow,” J. Fluid Mech. 443, 197 (2001).

[22] N. Kishore, “Flow and drag phenomena of tandem spheroid particles at finite Reynolds numbers,” Ind. Eng. Chem. Res. 51, 3186 (2012).

[23] A. J. B. Milne, B. Defez, M. Cabrerizo-Vílchez, A. Amirfazli, “Understanding (sessile/constrained) bubble and drop oscillations. Adv,” Colloid Interface Sci. 203, 22 (2014).

[24] P. W. Bearman, “Vortex shedding from oscillating bluff bodies,” Annu. Rev. Fluid Mech. 16, 195 (1984).

[25] H. M. Blackburn and R. D. Henderson, “A study of two-dimensional flow past an oscillating cylinder,” J. Fluid Mech. 385, 255 (1999).

Appendix – B

Details of the numerical simulation tool

As mentioned in Chapter 3, the Coupled Level Set method was used in VOF method. A submerged solid body approach was implemented using a weak coupling with an incompressible solver. The scheme used in the solver was 2^{nd} order for space and 1^{st} order for the time and the number of iterations between LS and VOF was chosen by the solver. Gravity effect has been considered in all simulations both for the still and the moving particle. A mesh independency was performed on the initial base grid by having the grid size and solving the same case for the results to be compared. When the maximum change of velocity and pressure fields between two consecutive domains was less than 1%, that grid was selected as the base mesh for the rest of simulations.

A maximum of 5 levels was used for the Dynamic Refinement of mesh. The refinement was done based on the gradient of the volume fraction as well as gradients of pressure and velocity throughout the domain. Adding more levels of refinements did not add up to the accuracy and the maximum change in the results (compared to having 5 refinement levels) was less than 1%.

For the experiments performed in Chapter 2, a thin rod was used beneath the particle to keep it in place. However, the rod was not considered in the simulations as it was not supposed to be present in the original definition of the problem. However, a separate simulation case was prepared in which the rod beneath the particle was also modeled as a wall. The goal was to confirm whether the existence of the rod has a significant effect

on the impact products (especially for the low Weber numbers). Figure B-1 compares the results of the two cases, still particle with and without the rod, for a low Weber number (*We*=0.05). Wettability of the rod material was set to be equal to the particle that it is attached to ($\theta_{eq} = \mathbf{70}°$). The results are shown in Fig. B-1 in the same flow time (t=15 ms). It can be concluded that the rod can be safely removed from the simulations without creating a meaningful change in the impact outcome.

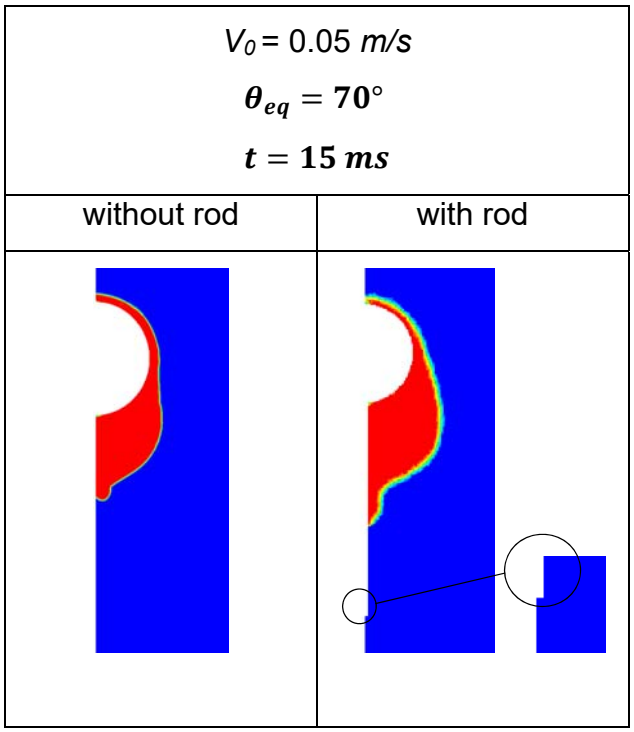

Figure B-1 Comparison between results of the numerical simulation with and without the rod beneath the particle

Appendix – C

User Defined Function for calculating the dynamic contact angle

```
#include "udf.h"
//double contact_line_position=0;
double theta_e_radian=(118.0*M_PI/180.0);
double dynamic_contact_angle=118.0;
int first_time=0,TPL_detected=0,time_step_number;
double contact_velocity=0;
FILE *file;
double old_t=0,xG_old=0,R=0;
real x1[ND_ND];
real x2[ND_ND];
static int last_ts = -1;
DEFINE_ADJUST(Contact_Angle_Update, domain)
{
#if !RP_HOST    /*  only host process is involved */
Thread *thread = Lookup_Thread(domain, 9); /*9 is ID number of the particle as a wall boundary*/
        Thread **pt = THREAD_SUB_THREADS(thread);
        cell_t cell;
        face_t f;
   real xG=0;
        real x[ND_ND];
        real xx[ND_ND];
        double f_Hoff_inverse, x_hoff,temp, Ca, volume;
        real i=0,j=0;
        time_step_number=N_TIME;  /*I need the procedure to be repeated every 10 time steps and velocity is calculated*/
   //Message("TimeStep=%d \n ",N_ITER);
   if (time_step_number%20==0 && last_ts != N_TIME) //since the iteration number won't become zero each time, continues from the last TS
   {
      last_ts = N_TIME;
      xx[0]=0;
```

```
      xx[1]=0;
      x[0]=0;
      x[1]=0;
   TPL_detected=0;
        begin_c_loop_all (cell,pt[1])
   {
            C_CENTROID(x,cell,pt[1]);
xG+=x[0];//C_VOLUME(cell,pt[1]);
TotalArea+=C_VOLUME(cell,pt[1]);
            j+=1;  /*the past 3 lines calculate X of particle C.G. as it moves in the domain
to be used later*/

                  if(/*C_VOF(cell,pt[1])>0.5 &&*/ C_VOF(cell,pt[1])>0.5 &&
TPL_detected==0)  /*finds all cells in the triple point area to be averaged later*/
                  {TPL_detected=1;
                  C_CENTROID(x,cell,pt[1]);

                  xx[0]=x[0];//C_VOLUME(cell,pt[1]);  xx[0]+=x[0]
                  xx[1]=x[1];//C_VOLUME(cell,pt[1]);  xx[1]+=x[1]
                  //i+=1;
            //    TotArea+=C_VOLUME(cell,pt[1]);
                  }

      }
        end_c_loop_all (cell,pt[1])

        #if RP_NODE     //in parallel mode, sums up the variables calculated on different
cores
      i=PRF_GISUM1(i);
      j=PRF_GISUM1(j);
      xx[0]=PRF_GRSUM1(xx[0]);
      xx[1]=PRF_GRSUM1(xx[1]);
      xG=PRF_GRSUM1(xG);
#endif

        x2[0]=xx[0];   //..   /i;
        x2[1]=xx[1];   //....   /i; /*averages all the cells on TP area to report just one point*/
        xG=xG/j-0.000006;  /*averages all x-coordinates of the cells adjacent to the
particle to find its C.G. -- 6e-6 is a calibration thing*/
```

```
   if(first_time==0) /*this condition is met only the first time that particle gets wet, as we
don't have a second point on particle to calculate the velocity*/
   {              /*so it captures the time to be able to calculate del_t later*/
   first_time=1;
   old_t=CURRENT_TIME;
   xG_old=xG;
   x1[0]=x2[0];
   x1[1]=x2[1];
   }
   else  /*this condition will be met after particle gets wet*/
            {
         R=0.001*sqrt(pow((acos((x2[0]-xG)/0.001)-acos((x1[0]-xG_old)/0.001)),2));

                  contact_velocity= R/(CURRENT_TIME-old_t);

                  Ca = contact_velocity*0.001003/0.0728;
                  temp= 0.5-0.5 * cos(theta_e_radian);
                  temp= 0.5 * log( (1.0+temp)/(1.0-temp) );//atanh(0.5-0.5 *
cos(theta_e_radian))
                  f_Hoff_inverse = -(9.78546 *
pow(temp,1.416430594900850))/(12.819*pow(temp,1.41643)-100.0);
                  x_hoff= Ca +  f_Hoff_inverse ;
                  if(contact_velocity>=0)
                           dynamic_contact_angle= acos(1-
2*tanh(5.16*pow((x_hoff/(1+1.31*pow(x_hoff,.99))),0.706))) *180.0/M_PI  ;
                  else
                           dynamic_contact_angle= 2*theta_e_radian*180.0/M_PI -acos( 1-
2*tanh(5.16*pow((x_hoff/(1+1.31*pow(x_hoff,.99))),0.706)   ) ) *180.0/M_PI  ;

                  if(I_AM_NODE_ZERO_P)
                  {

                  file = fopen("file.txt", "a+");
                  fprintf(file, "Time=%f R=%f contact_velocity=%f
dynamic_contact_angle=%f X1[0]=%f X2[0]=%f X1[1]=%f X2[1]=%f
xG=%f\n",CURRENT_TIME,R,contact_velocity,dynamic_contact_angle,x1[0],x2[0],x1[1]
,x2[1],xG);
                  fclose(file);
                  }
```

```
                x1[0]=x2[0];  /*current position of TP is stored as the old position for the
next time step*/
                x1[1]=x2[1];


      old_t=CURRENT_TIME; /*current time is stored for the next loop to calculate
del_t*/
      xG_old=xG;
      }

   }
   if (first_time==0)
   dynamic_contact_angle=118;
   else if(dynamic_contact_angle<180 && dynamic_contact_angle>0) /*to make sure
there is no weird output for DCA and DCA is not infinity*/
   dynamic_contact_angle=dynamic_contact_angle;
   else
   dynamic_contact_angle=118;
#endif
}


DEFINE_PROFILE(Contact_Angle_Set_Profile,t,i)
{
#if !RP_HOST      /*  only host process is involved */
         face_t f;
         begin_f_loop(f,t)
            {
                F_PROFILE(f,t,i) = dynamic_contact_angle;
      }
         end_f_loop(f,t)
#endif
}
```